



DOCUMENTATION PAGE

Form Approved
OMB No. 0704-0188



This information is estimated to average 1 hour per response, including the time for reviewing instructions, searching existing data sources, gathering the data, reviewing the collection of information, sending comments regarding this burden estimate or any other aspect of this collection of information, including suggestions for reducing this burden, to Washington Headquarters Services, Directorate for Information Operations and Reports, 1215 Jefferson Davis Highway, Suite 1204, Arlington, VA 22202-4302, and to the Office of Management and Budget, Paperwork Reduction Project (0704-0188), Washington, DC 20503.

1. AGENCY USE ONLY (Leave blank)		2. REPORT DATE June 1992	3. REPORT TYPE AND DATES COVERED THESES DISSERTATION	
4. TITLE AND SUBTITLE Particle Simulation of Auroral Double Layers			5. FUNDING NUMBERS	
6. AUTHOR(S) Bruce L. Smith,				
7. PERFORMING ORGANIZATION NAME(S) AND ADDRESS(ES) AFIT Student Attending: Princeton University			8. PERFORMING ORGANIZATION REPORT NUMBER AFIT/CI/CIA- 92-0220	
9. SPONSORING/MONITORING AGENCY NAME(S) AND ADDRESS(ES) AFIT/CI Wright-Patterson AFB OH 45433-6583			10. SPONSORING/MONITORING AGENCY REPORT NUMBER	
11. SUPPLEMENTARY NOTES				
12a. DISTRIBUTION/AVAILABILITY STATEMENT Approved for Public Release IAW 190-1 Distributed Unlimited ERNEST A. HAYGOOD, Captain, USAF Executive Officer			12b. DISTRIBUTION CODE	
13. ABSTRACT (Maximum 200 words)				
<p>92-31148</p> 170?				
14. SUBJECT TERMS			15. NUMBER OF PAGES 155	
			16. PRICE CODE	
17. SECURITY CLASSIFICATION OF REPORT	18. SECURITY CLASSIFICATION OF THIS PAGE	19. SECURITY CLASSIFICATION OF ABSTRACT	20. LIMITATION OF ABSTRACT	

92 12 08 076

Particle Simulation of Auroral Double Layers
Bruce L. Smith

Externally driven magnetic reconnection has been proposed as a possible mechanism for production of auroral electrons during magnetic substorms. Fluid simulations of magnetic reconnection lead to strong plasma flows towards the increasing magnetic field of the earth. These plasma flows must generate large scale potential drops to preserve global charge neutrality. We have examined currentless injection of plasma along a dipole magnetic field into a bounded region using both analytic techniques and particle simulation.

Our analysis shows that the maximum potential for cold ions and electrons, mass ratio $\frac{m}{M}$, is $q\Delta V = K \frac{1-\frac{m}{M}}{2} \propto \mu \Delta B$, where μ is their common magnetic moment, K is the kinetic energy of the injected ions, and ΔB is the difference between the maximum magnetic field strength, B_{MAX} , and that at injection, B_0 . With thermal spread in particle magnetic moments the potential depends on their temperature ratios, $\frac{T_i}{T_e}$, and with thermal injection velocities the magnetic field mirror ratio, $\frac{B_{MAX}}{B_0}$. For drifting isotropic Maxwellians, the leading order potential is $q\Delta\phi = K \frac{1-\frac{m}{M} \frac{T_i}{T_e}}{1+\frac{T_i}{T_e}} \frac{\Delta B}{B_{MAX}}$.

This potential is a boundary condition for the local field solution. While global charge neutrality must be maintained in steady-state, the local potential is determined by the Vlasov-Poisson equations. Several authors obtained quasineutral solutions ($n_i = n_e$) to this boundary value problem. However, single-valued quasineutral solutions are only accessible to special combinations of fields and particle distributions. In our case multivalued solutions to the quasineutral equation arise for particular values of electric and magnetic fields. A double layer is that solution which preserves gross quasineutrality within its volume while permitting momentum balance between incident accelerated particles. The potential of the double layer is limited by the ion kinetic energy but need not match the global potential required for overall charge neutrality.

One and two dimensional electrostatic particle simulations verify both double layer solutions and dependence of potentials on the injected energy. The difference between global and local potentials is absorbed in a sheath opposite the injection boundary.

Potential formations are strictly dependent on the self-consistent charge distributions they support. Microinstabilities cause changes in particle distributions. Double layer motion is associated with exchange of momentum between particles and these fields.

Accession For	
NTIS CRA&I	<input checked="" type="checkbox"/>
DTIC TAB	<input type="checkbox"/>
Unannounced	<input type="checkbox"/>
Justification	
By	
Distribution /	
Availability Codes	
Dist	Avail and/or Special
A-1	

Particle Simulation of Auroral Double Layers
Bruce L. Smith

Externally driven magnetic reconnection has been proposed as a possible mechanism for production of auroral electrons during magnetic substorms. Fluid simulations of magnetic reconnection lead to strong plasma flows towards the increasing magnetic field of the earth. These plasma flows must generate large scale potential drops to preserve global charge neutrality. We have examined currentless injection of plasma along a dipole magnetic field into a bounded region using both analytic techniques and particle simulation.

Our analysis shows that the maximum potential for cold ions and electrons, mass ratio $\frac{m}{M}$, is $q\Delta V = K \frac{1-\frac{m}{M}}{2} \propto \mu \Delta B$, where μ is their common magnetic moment, K is the kinetic energy of the injected ions, and ΔB is the difference between the maximum magnetic field strength, B_{MAX} , and that at injection, B_0 . With thermal spread in particle magnetic moments the potential depends on their temperature ratios, $\frac{T_i}{T_e}$, and with thermal injection velocities the magnetic field mirror ratio, $\frac{B_{MAX}}{B_0}$. For drifting isotropic Maxwellians, the leading order potential is $q\Delta\phi = K \frac{1-\frac{m}{M} \frac{T_i}{T_e}}{1+\frac{T_i}{T_e}} \frac{\Delta B}{B_{MAX}}$.

This potential is a boundary condition for the local field solution. While global charge neutrality must be maintained in steady-state, the local potential is determined by the Vlasov-Poisson equations. Several authors obtained quasineutral solutions ($n_i = n_e$) to this boundary value problem. However, single-valued quasineutral solutions are only accessible to special combinations of fields and particle distributions. In our case multivalued solutions to the quasineutral equation arise for particular values of electric and magnetic fields. A double layer is that solution which preserves gross quasineutrality within its volume while permitting momentum balance between incident accelerated particles. The potential of the double layer is limited by the ion kinetic energy but need not match the global potential required for overall charge neutrality.

One and two dimensional electrostatic particle simulations verify both double layer solutions and dependence of potentials on the injected energy. The difference between global and local potentials is absorbed in a sheath opposite the injection boundary.

Potential formations are strictly dependent on the self-consistent charge distributions they support. Microinstabilities cause changes in particle distributions. Double layer motion is associated with exchange of momentum between particles and these fields.

PARTICLE SIMULATION
OF
AURORAL DOUBLE LAYERS

Bruce L. Smith

A DISSERTATION
PRESENTED TO THE FACULTY
OF PRINCETON UNIVERSITY
IN CANDIDACY FOR THE DEGREE
OF DOCTOR OF PHILOSOPHY

RECOMMENDED FOR ACCEPTANCE
BY THE DEPARTMENT OF
ASTROPHYSICAL SCIENCES

June 1992

Externally driven magnetic reconnection has been proposed as a possible mechanism for production of auroral electrons during magnetic substorms. Fluid simulations of magnetic reconnection lead to strong plasma flows towards the increasing magnetic field of the earth. These plasma flows must generate large scale potential drops to preserve global charge neutrality. We have examined currentless injection of plasma along a dipole magnetic field into a bounded region using both analytic techniques and particle simulation.

Our analysis shows that the maximum potential for cold ions and electrons, mass ratio $\frac{m}{M}$, is $q\Delta V = K \frac{1-\frac{m}{M}}{2} \propto \mu\Delta B$, where μ is their common magnetic moment, K is the kinetic energy of the injected ions, and ΔB is the difference between the maximum magnetic field strength, B_{MAX} , and that at injection, B_0 . With thermal spread in particle magnetic moments the potential depends on their temperature ratios, $\frac{T_i}{T_e}$, and with thermal injection velocities the magnetic field mirror ratio, $\frac{B_{MAX}}{B_0}$. For drifting isotropic Maxwellians, the leading order potential is $q\Delta\phi = K \frac{1-\frac{m}{M} \frac{T_i}{T_e}}{1+\frac{T_i}{T_e}} \frac{\Delta B}{B_{MAX}}$.

This potential is a boundary condition for the local field solution. While global charge neutrality must be maintained in steady-state, the local potential is determined by the Vlasov-Poisson equations. Several authors obtained quasineutral solutions ($n_i = n_e$) to this boundary value problem. However, single-valued quasineutral solutions are only accessible to special combinations of fields and particle distributions. In our case multivalued solutions to the quasineutral equation arise for particular values of electric and magnetic fields. A double layer is that solution which preserves gross quasineutrality within its volume while permitting momentum balance between incident accelerated particles. The potential of the double layer is limited by the ion kinetic energy but need not match the global potential required for overall charge neutrality.

One and two dimensional electrostatic particle simulations verify both double layer solutions and dependence of potentials on the injected energy. The difference between global and local potentials is absorbed in a sheath opposite the injection boundary.

Potential formations are strictly dependent on the self-consistent charge distributions they support. Microinstabilities cause changes in particle distributions. Double layer motion is associated with exchange of momentum between particles and these fields.

Contents

Abstract	i
Preface	ix
1 Introduction	1
2 Aurorae	11
2.1 The Sun's Plasma and Magnetic Fields	11
2.1.1 The Sun	11
2.1.2 The Solar Wind	12
2.1.3 Interplanetary Magnetic Field	13
2.2 The Earth's Magnetosphere	13
2.2.1 The Earth's Magnetic Field	13
2.2.2 The Magnetosheath	15
2.2.3 Convection Electric Field	16
2.2.4 Ionosphere	17
2.2.5 Plasma Sheet	17
2.2.6 Plasmasphere	18
2.2.7 Plasma Parameters	18
2.3 Aurorae and Substorms	18
2.3.1 Diffuse Aurorae	18
2.3.2 Discrete Aurorae	20
2.3.3 Geomagnetic Substorms	20
2.3.4 Plasma Jet Theory	23
3 Sheaths and Double-Layers	26
3.1 Maxwell-Boltzmann Equations	26

3.2	The Fluid Equations	27
3.3	Useful Idealizations	28
3.3.1	Quasi-Neutrality (Plasma Approximation)	28
3.3.2	The Adiabatic Approximation	29
3.4	Sheaths	32
3.4.1	One - Dimensional Sheath	32
3.5	Double Layers with Current	36
3.5.1	Double Sheaths	36
3.5.2	Block Theory	38
3.5.3	Kan and Lee	39
3.6	Currentless Double Layers	40
3.6.1	Perkins and Sun	40
3.6.2	Experiments	44
3.7	Overview	45
4	Analysis	48
4.1	Cold Model	48
4.2	Finite Perpendicular Temperature	53
4.2.1	Particle Currents	53
4.2.2	Particle Densities	54
4.2.3	Langmuir's Condition	58
4.3	Generalization to Drifting Maxwellian	60
4.3.1	Current Density	60
4.3.2	Particle Density	62
4.4	Summary	65
5	One Dimensional Particle Simulation	67
5.1	Physical Model	67
5.1.1	Particles	68
5.1.2	Electric Field	68
5.1.3	Magnetic Field	69
5.2	The Computational Model	69
5.2.1	Electric Field	70
5.2.2	Particles	71
5.3	Simulation Results	74
5.3.1	Simulation Parameters	74
5.3.2	Chronology	74

5.3.3	Velocity Distributions	76
5.3.4	Stringer Plots	76
5.3.5	Electric Field Potential	80
5.3.6	Wave Spectra	80
5.3.7	Energies	82
5.4	Discussion	82
5.4.1	Plasma Instabilities	82
5.4.2	A Kinetic Approach to Double Layers	85
5.4.3	Comparison with Plasma Jet Analysis	88
6	2D Simulation	92
6.1	Computational Model	92
6.1.1	Electric Field	92
6.1.2	Particles	95
6.2	Two Dimensional Results	97
6.2.1	Simulation Parameters	97
6.2.2	Chronology	97
6.2.3	Velocity Distributions	97
6.2.4	Electric Field Potential	99
6.3	Discussion	99
7	Conclusion	103
A	Particle Pushers	108
A.1	The "Leap Frog" Scheme	108
A.2	Gyrokinetic Solution	113
B	Poisson Solvers	116
B.1	Charge Aggregation and Force Interpolation	116
B.1.1	Pairwise Force Calculation	116
B.1.2	E Field Grid	116
B.1.3	Direct Integration	117
B.2	Electric Field Calculation	117
B.2.1	Difference Equations	117
B.2.2	Fourier Transform Solution	118
B.3	Particle Shapes	127
B.3.1	Cloud-in-Cell Weighting	127

B.3.2	Optimal Particle Shape	128
B.4	Extension to Two Dimensions	135
B.4.1	Poisson's Equation in Spherical and Cylindrical Co-ordinates	135
B.4.2	Continuous Solution	135
B.4.3	Matrix Solution	136
B.4.4	Solution for Electric-field	139
B.4.5	Charge Sharing/Force Interpolation	143
C	Buneman Algorithm Solution to the Mixed Boundary Condition Problem	147

List of Figures

1.1	An Aurora	2
1.2	Diffuse Aurorae and Auroral Arcs	3
1.3	Double Layer Driven by Fixed Potential	5
1.4	Sato and Okuda Circuit Model	6
1.5	Multiple Double Layers	7
2.1	The Earth's Magnetosphere	14
2.2	Polar Potentials	16
2.3	Near-Earth Plasma	19
2.4	Convective Flow	20
2.5	Polar Field-Aligned Currents	21
2.6	Auroral Potential Structure	22
2.7	Sato Model	24
3.1	K-V Plane	30
3.2	The First Law	31
3.3	1D Sheath	33
3.4	Plasma-Sheath Solution	35
3.5	Block Model	37
3.6	Perkins and Sun Densities	42
3.7	Cohen Solutions for Thermal Barrier Cells	43
3.8	Stenzel's Experiment	44
3.9	Stenzel's Potential	46
4.1	A Non-Quasineutral Potential	51
4.2	Cold Plasma	52
4.3	V vs Y	56
4.4	F _s	57

4.5	Maxwellian Electrons and Dawsonian Ions	59
4.6	Drifting Maxwellian Distribution Function	64
5.1	One Dimensional Model	68
5.2	Chronology of Substorm Simulation	75
5.3	Velocity Distribution Functions	77
5.4	Current Carrying Flows	78
5.5	Counterstreaming Beams	79
5.6	Potentials and Energy Spectra	81
5.7	Frequency Spectra	83
5.8	Energies	84
5.9	Double Layer Integration	86
5.10	Potential vs Kinetic Energy	88
6.1	The 2D Model	93
6.2	Velocity Space	98
6.3	Velocity Distributions	100
6.4	Potentials	101
6.5	Energies	102
A.1	The Leap Frog Scheme	109
A.2	Magnetic Coordinates	110
B.1	Area of Integration	120
B.2	Potential vs. Radius	131
B.3	Contour of Integration	134
B.4	Gauss' Law at $m=0$	139
B.5	Gauss' Law at $m > 0$	140
B.6	Calculation of E on Boundary	142
B.7	Variation of Charge Density With r	145

Preface

Philosophy

The birth of plasma physics as a discipline is most often associated with the advent of the fusion program in the late 50's. However, an equal impetus for a comprehensive understanding of plasma physics phenomena was generated by coincident advances in space physics. Both the space physics and the fusion communities owe a great deal to an even more recent discipline.

Up to a comparatively short time ago (1960's) the only approach to the many-body problems of plasma phenomena was the statistical one of solving the coupled Maxwell-Boltzmann equations or its moments - fluid theory - applied to an appropriate model. Alternatively, the experimentalist could construct an apparatus which closely matched the parameters under investigation and with suitable diagnostics, make desired measurements. In both instances the construction of a suitable model, to which the theory or an experiment could be tractably applied, was quite constrained, and certain simplifying assumptions were necessary in order to glean any useful information at all.

With analytic theory, once approximations were made and a solution found, many of the details of plasma behaviour could be obscured. For instance, reliance on Fluid Theory provided no information about wave-particle interactions. Similarly, experiments were limited, in that not all parameters could be measured. These measurements depended severely on the ingenuity and pursestrings of the experimenter. In many respects then the most useful results of theory and experiment are to demonstrate very general phenomena while application to specific phenomena were limited to embellishing the general results with appropriate detail - as for example, explanation of Whistler waves in the ionosphere.

With advent of powerful computers a radical new approach to plasma physics became possible. Instead of statistical solution to the many-body problem, one could actually follow the self-consistent trajectories of each particle in an ensemble. The data from each particle could be stored and used to provide an "exact" description of particles and fields.

Of course, this is an oversimplification. Computer time and memory are limited and other complications abound. First, the particles can only be followed in discrete steps so that a series of snapshots and not a continuous motion picture is possible. Second, calculations of the fields in a pair-wise manner was prohibitively time expensive and memory consuming. Third, the number of particles which could be followed, and therefore particle density, was generally much lower than that of the modeled phenomena. Finally, since the model is necessarily finite, questions about what to do with particles and fields at the boundaries is a thorny one.

All of these considerations mean that, while a powerful new tool exists to examine specific physical situations, the role of the modeler, the computational physicist, is an enormous one. Once the model has been constructed and successfully implemented for a particular situation, it is important to know that the model can be "scaled" to a broader range of additional problems.

Even more important than the code as implemented is the ability to organize and use a set of "tools" into working code. So, while useful results may be obtained using another's code, its construction or even its modification, clearly relies on the experience gained by doing. This experience is ultimately the most important product of this effort.

Acknowledgements

I dedicate this dissertation to a late friend of mine, Tom Johnson, who was so cruel as to interview prospective fellows with questions about plasma sheaths but wrote beautiful poetry about the family he loved. Thanks to the Fannie and John Hertz Foundation for their financial support during my three years study at Princeton. I am deeply indebted to many others for their always concern, often patience, sometimes encouragement, and occasional help in the years since.

Chapter 1

Introduction

Since 1958 when the Van Allen belts were discovered, we have come to recognize complex interactions between the sun and the earth coupled by the sun's plasma (the solar wind), its radiation (at the earth's ionosphere) and their magnetic fields (the earth's, the Interplanetary Magnetic Field (IMF), and current-driven magnetic disturbances.) One of the most intriguing and beautiful manifestations of these interactions is the aurora borealis.

As pictured in the accompanying sketch (Figure 1.1), observation of these aurorae is not new. Greeks recorded them many centuries ago but their name is attributed to Gassandi (1621)[12, p.15]. The detailed physical processes which lead to aurorae, however, are still being understood. The cause of the emissions themselves weren't known until the 50's when, from electron densities at the aurorae, they were linked to impact of energetic electrons upon oxygen molecules in the earth's ionosphere.

Since their discovery two different types of aurorae have been identified. (Figure 1.2). Diffuse aurorae are, just as their name implies, broad bands of light which appear almost continuously in the polar region sky. The broad distribution of electron energies which cause diffuse aurorae are associated with pitch angle scattering into the electron loss cone above the earth's dipole magnetic field.

In contrast, discrete (or Bright Active) aurorae, are identified as ribbons of light. In 1960 McIlwain [31, p.99] discovered a characteristic electron energy peak at 6 keV during discrete aurorae. For these energetic electrons to reach the earth, accelerating potentials must exist parallel to the earth's magnetic field [31, p. 99ff] and a source of energy must be available to drive



Figure 1.1: A woodcut by Fridtjof Nansen; Nansen depicts himself strolling on the ice under a triple curtain-like form of the aurora; the auroral arcs. (From Nansen's *Nord I Takeheunen*, 1911) [2, Cover Page].

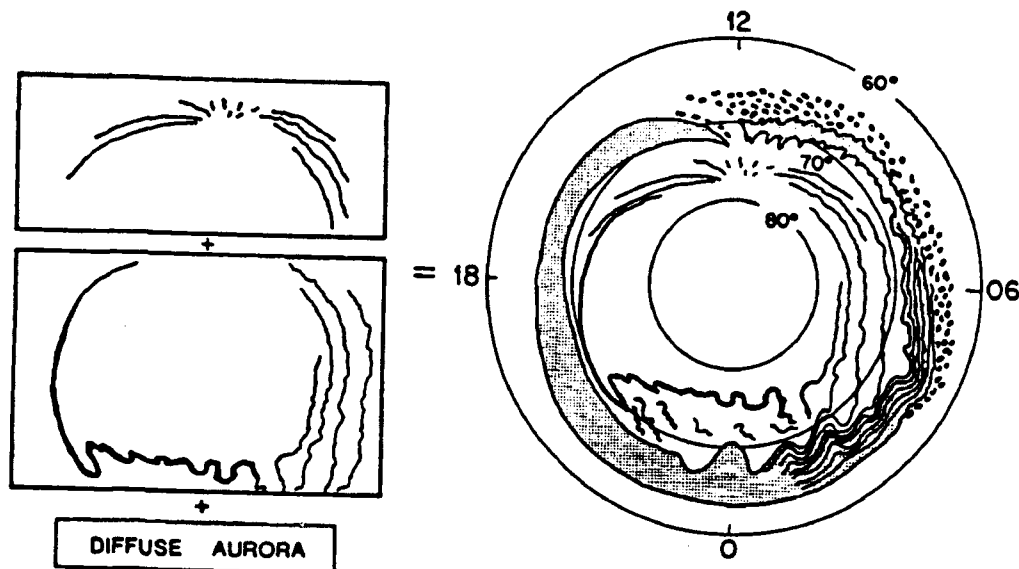


Figure 1.2: Schematic diagram showing the main characteristics of auroral displays, as seen from above the north geomagnetic pole. Auroral arcs are indicated by lines and the diffuse aurora is indicated by the shaded region. This is slightly modified from the original version given by Akasofu (1976) [2, p.4].

them.

Discrete aurorae are correlated with increased solar activity and the direction of the IMF with respect to the earth's dipole magnetic field. These in combination are believed to cause substorms. During these substorms plasma is observed to flow from the tailward region toward and away from the earth. As modeled by Sato [38] the energy involved in this flow results from externally driven magnetic reconnection.

A "semi-empirical" theory to substantiate plasma flows as a source of energetic electrons for substorm-generated aurorae is due to Serizawa and Sato[42]. They developed an expression for the potential drop between injection and loss boundaries required to preserve global charge neutrality. Their analysis revealed that for ion parallel kinetic energy, K , and temperature ratio, T_i/T_e , $e\phi_{MAX} \approx K/(1 + T_i/T_e)$ with only mild dependence on electron to ion mass ratios $m/M \ll 1$ and mirror ratios $B_{MAX}/B_0 \gg 1$. As noted by the authors, this theory yields no details about the nature of background particle interaction with the local potential.

Under the assumption of quasineutrality several authors have shown, both in theory [34],[52] and through numerical calculation [14], that large, long-scale length ($l \gg \lambda_D$) potential drops along magnetic field lines may develop self-consistently. Although this mechanism has been proposed as a candidate for acceleration of auroral electrons, results between differ-

ent models are contradictory and heavily dependent on assumed particle distributions. Further, the assumption of quasineutrality limits acquired solutions to only a subset of those actually possible.

Among alternatives proposed for electron acceleration are double layers (DLs) - potential drops over relatively short scale lengths ($\frac{e\phi}{T} \sim \frac{kT}{\lambda_d}$). Both strong ($e\phi \gg kT$) and weak ($e\phi \sim kT$) DLs have recently been observed above the earth's poles [49].

The role of double layers in laboratory and space plasmas has been the subject of much investigation. In an early analysis Block [6, p.349] modelled four species of particles—reflecting and passing, electrons and ions—incident upon a strong DL. Two fluid equations, an adiabatic equation of state, and Poisson's equation lead to criteria on the drift velocities of ions and electrons incident on the high and low potential sides of the DL, respectively. These are called Bohm criteria in analogy to similar criteria on ions in a plasma sheath[7, p.77]. An analogous Langmuir's condition [30, p. 973] leads to the perceived requirement for net current in all DLs.

Focussing on these criteria as a recipe, one could easily construct a DL. Plasma experiments and simulations required only fixed potentials at the boundaries to drive required currents or a floating potential (or even periodic boundary conditions) with large enough drifts between species. Because of these drifts, these plasmas were inherently unstable. (See Fig. 1.3.)

Just recently double layers have been demonstrated under more relaxed assumptions about boundary conditions and particle distributions. Some authors have found ways to relax the constraints imposed by the Bohm criteria. For example, Kan and Lee [25] concluded that the condition on the electron velocity is obviated by presence of trapped electrons. In their support simulations by Wagner showed double-layers to develop in the presence of just a current sheet[51].

Sato and Okuda [36,37] performed a series of simulations using even "more realistic" conditions. Their model (Fig. 1.4(a)) was that of polar region field lines in a self-consistent circuit (Fig. 1.4(b)). Initial conditions included a driving potential and current. The subsequent potential and current were related by a fixed resistance consistent with the initial conditions. Specifically, they assumed an electron drift velocity, $v_{de} < v_{the}$, and $T_e \gg T_i$. This is the range of parameters for ion-acoustic instabilities, but avoids the large relative drifts which may cause other two-stream

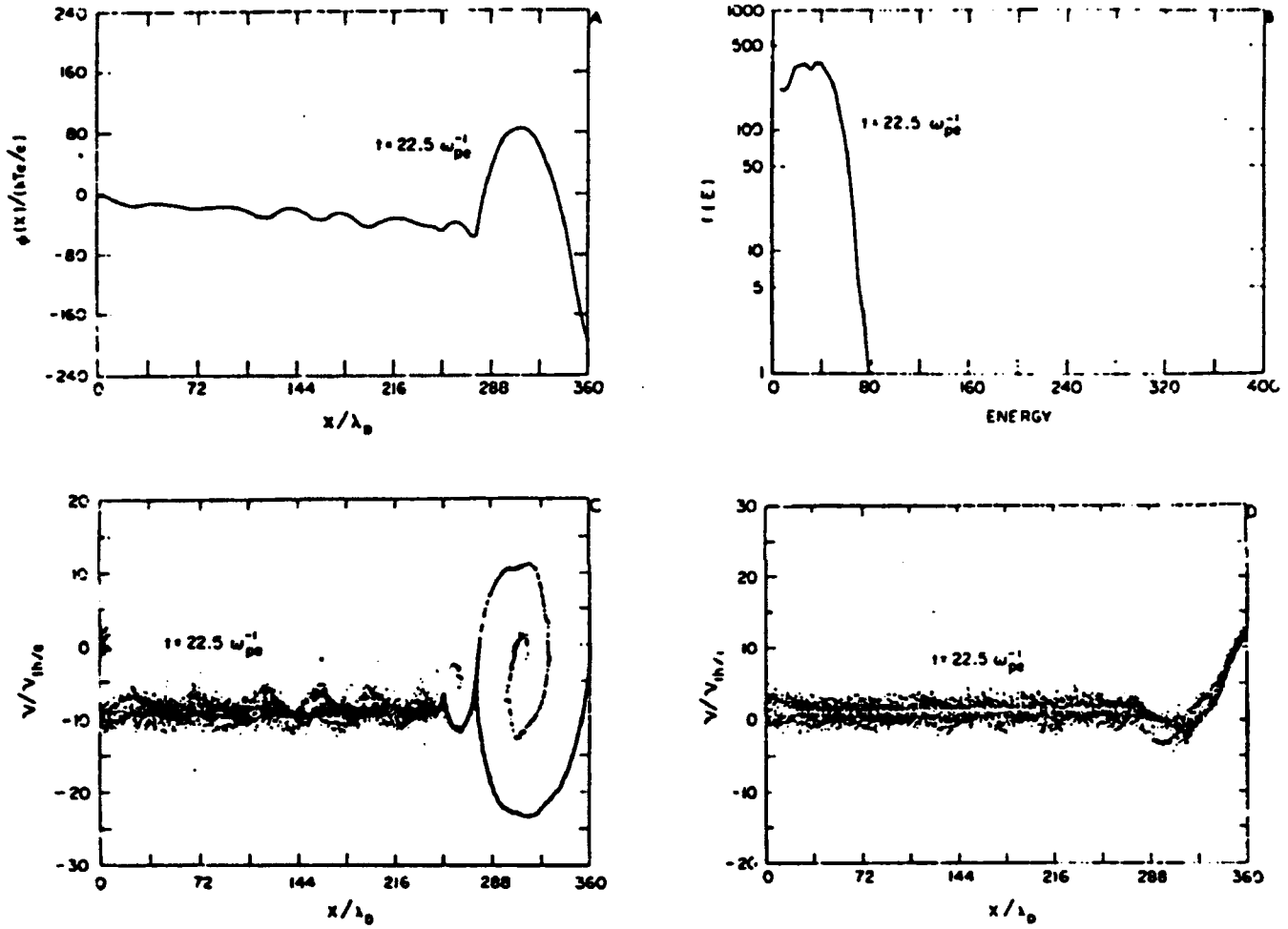


Figure 1.3: Initial propagation of a pulse driven by fixed potential boundary conditions. Top left: the potential profile. Top right: electron distribution function at the high-potential boundary. Bottom left: electron phase space. Bottom right: ion phase space. (After Hubbard and Joyce [35].) [43]

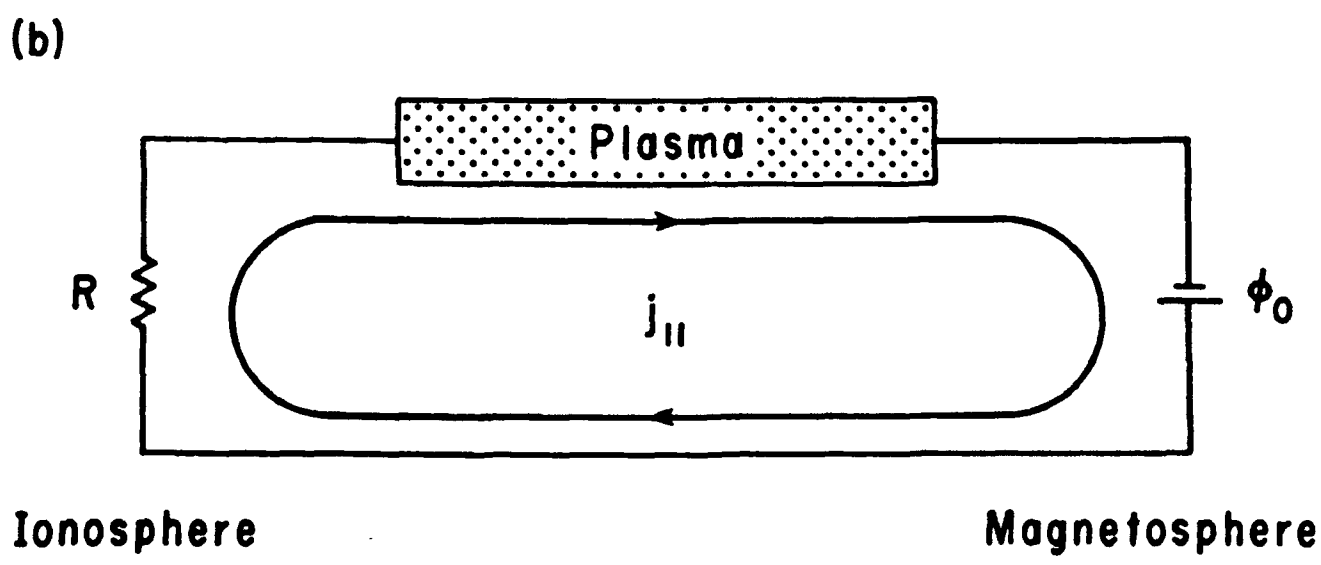
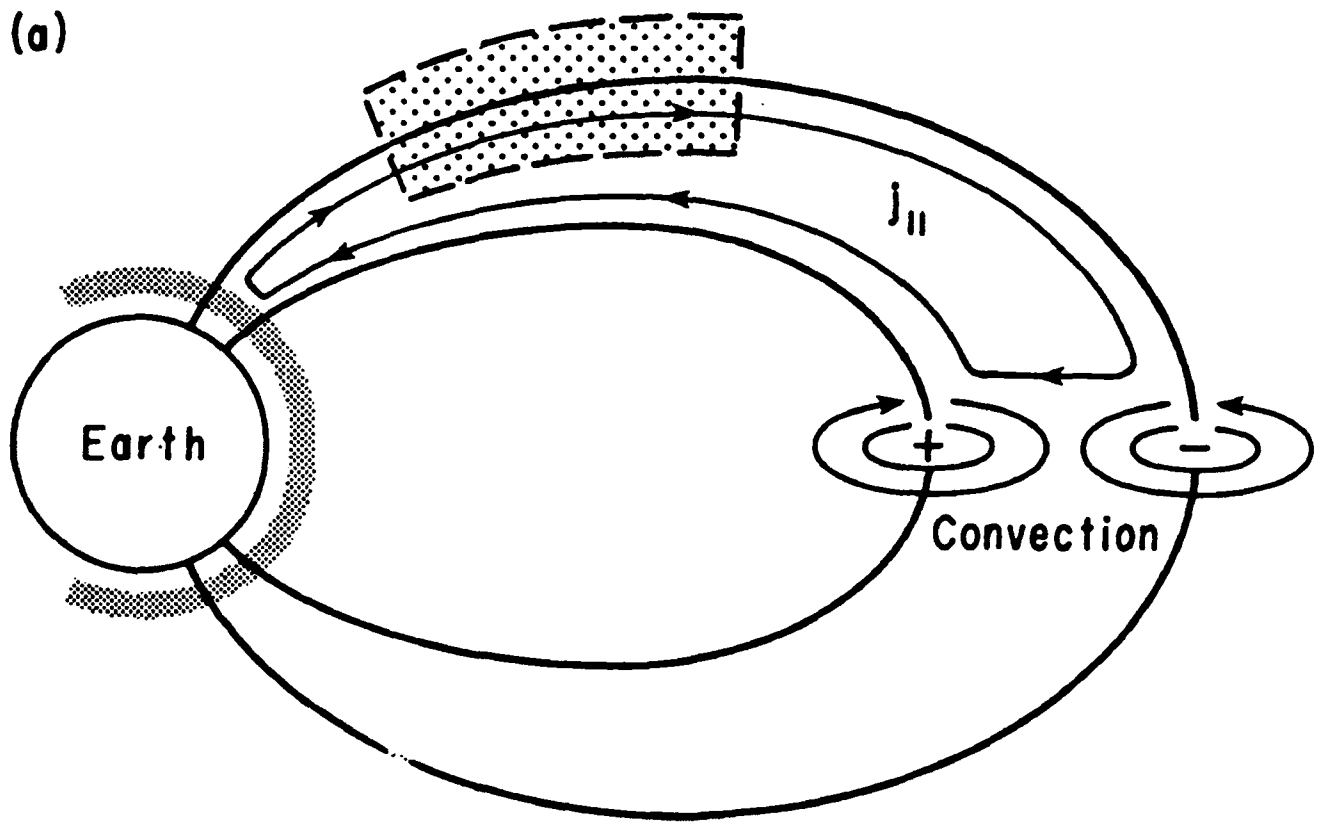


Figure 1.4: Model of polar region current driven by the convection electric field (a). The plasma is embedded in a self-consistent circuit (b) [37, p.3358].

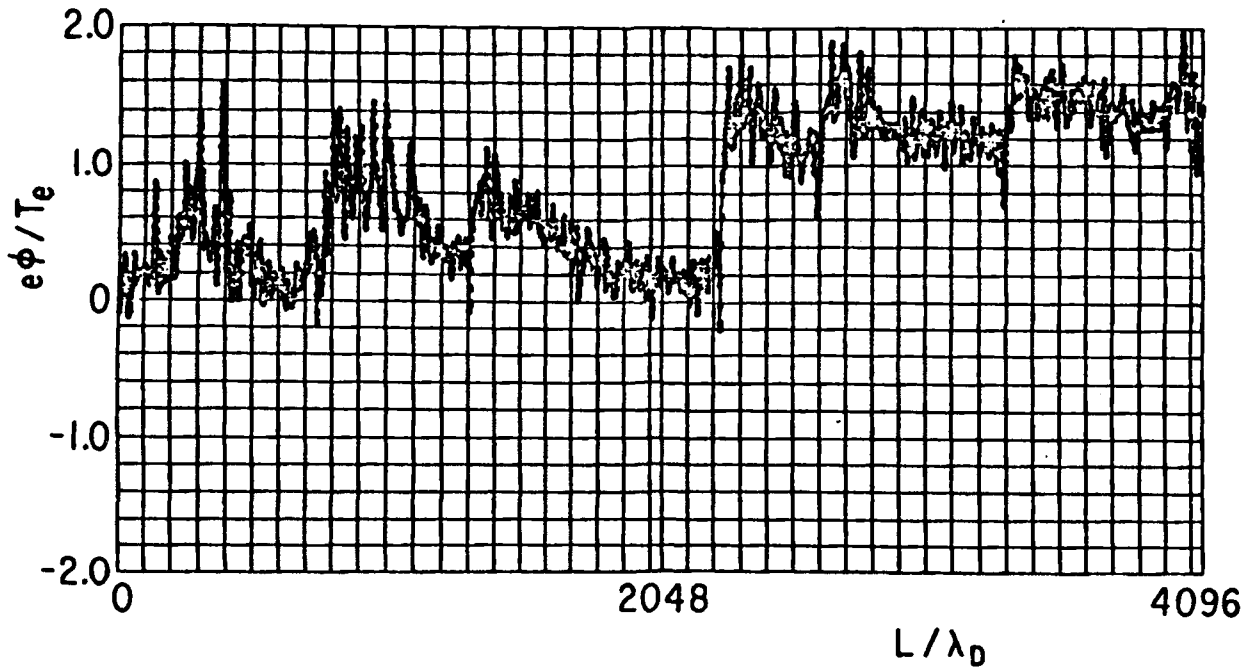


Figure 1.5: Sato and Okuda results exhibit multiple weak DLs. These DLs move with a velocity near the ion-acoustic velocity but recur so that the number of DLs is approximately constant[37, p.3364].

instabilities.

One of the results, shown in Figure 1.5, was obtained for $v_{de}/v_{the} = 0.6$. As apparent, the simulation resulted in multiple weak ($e\phi \sim T_e$) DLs about $1000\lambda_D$ apart and with scale lengths $l \sim 50\lambda_D$. These DLs are unstable and propagate at near the ion-acoustic velocity but recur at a rate such that the number of DLs is approximately constant.

Hasegawa and Sato [22] provided the theoretical mechanism for such DLs. Basically, an ion hole is created which cuts off the electron current. Formation of an adjacent electron hole follows. This yields a DL which decays on the ion time scale.

Most recently laboratory and theory experiments have demonstrated double layer solutions even under currentless conditions. Stenzel et al [44] conducted an experiment in which a dipole magnetic field reflected an incident ion beam. This experiment resulted in inherently currentless strong DLs for varying magnetic field strengths. Cohen et al modeled the likely formation of double layers in the throat of a mirror device[15]. Perkins and Sun [35] generalized their results by demonstrating eigenvalue solutions for currentless DLs.

Interestingly, quasineutrality does not preclude formation of double layers (DLs) [52, p.1526][45]. These results contrast with those like Chiu and Schultz' [14], using the condition of local charge neutrality to demonstrate the requirement for particular mixes of particle velocity distributions, but agree with more recent work by Stern, who includes double layers within an overall quasi-neutral framework.

As described in this introduction it is our goal to extend work on double layers to more realistic scenarios such as these "recent" theories, experiments, and simulations. Chapter 2 provides a brief survey of auroral physics, leading to a physical context for construction of our model. We are motivated by observations that aurorae are caused by energetic electrons. In particular, we examine one possible source of these electrons suggested by Sato et al [38], [42] that during substorms plasma flows earthward driven by magnetic reconnection in the tail region leading to large scale potentials to be explored by plasma constituents. Their results are supported by global calculations, however, and rely on static injection distributions. They therefore provide few details about the local behaviour of particles and the self-consistent electric potential in space and time. Alternative solutions exist which satisfy the boundary conditions of the global potential drop, injected particle distributions and background magnetic field.

In Chapter 3 we review theories and measurements from experiments and observations relevant to auroral double layers, and other plasmas immersed in a dipole magnetic field. Many of the previous theories suffer from the limited focus on global versus local analysis of potential solutions or ignore entirely the possibility for existence of double layers by excluding the class of solutions to which they belong. These deficiencies are partially due to unwarranted regard for thresholds and criteria rather than the underlying physics from which they were developed. This chapter has the simultaneous goal of exposing the reader to analytic and graphical techniques for analysing solutions to Poisson's equation. Use of both global charge conservation, requiring currentless boundaries, and local quasineutrality, exploring solutions to Poisson's equation by mapping $\Delta n = 0$, are accommodated by the same physics.

We have examined solutions to the Vlasov-Poisson equations using both analytic and computational models. Among the questions we ask: What is the local distribution of potential-double layer or otherwise? May they be currentless or do criteria prohibit formation of double layers? Are they

accessible? Do they persist or are they subject to instabilities? How do global and local approaches coincide?

In Chapter 4 we obtain both the global and local analytic solutions. These analyses weave together the theories of the previous chapter while developing observations and supporting the model assumptions for the simulations to follow. While Serizawa and Sato use “semi-empirical” methods to obtain a global requirement for large scale potential drops, we develop an analytic result. We analyze expected simulation results for the local potential using quasi-neutral techniques. In particular we assume Drifting Maxwellian particle distributions, beginning in the limit of cold temperatures for both T_{\perp} and T_{\parallel} and proceeding to finite values for both. The cold distribution is used explicitly by Schmidt [40] as an example of moving plasma behaviour, but is implicit in the assumed distributions of other authors [35], [15]. We find that the underlying global solutions retain their dependence on the injected ion kinetic energy even for finite T_{\perp} and T_{\parallel} but local DL solutions exist only for warm T_{\parallel} electrons.

None of the analytic techniques permit observation of temporal and spatial dependence. Particle simulations allow observation of both, thus demonstrating accessibility, the role of instabilities, interaction between the self-consistent particle distributions and how local requirements on the potential satisfy competing global boundary conditions. They permit observation beyond physically limited experiments (such as those in space) and give the “experimenter” more freedom in terms of flexibility and availability of “apparatus” and expenditure of time and money. Data can be stored and additional “non-intrusive” diagnostics performed. These diagnostics are limited only by the ingenuity of the computational physicist and simulation time and memory available.

Previous simulations were inadequate since they concentrated on periodic, non-bounded simulation regions or fixed potentials and lacked a realistic magnetic field and injection scheme. In Chapter 5, using particle simulation, we modeled a flowing neutral plasma injected along a (fully) dipole magnetic field. The computational model is that of a three-dimensional magnetic mirror with a one-dimensional (thus 1D) electrostatic solution to Maxwell’s equations lying along the mirror axis. A currentless, neutral (one-sided) Maxwellian plasma is injected at the low-field ($x=L$) side (e.g., magnetosphere) into an initially vacuum simulation region and propagates toward the high-field ($x=0$) side (e.g., the ionosphere.) Field boundary

conditions are $\phi(0) = 0$, $d\phi/dx(L) = -E(L) = 0$ [48]. Model diagnostics include phase-space plots; local charge densities, fields, and potentials; frequency and spatial spectra; and energy calculations. A variety of particle distributions, boundary conditions and equations of motion were used.

Both double layers and large scale potentials with $eV \gg kT$ are observed. The double layers move in correspondence with changes in velocity space distributions of incident particles. These changes coincide with observed instabilities. Movement of the double layer in time is associated with Langmuir's condition. Comparisons are made between theory and "experiment."

Extension of the simulation to two-dimensions offers the possibility to observe instabilities, transport processes and scale lengths not permitted in 1D, but modeling in 2D requires additional, sometimes subtle, considerations. In chapter 6 we describe construction of and results from a two-dimensional code. Comparison is made to behaviour in 1D.

In Chapter 7 we conclude by summarizing our contributions, suggesting future employment of our models and identify gaps yet to be explored.

General methods of particle simulation are described in a set of appendices to detail techniques and tools necessary for code construction. Important difficulties had to be overcome in the simulation of a plasma injected at a non-periodic boundary. In 1D we developed techniques to combat aliasing of Fourier transform solutions. In 2D we extended use of Buneman's algorithm [11] for solving Poisson's equation to mixed boundary conditions. In both codes we developed and used a guiding center pusher for electrons which permitted use of larger time steps. For this reason, although we initiated construction of these simulations with a particular application in mind, we emphasize these general aspects to relate the model's construction to possible follow-on investigation.

Finally, an extensive bibliography should add to the usefulness of this document as a reference source.

Chapter 2

Aurorae ¹

2.1 The Sun's Plasma and Magnetic Fields

The aurorae result from complex plasma phenomena under the influence of interactions between the sun and the earth. Regardless of their proximity, these plasmas remained relatively inaccessible until comparatively recently and their study is a relatively new branch of space physics. In this chapter we introduce the physics of these plasmas which provide motivation for our dissertation and a context within which to build analytic and computational models.

2.1.1 The Sun

The Sun is the major source of energy and a major source of particles for interactions manifest in phenomena such as aurorae. The core at the sun's center, heated by gravitational pressure, produces over 10^{26} W via p-p and carbon cycle fusions. This energy radiates out through the radiation zone producing X-rays, boils up through the convection zone and is visibly apparent in the photosphere. In this transit the temperature decreases from 10^7 °K at the core to 5×10^3 °K at the photosphere. However, in the outer chromosphere large amplitude acoustic or shock waves heat the gas of the

¹Except where otherwise noted, the substance of this chapter was gleaned from the 1986 Princeton University AS556 Lecture Notes, Selected Topics in Space Physics, by Professor Hideo Okuda [33]. Author references with years in parentheses are from these notes.

photosphere to 10^6K and densities continually decrease from 10^{17} cm^{-3} primarily neutrals to a plasma density of $10^6 - 10^9\text{ cm}^{-3}$ at the corona.

The corona is the location of many solar activities. Among these are solar flares and sunspots. Sunspots are dark spots (low temperature regions) on the sun's surface which are also observed to be local regions of strong magnetic fields ($\sim 1\text{kG}$) much larger than the normal sun magnetic field, a dipole of approximate magnitude $B=1$ Gauss with a 22 year reversal cycle. Sunspots are thought to originate from the wrapping of magnetic field lines as the sun rotates (Babcock, 1959). This model also describes the 11 year sunspot cycle with its familiar "butterfly pattern."

Solar flares violently release magnetic energy associated with these sunspots as the field lines buoy up above the coronal surface. The energy stored in solar flares is as much as 10^{32} ergs and can be released in tens of minutes. Its release may be explained by "driven" (Pettschek-Parker) magnetic field line reconnection. This mechanism may also be important in the Earth's magnetic tail.

Radiation from the sun may be approximated as blackbody at 5800°K and is the primary portion of energy released by the sun. At the earth this radiation is responsible for visible light-day and night-as well as production of the ionosphere, where the high frequency edge (UV and X-rays) of the radiated spectrum is absorbed.

2.1.2 The Solar Wind

The solar wind was first postulated by Biermann (1951) to explain the anti-sunward orientation of comets' tails. Radiation pressure alone was insufficient to account for this phenomena. Observations have since shown that typical earth parameters for the solar wind are $n=5\text{ cm}^{-3}$, $T=2 \times 10^5\text{K}$ and $u=400\text{ km/sec}$. The wind consists of 90% H and 10% He with a mean free path $l_{mfp} \sim 1\text{ AU} = 150 \times 10^6\text{ km}$ (500 light sec). The energy flux from the solar wind is $10^{13} - 10^{14}\text{ W}$ and is the driver for magnetospheric activity. One may readily verify that the kinetic energy density of the solar wind at the earth is much greater than its magnetic field energy density.

A theoretical foundation for the solar wind was advanced by Chapman (1958). His was a static model in which the pressure of the corona was balanced by the gravitational force. This model was unsuccessful in that the gravitational potential was too weak to contain the corona. An alternate

dynamic model, in which outgoing solar wind is replaced by solar gas, was more successful. A particular manifestation of this model is supersonic expansion of the solar wind ($M_A = 5$) in the gravitational throat of the sun.

2.1.3 Interplanetary Magnetic Field

The dipole field of the sun is dragged along by the solar wind. Because of the sun's rotation, the field lines form an Archimedes spiral. At the earth the resulting magnetic field points at an angle $\chi \sim 45^\circ$ to the line between the sun and earth in the sun's equatorial plane. The magnitude of the field at the earth is $\sim 5 \times 10^{-5} G$ and for distances much greater than the earth's is primarily in the ϕ direction. At large distances from the sun density decreases as $1/r^2$ while $B_{IMF} \propto 1/r$. An outward limit for the solar wind is obtained where magnetic pressure balances particle pressure at 50 AU, well beyond Pluto.

2.2 The Earth's Magnetosphere (See Fig. 2.1.)

2.2.1 The Earth's Magnetic Field

For up to about 10 earth radii the magnetic field of the earth is well modeled by a simple magnetic dipole produced by an infinitesimally small current loop. Such a field is characterized by its magnetic moment (\vec{m}) and is given by the formula [24, p. 182]

$$\vec{B} = \frac{3\hat{n}(\hat{n} \cdot \vec{m}) - \vec{m}}{|\vec{x}|^3}$$

Since the earth $\vec{m} = -m\hat{z}$, \vec{B} may be well expressed in cylindrical coordinates

$$\vec{B} = \frac{m}{r^3} \left[-\frac{3\rho z}{r^2} \hat{\rho} + \left(1 - \frac{3z^2}{r^2}\right) \hat{z} \right]$$

and its magnitude easily computed as

$$B = \frac{m}{r^3} \left(1 + \frac{3z^2}{r^2}\right)^{1/2}$$

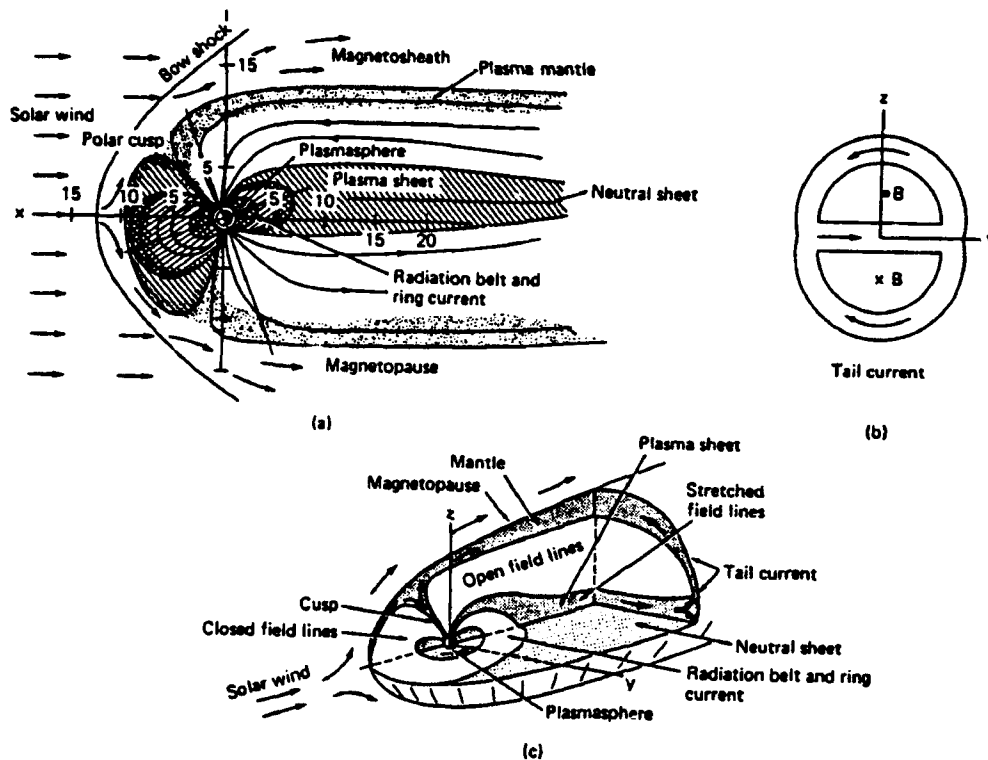


Figure 2.1: Schematic of major regions of the earth's magnetosphere. Auroral ovals encircle earth at ~ 100 km and in the $65^\circ - 75^\circ$ magnetic latitude band. (a) Noon-midnight meridian projection; (b) tail current system as viewed from sun; (c) three-dimensional perspective of (a) [31, p.1].

If the field is known at a given point, say \vec{x}_0 , then in terms of that field

$$B = B_0 \left(\frac{r_0^3}{r^3} \right) \left[\left(1 + \frac{3z^2}{r^2} \right) / \left(1 + \frac{3z_0^2}{r_0^2} \right) \right]^{1/2}$$

The magnitude of the earth's field at 1 earth radius is known to be .312 G at the equator (and .628 G at the poles.) The total field $\vec{B} = B\hat{b}$ is easily seen to be

$$\vec{B} = B_0 \left(\frac{r_0}{r} \right)^3 \left(1 + \frac{3z_0^2}{r_0^2} \right)^{-1/2} \left[-\frac{3\rho z}{r^2} \hat{\rho} + \left(1 - \frac{3z^2}{r^2} \right) \hat{z} \right]$$

and the two directions of $\hat{b} = b_\rho \hat{\rho} + b_z \hat{z}$ are given by

$$\begin{aligned} b_\rho &= -3 \frac{z}{r^2} \left(1 + 3 \frac{z^2}{r^2} \right)^{-1/2} \\ b_z &= \left(1 - 3 \frac{z^2}{r^2} \right) \left(1 + 3 \frac{z^2}{r^2} \right)^{-1/2} \end{aligned}$$

While the IMF represents but a small perturbation to the near earth magnetic field. B_{IMF} is approximately that of the earth at $r \sim \left(\frac{5 \times 10^{-5}}{3 \times 10^{-1}} \right)^{1/3} \approx 15$ earth radii.

2.2.2 The Magnetosheath

The first encounter of the solar wind with the earth's magnetic field is at the bow shock ($R \sim 15 R_E$) where the supersonic flow from the sun decelerates to subsonic with respect to v_A . The solar wind plasma heats in the magnetosheath exchanging kinetic for thermal energy, and is finally blocked at the magnetopause ($R \sim 10 R_E$) where the solar wind pressure balances pressures from the earth's magnetic field and particles in the magnetosphere, within which the earth's magnetic field is confined. The distant extent of the magnetosheath is $R \sim 200 R_E$ where the magnetic fields of the earth and the solar wind become comparable[31, p.86].

As the plasma flows past the earth, it drags along the earth's magnetic field creating two categories of field lines—open and closed. Subject to adiabatic constraints particles are free to enter or leave the earth's ionosphere primarily at the polar caps where the magnetic field lines are open. In absence of collisions or wave-particle interactions the solar wind may not penetrate the closed lines of the magnetosphere. However, two popular mechanisms have been proposed to allow for this occurrence.

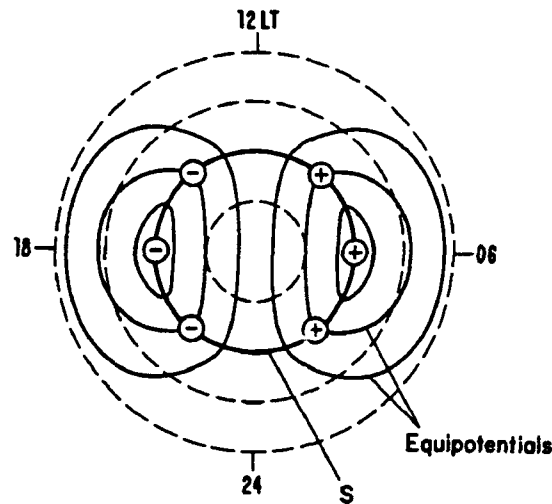


Figure 2.2: Mapping of the convection electric potentials and the surface S from the magnetosphere to the ionosphere, as seen from above the north pole [31, p. 60].

The first, proposed by Axford-Hines, invokes the Kelvin-Helmholtz instability as a source of “anomalous viscosity.” In this case the solar wind may penetrate the earth’s magnetic field on a steady state basis. Additionally, in periods of increased solar activity, when the IMF may acquire random components in the N-S direction, Dungey [31, p.56-59] theorized that a southward component would cause reconnection both sunward and anti-sunward of the earth, permitting free access of the solar wind into the earth’s magnetosphere.

2.2.3 Convection Electric Field

As the solar wind traverses the earth’s magnetic field, an electric field is mapped into the ionosphere along open dipole magnetic field lines. This field drives currents perpendicular to the magnetic field and establishes current patterns which map into polar caps. The observed value of this electric field is 20mV/m over the polar caps, amounting to an integrated potential of $e\phi \sim 50\text{ kV}$ [31, p.64]. In the polar region ionosphere this potential causes the flow of currents both perpendicular to the magnetic field and parallel (Pederson currents) and perpendicular (Hall currents) to the electric field[31, p.60]. Birkeland currents flow parallel to the magnetic

field.

2.2.4 Ionosphere

Nearest the earth the ionosphere covers the globe. Because of solar radiation and neutral density fall off with height, different regions of plasma may be identified. Below the E region (~ 100 km) the collision frequency is such that $\nu_{en} > \Omega_e$ and $\nu_{in} > \Omega_i$, above it $\Omega_e > \nu_{en} > \nu_{in} \geq \Omega_i$. As a result, the E region is the site of current amplification, and Hall conductivity dominates current flow in the ionosphere. Ionospheric plasma may exit through the polar caps creating the polar wind.

2.2.5 Plasma Sheet

Directly behind the earth the ambient polar wind collects to form the plasma sheet. The plasma sheet is the demarcation between the two oppositely directed components of the combined earth-IMF magnetic field. The sheet is populated with plasma particles $T = .1 - 10keV$, $n = .01 - 1cm^{-3}$ and $V = 10 - 1000km/s$ [31, p.2].

Because of the oppositely directed magnetic fields a current must flow in the neutral sheet region defined by $B=0$. This is known as the sheet current. The plasma sheet is a tremendous reservoir of solar wind energy $E \sim 3 \times 10^{22} - 10^{25}$ ergs[31, p.3]. Part of the sheet, known as the tail, stretches more than $200 R_E$ as estimated by mapping polar electric fields into the tail [31, p.86].

Examination of individual particle orbits as they enter the neutral sheet show that the particles are trapped and oscillate between opposite magnetic poles of the plasma sheet fields. Electrons and ions drift in opposite directions—the resulting current is in the direction of the electric field. The work done on the particles is $P \sim 10^{12}$ W[31, p.87].

Because of its current system, the sheet is particularly vulnerable to instabilities from reconnection (or tearing modes.) These instabilities make the sheet a source for other of the earth's regions.

2.2.6 Plasmasphere

Just outside the earth is the closed region known as the earth's plasmasphere. It is a cold ($T \leq 1$ eV) [31, p.2], dense ($n \sim 10^3$) region of plasma which ends abruptly at the plasmopause where the corotation field of the earth, $\vec{E}_c = -\vec{v}_R \times \vec{B}/c$, coupled to the convection electric field sweeps out the region between $R_E=3-6$ [31, p.76].

Throughout the region between the ionosphere and the sheet are the famous ring currents and radiation belts where high energy electrons and ions are trapped. The particles are responsible for a magnetic field depression, $\Delta B \sim 100snT$ [31, p.3], at the earth's surface during magnetic storms. This region also stores a significant amount of energy $\sim 2 \times 10^{22} - 10^{25}$ ergs [31, p. 2]. The rings are accelerated by ExB, Fermi and betatron acceleration and are depopulated by ion cyclotron waves and charge exchange [31, p. 3].

2.2.7 Plasma Parameters

Parameters throughout these regions are conveniently summarized in Fig. 2.3. Using $n=1-100 \text{ cm}^{-3}$, $B=10^2 - 10^4 \times 10^{-5}G$, and $T_e \leq T_i \sim 100's \text{ eV}$ yields $\omega_{pe} \sim \omega_{ce} \sim 10^5 - 10^6 \text{ rad/s}$ and $\beta \ll 1$. In this parameter regime the electrostatic approximation is appropriate [28].

2.3 Aurorae and Substorms

2.3.1 Diffuse Aurorae

The lights known as aurorae are caused by energetic electrons striking ambient molecules, primarily oxygen at the 4756\AA line, within the earth's ionosphere. Within the earth's magnetic field an electric field $\vec{E} = -\vec{v} \times \vec{B}$ forms to achieve a fluid force balance. The mapping of this field back into the tail drives the tail plasma earthward.

Electrostatic waves such as ES electron cyclotron harmonics have been shown to be responsible for scattering (primarily) convected electrons into the loss cone causing the diffuse aurora. The aurorae display characteristic patterns associated with return currents required to replenish these electrons.

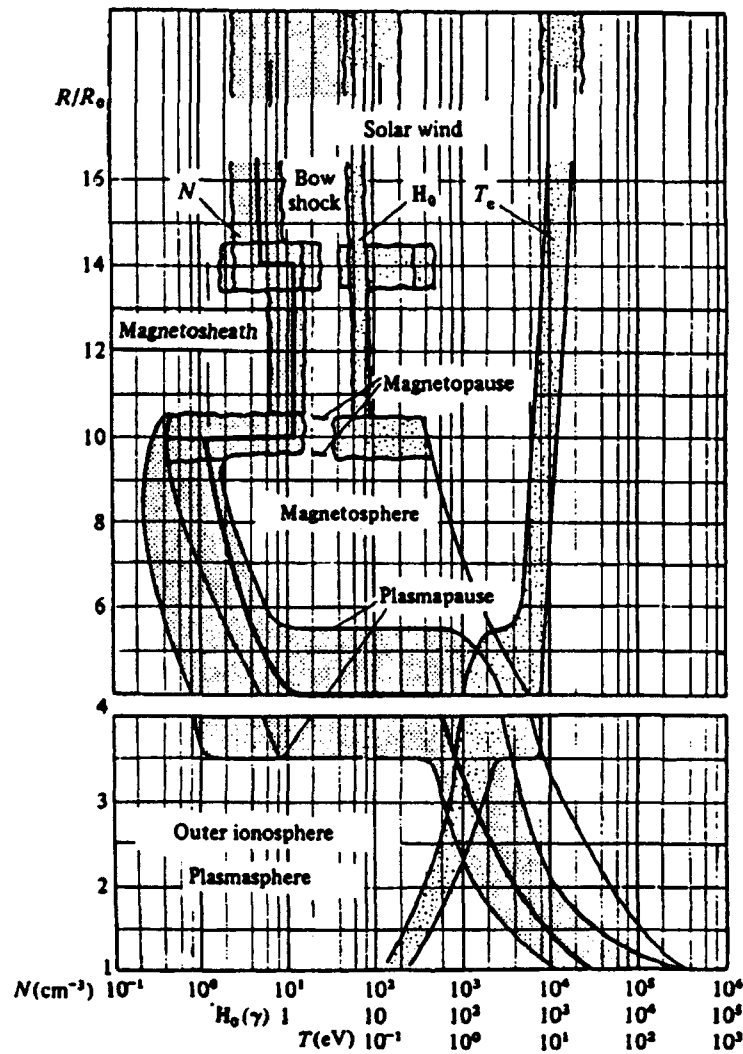


Figure 2.3: Model of the near-Earth plasma in equatorial regions and at middle latitudes; R/R_0 is the geocentric distance in Earth radii [3].

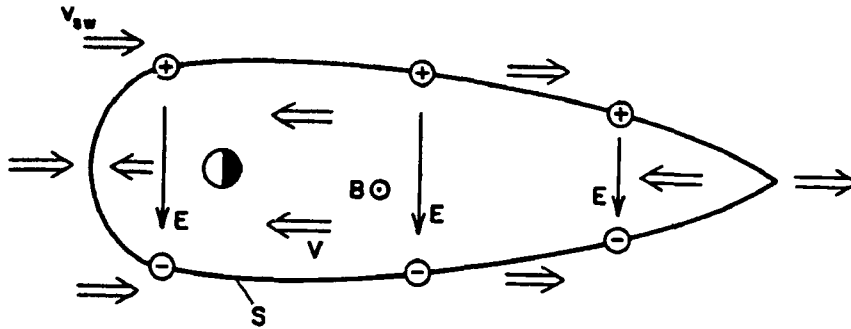


Figure 2.4: Illustration of convective flow V in the equatorial plane resulting from the superposition of the interplanetary and the earth's magnetic field. The surface S , charged as indicated, separates the regions of sunward and anti-sunward convection[31, p.59].

2.3.2 Discrete Aurorae

The visible forms of discrete aurorae have scale widths of $\sim 10km$ and are imbedded in larger scale $\sim 100km$ inverted V structures explained by current patterns established above. However, the current densities as measured for discrete aurorae, $j \sim 10^{-6} - 10^{-5} A/m^2$, cannot be explained by flows into a normal loss cone [31, p. 104]. The loss cone must be widened by parallel electric fields with integrated potential \sim few keV. Possible mechanisms for these fields include large scale potentials generated by suitable particle distributions or both strong and multiple weak DLs. Backscattered particles and Auroral Kilometric Radiation (AKR) from the RH extraordinary wave, rivaling Jupiter as a source of radio emissions, are associated with these potential structures[31, p.145].

2.3.3 Geomagnetic Substorms

During increases in solar activity changes in the solar wind and IMF take place. The plasma from the solar wind may collect at the plasma sheet more rapidly than it dissipates due to normal diffusion processes. Because the magnetic field is so low, the resulting system may be unstable, injecting plasma along field lines toward the polar caps to cause increased auroral

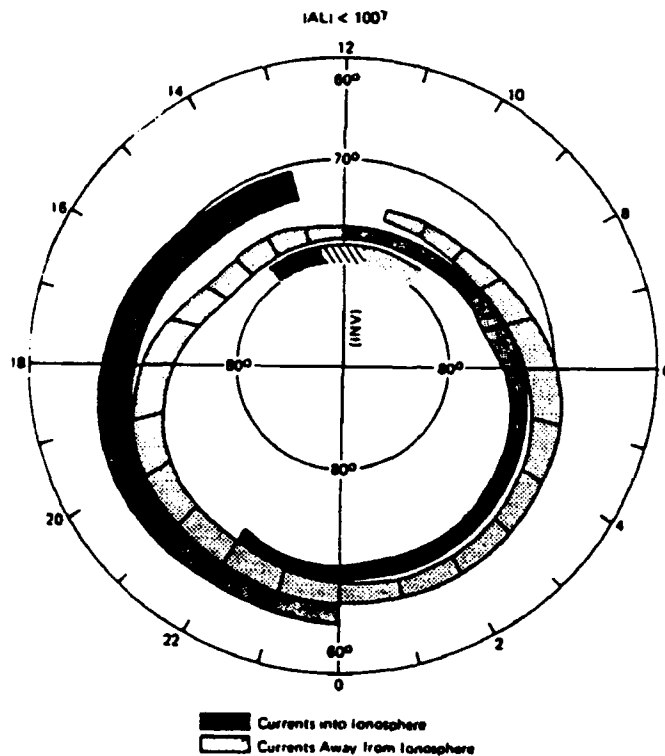


Figure 2.5: Summary of the distribution and directions of the large-scale field-aligned currents as determined from Triad satellite magnetic field observations. The hatched area near noon indicates confused current directions (from Iijima and Potemra, 1976b) (©by American Geophysical Union)[31, p.105].

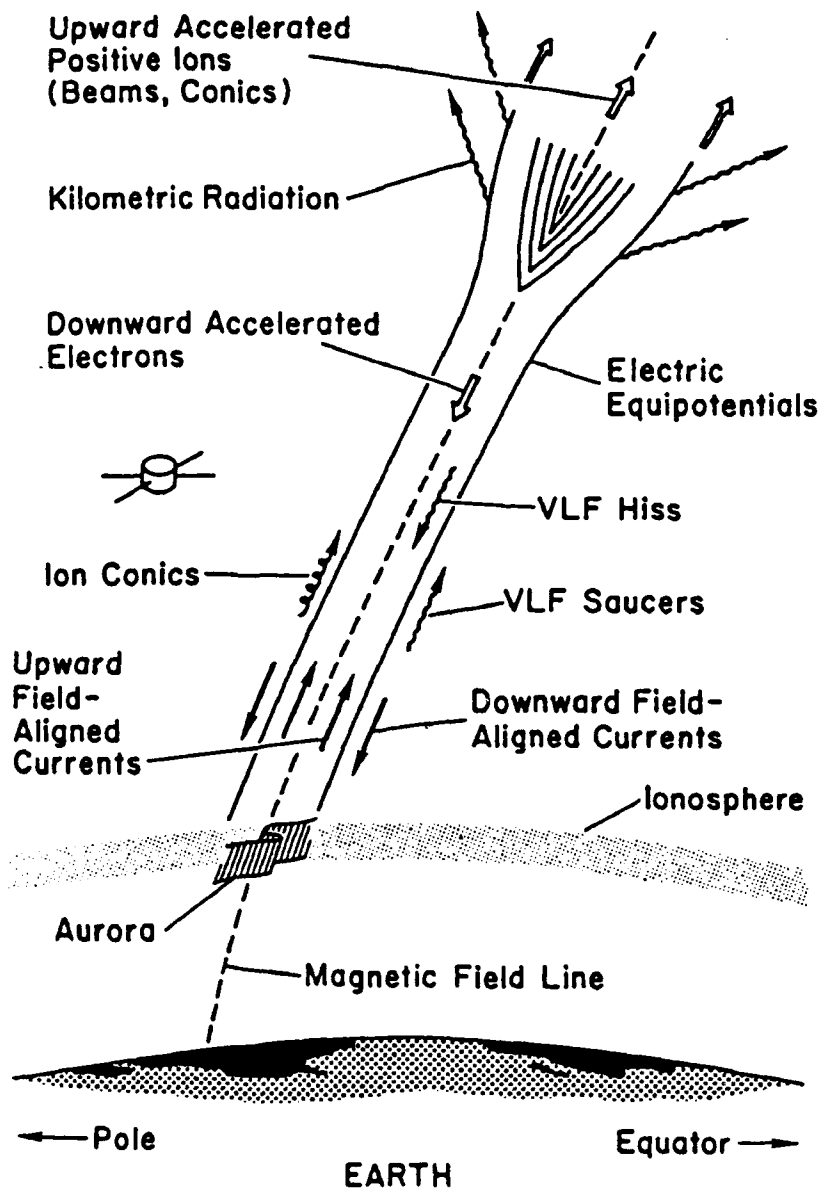


Figure 2.6: Schematic illustration, showing some of the interesting features associated with the auroral potential structure (P.B. Dusenbery)[2, p.13].

activity known as auroral storms. During these auroral storms, the ambient densities may increase above typical values.

Substorms are a subset of a storm and last for several hours while a storm may last several days. Substorms are associated with discrete aurorae and are evidenced by BEN (Broadband Electrostatic Noise) and ion conics.

The actual process for formation of a substorm is controversial. Substorms may be the result of local tearing mode instabilities and can cause a heightened flow of plasma toward the earth as well as a tailward flow known as a plasmoid. Parameters for this flow are $n=1-1 \text{ cm}^{-3}$, $V=100-1500 \text{ km/s}$, and $T_e < T_i \leq 2\text{keV}$. A substorm, related to tearing mode instabilities, is thought to be driven by some external source and this process is therefore called "driven reconnection."

2.3.4 Plasma Jet Theory

Using a 2D MHD model with anomalous resistivity, Sato simulated an externally driven magnetic reconnection creating strong plasma jets with speeds $\sim v_A \approx 500 \text{ km/s}$ [38]. Subsequently Sato and Hasegawa [39] developed a theory for this process. While tearing modes saturate at low flow velocity, externally driven flows have large velocities consistent with observation of strong jetting of protons [38, p. 7178].

A subsequent model of potentials generated from these flows is proposed as a mechanism for auroral electron acceleration. Serizawa and Sato showed that an equilibrium solution exists which is currentless and requires no trapped particles. To do this, they specified the particle distribution at an injection point into a mirror field and then used the currentless condition, $j_i = j_e$, to obtain the required maximum potential at the opposite boundary.

The injected distributions are

$$f_j(v_{\parallel 0}, v_{\perp 0}^2) = N_j \left(\frac{\alpha_j}{\pi} \right)^{\frac{3}{2}} e^{(-\alpha_j v_{\perp 0}^2)} \times \{ e^{[-\alpha_j (v_{\parallel 0} - u_j)^2]} - e^{[-\alpha_j (v_{\parallel 0} + u_j)^2]} \} \quad (2.1)$$

where $j=e,i$ and $\alpha = (\frac{m}{2T})$, u is the flow speed and N the particle density. For frequencies less than the ion cyclotron frequency but greater than collision frequencies we may assume that both energy and magnetic moment are conserved. From these assumptions the return flux at the injection point may be calculated. Imposition of $j_i = j_e$ then yields a solution for the

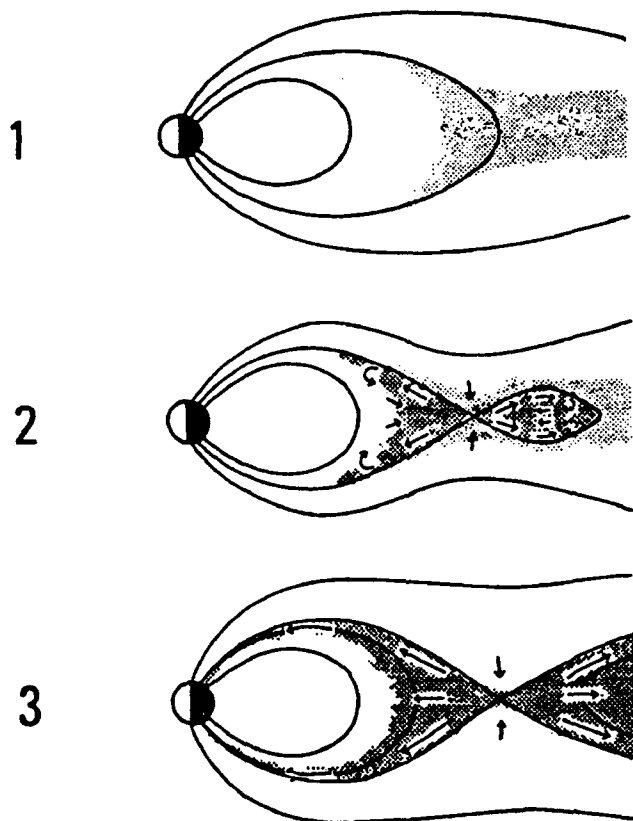


Figure 2.7: Sketches illustrate a model of the magnetotail structure change associated with magnetic reconnection. (Top) The normal state. (Center) A state of the magnetotail just after magnetic reconnection sets in. In this stage , accelerated plasmas on the earth side of the reconnection point are still trapped, and those on the antisolar side are confined in a magnetic island. (Bottom) Illustration of a stage of the substorm expansion in which trapped particles are precipitated down into the ionosphere and the magnetic island is propelled tailward [38, p. 7178].

maximum potential which may be obtained numerically as

$$e\phi_{MAX} = \frac{1}{2}Mu_0^2\left(1 - \frac{B_0}{B_{MAX}}\right)\left(\frac{T_e}{T_i} - \frac{m_e}{m_i}\right)\left(1 + \frac{T_e}{T_i}\right) \quad (2.2)$$

This scenario will serve as a model for our simulations and theory. Although this formalism does not specify the particle densities or potential at any point between the source point and throat, it provides a useful formula with which to compare our results. We shall devote the remainder of the dissertation to examining both global and local solutions for the potential and considering the relationship between these approaches. Additionally, this technique for obtaining the global potential will be used in Chapter 4 to analyze requirements for global charge neutrality.

Chapter 3

Sheaths and Double-Layers

The previous chapter introduced a method for determining global potential requirements for a bounded region. In this chapter we consider techniques for analyzing local self-consistent field/particle distributions and the resulting observations from their application.

3.1 Maxwell-Boltzmann Equations

Electromagnetic phenomena are governed by Maxwell's equations:

$$\nabla \cdot \vec{E} = 4\pi\rho \quad 3.1(a)$$

$$\nabla \times \vec{E} = -\frac{1}{c} \frac{\partial \vec{B}}{\partial t} \quad 3.1(b)$$

$$\nabla \cdot \vec{B} = 0 \quad 3.1(c)$$

$$\nabla \times \vec{B} = \frac{1}{c}(4\pi\vec{j} + \frac{\partial \vec{E}}{\partial t}) \quad 3.1(d)$$

These equations are familiar to us as Gauss' Law (3.1(c)), Poisson's Equation (3.1(a)), Faraday's Law (3.1(b)) and Ampere's Law (3.1(d)). Gauss' Law and Poisson's Equation may be treated as initial value conditions which, once satisfied, remain so by virtue of Faraday's and Ampere's Laws. It is often useful to define the electric field in terms of a scalar and vector potentials

$$\vec{E} = -\nabla\phi - \frac{1}{c} \frac{\partial \vec{A}}{\partial t}$$

with $\nabla \cdot \vec{A} = 0$, so that Poisson's equation may be equally well expressed as $-\nabla^2\phi = 4\pi\rho$.

The charge and current densities ρ and \vec{j} can be obtained by summing the zeroth and first velocity moments of the particle distribution function, (f), for each plasma component (α), weighted by its charge (q):

$$\begin{aligned}\rho &= \sum_{\alpha} q_{\alpha} \int d\vec{v} f_{\alpha} \equiv \sum_{\alpha} q_{\alpha} n_{\alpha} \\ \vec{j} &= \sum_{\alpha} q_{\alpha} \int d\vec{v} \vec{v} f_{\alpha} \equiv \sum_{\alpha} q_{\alpha} \vec{\Gamma}_{\alpha}\end{aligned}$$

The particle distributions in turn evolve according to the Boltzmann equation,

$$\frac{\partial f}{\partial t} + \vec{v} \cdot \nabla f + \vec{a} \cdot \nabla_{\vec{v}} f = - \left. \frac{\partial f}{\partial t} \right|_{coll}, \quad (3.2)$$

where the RHS of (3.2) represents “collisions”, essentially the particle/field interaction terms not included in its LHS. When the term on the RHS of (3.2) is small and collisions may be ignored, we have the Vlasov equation,

$$\frac{\partial f}{\partial t} + \vec{v} \cdot \nabla f + \vec{a} \cdot \nabla_{\vec{v}} f = 0 \quad (3.2a)$$

The acceleration, \vec{a} , is commonly given in terms of the Lorentz' force,

$$\vec{F} = m\vec{a} = q(\vec{E} + \vec{v} \times \vec{B}) \quad (3.3)$$

and couples these Maxwell-Boltzmann equations.

3.2 The Fluid Equations

The fluid equations derive from velocity moments

$$\int d\vec{v} \vec{v}^n (\dots)$$

of Boltzmann's Equation. These equations are not closed, since each involves one higher moment. “Closure” is obtained by truncating the series at some moment and replacing it with some reasonable form.

As presented above, one set of equations may be obtained for each plasma constituent. The fluid equations for a plasma of electrons and one specie of ions are commonly known as two-fluid theory and are familiar as

$$\text{equation of continuity:} \quad \frac{\partial n}{\partial t} + \nabla \cdot n\vec{v} = 0 \quad (3.4a)$$

$$\text{equation of motion:} \quad mn \left[\frac{\partial \vec{v}}{\partial t} + (\vec{v} \cdot \nabla) \vec{v} \right] = qn(\vec{E} + \vec{v} \times \vec{B}) - \nabla p \quad (3.4b)$$

where we have assumed a scalar pressure, p . Often, the isotropic ideal gas law, $p=nkT$, may be used. \vec{E} and \vec{B} obtain from Maxwell's equations (3.1) above.

Alternatively, by combining (adding or subtracting) these individual species equations, one obtains one-fluid theory. These are

$$\text{conservation of mass: } \frac{\partial \rho_m}{\partial t} + \nabla \cdot (\rho_m \vec{v}) = 0 \quad (3.5a)$$

$$\text{conservation of charge: } \frac{\partial \rho}{\partial t} + \nabla \cdot \vec{j} = 0 \quad (3.5b)$$

$$\text{equation of motion: } \rho_m \frac{\partial \vec{v}}{\partial t} = \vec{j} \times \vec{B} - \nabla p + \rho_m \vec{g} \quad (3.5c)$$

$$\text{Generalized Ohm's Law: } \vec{E} + \vec{v} \times \vec{B} = \eta \vec{j} + \frac{1}{en} (\vec{j} \times \vec{B} - \nabla p_e) \quad (3.5d)$$

In the above, mass flow is dominated by the ions while electrical properties tend to depend on the electron's motion. The resistivity η is defined by the first velocity moment of the collision term in Boltzmann's equation (3.2).

3.3 Useful Idealizations

3.3.1 Quasi-Neutrality (Plasma Approximation)

By nature a plasma tends toward charge neutrality. (Opposite charges attract, like charges repel.) A useful approximation is to assume that the densities of ions and electrons are equal

$$\Delta n \equiv n_i - n_e = 0 \quad (3.6)$$

This assumption is known as the plasma approximation or quasineutrality. Of course, with this assumption the value of the electric field can no longer be freely determined directly from Poisson's equation but must instead come from some other means such as the fluid equations (3.4) and (3.5).

It is useful to examine the validity of the plasma approximation. We do so in one-dimension. For a single ion species Poisson's equation (3.1(a)) can be rewritten by changing variables to

$$\frac{d^2 V}{dX^2} = N_i - N_e \quad (3.7)$$

where $\lambda_D = \sqrt{\frac{kT}{4\pi n e^2}}$, $N \equiv n/n_0$, $n_0 \equiv n_i + n_e$, $V \equiv -e\phi/kT$, and $X \equiv x/\lambda_D$. (See [43, eq(14)].) Since $|N_e|$ and $|N_i| \leq 1$, $|N_i - N_e| \leq 1$ and, averaging

Poisson's equation over a scale length, L ,

$$\frac{1}{L} \int_0^L dX \left(\frac{d^2 V}{dX^2} \right) = -\Delta \left(\frac{d \frac{e\phi}{kT}}{dX} \right) = \langle N_i - N_e \rangle \leq 1$$

where $\langle \dots \rangle$ denotes the average $\frac{1}{L} \int_0^L dX (\dots)$. Quasineutrality holds when $|\Delta \frac{d \frac{e\phi}{kT}}{dX}| \ll 1$ or the scale length for the change in slope of the potential is much greater than a Debye length. This is trivially true for $|\frac{e\phi}{kT}| \ll 1$ over the same interval. Although quasineutrality may not hold locally, it must hold in the macro sense, even in the formation of sheaths and DLs[45].

3.3.2 The Adiabatic Approximation

The steady-state Vlasov equation may be easily solved for the case of one-dimensional electrostatic fields and a mirror force. When the magnetic moment, μ , is an adiabatic invariant, the force on the particles may be expressed in terms of a scalar potential ($\Phi = q\phi + \mu B$):

$$F = -\frac{d\Phi}{dx} = -q \frac{d\phi}{dx} + \mu \frac{dB}{dx}$$

Entering this for the acceleration term, the steady-state Vlasov equation becomes

$$v \frac{\partial f}{\partial x} - \frac{1}{m} \frac{d\Phi}{dx} \frac{\partial f}{\partial v} = 0$$

and may be rewritten as

$$\frac{\partial f}{\partial V} - \frac{\partial f}{\partial K} = 0$$

where $V = \Phi/kT$ and $K = 1/2mv^2/kT$.

Treating V and K as coordinates in two space, we see that

$$\nabla f \cdot (\hat{i} - \hat{j}) = 0$$

where $\vec{V} = V\hat{i}$, $\vec{K} = K\hat{j}$ and $\nabla \equiv \frac{\partial}{\partial V}\hat{i} + \frac{\partial}{\partial K}\hat{j}$. We may represent this equation graphically as a function (f) whose gradient is orthogonal to the direction of $\hat{i} - \hat{j}$. (See Figure 3.1.) The solution to this equation corresponds to rotating the axes 45° such that ∇f lies perpendicular to the family of curves $H=K+V=\text{constant}$. Therefore f is a member of the family of functions, $f(H+c)$, c constant. The reader may recognize lines parallel to

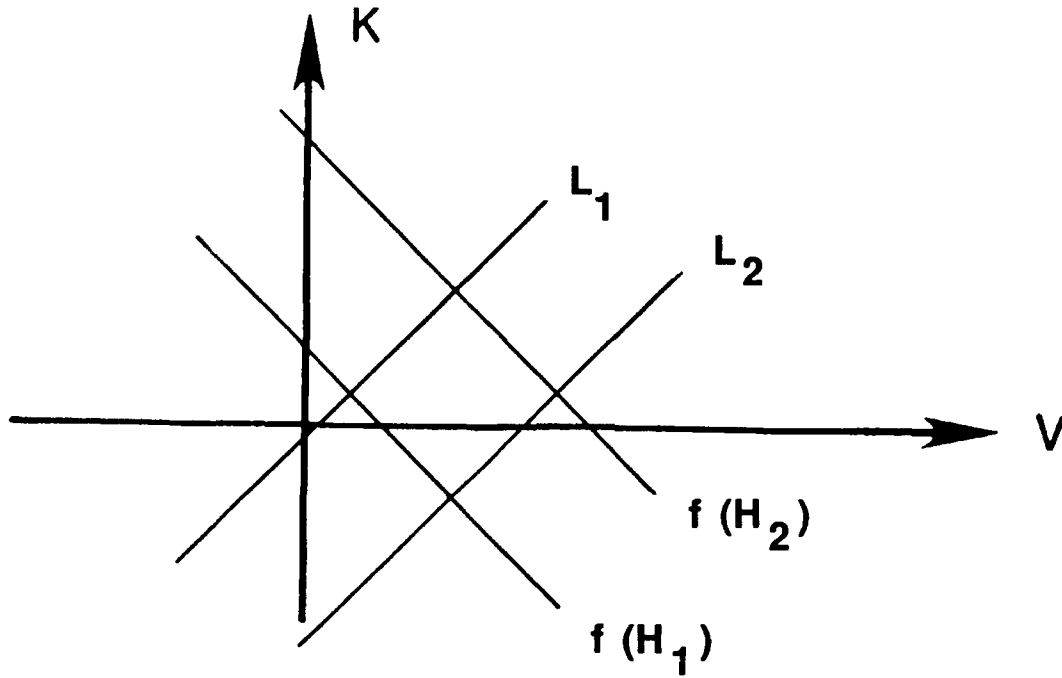


Figure 3.1: K-V Plane showing lines of constant $K \pm V$. These lines may be identified with the Hamiltonian, $H=K+V$, and the Lagrangian, $L=K-V$.

∇f as defining a set of Lagrangians, $L \equiv K-V = c_{1,2,\dots}$, while H may be identified as the Hamiltonian.

If we use the boundary condition that f is a drifting Maxwellian in the absence of a potential (at $V=0$), we know that

$$f(K + c) = f_M,$$

and c just determines the constant of normalization. To maintain this functional form, $f(H) = f_M e^{-\Phi/kT}$. This is simply the Boltzmann or adiabatic distribution. For a cold species ($T=0$) the contribution to the Maxwellian occurs only at $\mathcal{E}=\text{constant}$. This is equivalent to conservation of energy.

A more familiar version of the adiabatic approximation is obtained from the first law of thermodynamics when we insist that an ideal gas remains isolated ($TdS=0$) during a process (See Fig. 3.2.)

$$\begin{aligned} TdS &= dW + dU = 0 \\ dW = pdV &= p(d\frac{1}{n}), \quad p=nkT \text{ (ideal gas)} \\ U &= N(\frac{1}{2}mu^2 + q\phi + \mu B) \equiv \mathcal{E} \\ -kTd \ln n &= d(\frac{1}{2}mu^2 + q\phi + \mu B) \\ n &= n_0 e^{-\mathcal{E}/kT} \end{aligned}$$

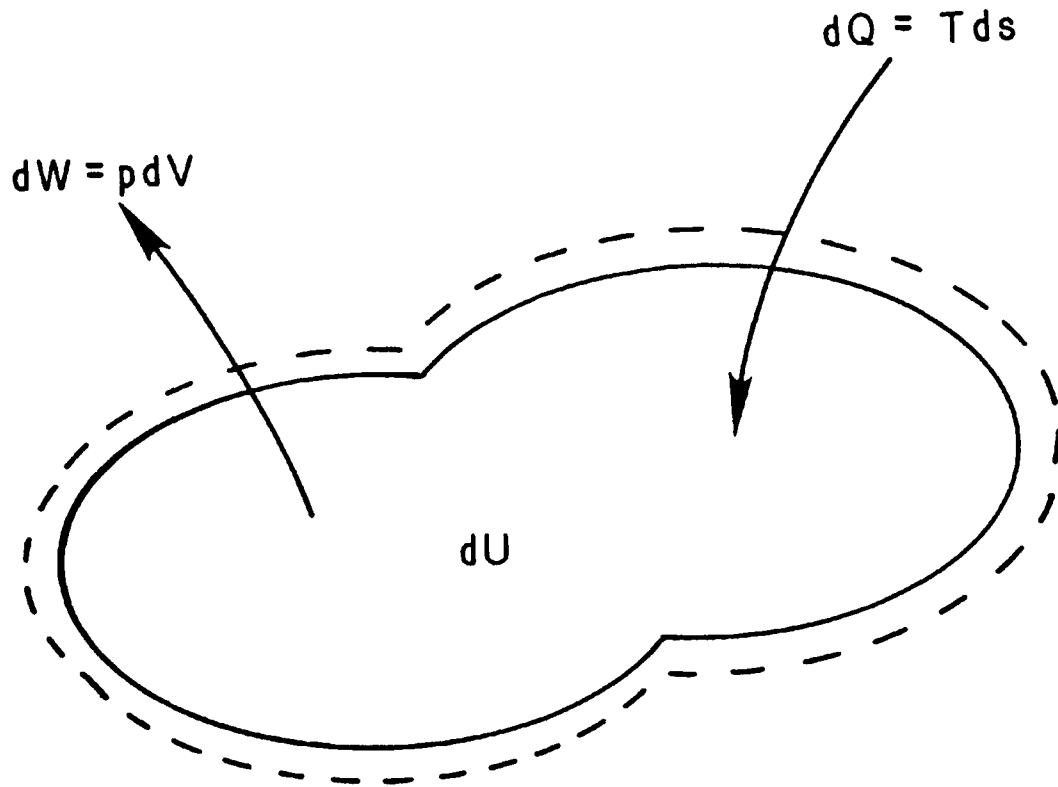


Figure 3.2: Diagram depicting flow of energy into and out of an isolated control volume.

In practice the adiabatic approximation is used when the distribution has time to reach thermodynamic equilibrium—when we know that we have a Maxwell-Boltzmann distribution—but before species have time to exchange energy with other species (or waves.)

3.4 Sheaths

3.4.1 One - Dimensional Sheath

The solution for the electric potential in a plasma of warm electrons and cold ions in contact with a conducting wall is attributed to Langmuir. This geometry is depicted at Figure 3.3. To the left of $x = 0$ we take $\vec{E} = 0$, implying $n_i = n_e = n_0$. We use the adiabatic equation of state for electrons,

$$n_e = n_0 e^{\frac{e\phi}{kT}},$$

and combine the equation of continuity (3.4a)

$$\begin{aligned} \nabla \cdot (n\vec{v}) &= 0 \\ (nv)_0 &= (nv) \end{aligned}$$

and conservation of energy

$$\begin{aligned} \frac{1}{2}Mv^2 + e\phi &= \frac{1}{2}Mv_0^2 \\ v &= \sqrt{v_0^2 - \frac{2e\phi}{M}} \end{aligned}$$

to obtain the ion particle density

$$n_i = n_0 \left(1 - \frac{e\phi}{\frac{1}{2}Mv_0^2}\right)^{-\frac{1}{2}}$$

Substituting into Poisson's equation (3.1(a)) and defining $V = \frac{-e\phi}{kT}$, we obtain

$$\frac{d^2V}{dX^2} = \left(\frac{1}{\sqrt{1 + \frac{2V}{\mathcal{M}^2}}} - e^{-V}\right)$$

where the scale length and debye length are defined above and the Mach number is defined as $\mathcal{M} \equiv \frac{v_0}{c_s}$ in terms of the sound speed $c_s \equiv \left(\frac{kT}{M}\right)^{\frac{1}{2}}$.

Multiplying by $\frac{dV}{dX} \equiv \xi$ and using $\xi_0 = 0$ leads to:

$$\begin{aligned} \frac{1}{2} \frac{d}{dX}(\xi^2) &= \frac{d}{dX} \left[\left(1 + \frac{2V}{\mathcal{M}^2}\right)^{\frac{1}{2}} \mathcal{M}^2 + e^{-V} \right] \\ \frac{1}{2} \xi^2 &= \left(1 + \frac{2V}{\mathcal{M}^2}\right)^{\frac{1}{2}} \mathcal{M}^2 + e^{-V} - \mathcal{M}^2 - 1 \end{aligned}$$

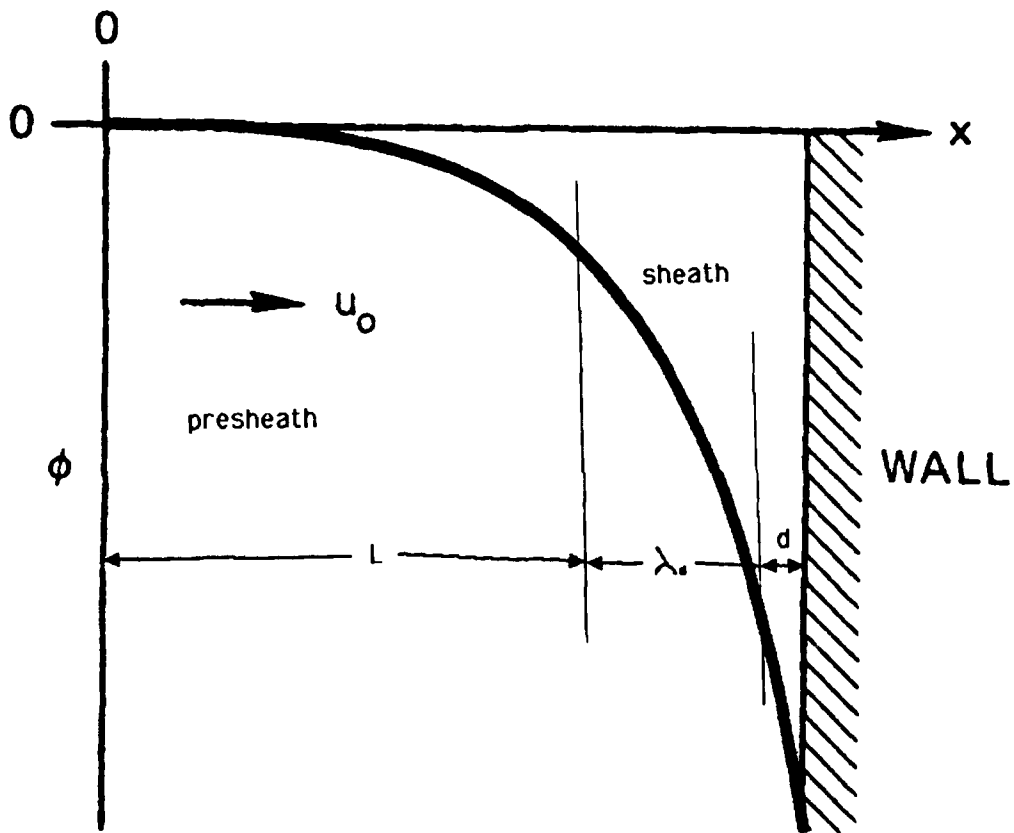


Figure 3.3: The potential ϕ in a planar sheath. Cold ions are assumed to enter the sheath with a uniform velocity u_0 . The regions of the sheath are marked as the presheath, sheath and anode (d) [13, p.245].

This equation can only be satisfied for

$$1 + \mathcal{M}^2 < \left(1 + \frac{2V}{\mathcal{M}^2}\right)^{\frac{1}{2}} \mathcal{M}^2 + e^{-V}$$

when $\xi^2 > 0$. For small V , near $X = 0$ [13, p.246],

$$\begin{aligned} \frac{1}{2}V^2\left(1 - \frac{1}{\mathcal{M}^2}\right) &> 0 \\ \text{so } \mathcal{M}^2 &> 1 \text{ or} \\ v_0 &> c_s \end{aligned}$$

Equivalently, we may require for self-consistency that at $V=0$ $\frac{\partial \Delta n}{\partial x} > 0$ and $\xi > 0$,

$$\begin{aligned} \left[-\frac{1}{2}\left(1 + \frac{2V}{\mathcal{M}^2}\right)^{-3/2} \frac{2}{\mathcal{M}^2} + \exp -V\right] \frac{\partial V}{\partial x} &> 0 \\ \exp -V &> \left(1 + \frac{2V}{\mathcal{M}^2}\right)^{-3/2} \frac{1}{\mathcal{M}^2} \\ \mathcal{M}^2 &> 1 \\ v_0 &> c_s \end{aligned}$$

as before. This condition is known as the Bohm-Sheath criterion and specifies a minimum ion injection velocity, v_0 , for the formation of sheaths. Alternatively, this criteria has been shown above as a condition on the slope of the relative charge density. We will exploit this equivalence in observations to follow.

The demarcation between the sheath and the presheath is marked by the existence of a quasineutral or "plasma" solution (eqn. 3.6). This is evident in Langmuir's evaluation of low-pressure, long mean free path plasma, as pictured in Fig. 3.4. The reader should note that the formal plasma solution is double-valued in ϕ and no unique "plasma" solution exists beyond $s = s_0$.

Outside the sheath region in the presheath, v is arbitrary. To get a velocity $v > c_s$, there must be an accelerating electric field in the presheath plasma while still satisfying the condition of quasineutrality. This condition may still be satisfied provided the scale length is long. The field itself comes from the distribution of ions and electrons produced within the plasma.

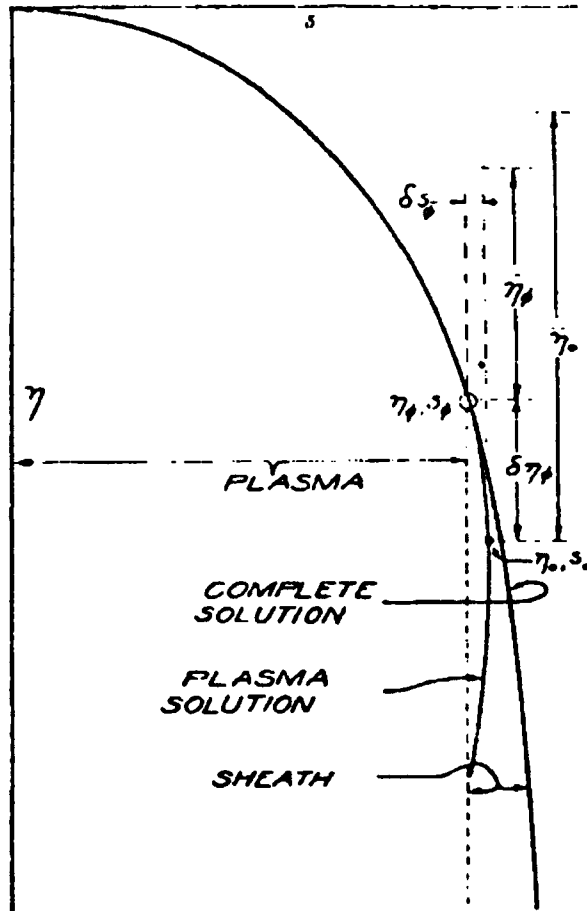


Figure 3.4: The relation of the plasma and complete solutions of the plasma-sheath integral equation [50, Fig. 6, p.902]. (Here η and s correspond to the variables ϕ and x .)

At some point near the wall the contribution of electrons to the space charge becomes negligible. Ignoring this contribution, we calculate a potential as measured from the sheath boundary.

$$\begin{aligned}\frac{\partial^2 \phi}{\partial x^2} &= 4\pi n_0 e \left(1 - \frac{e\phi}{\frac{1}{2} M v_0^2}\right)^{-\frac{1}{2}} \\ \frac{1}{2} \frac{\partial}{\partial x} \left(\frac{\partial \phi}{\partial x}\right)^2 &= 4\pi n_0 M v_0^2 \frac{\partial \left(1 - \frac{e\phi}{\frac{1}{2} M v_0^2}\right)^{\frac{1}{2}}}{\partial x} \\ \frac{\partial \phi}{\partial x} &= -\left[8\pi n_0 M u_0^2 \left\{1 - \frac{2e\phi}{M u_0^2}\right\}^{\frac{1}{2}} - 1\right] - \left(\frac{\partial \phi}{\partial x}\right)_0^{\frac{1}{2}}\end{aligned}$$

For $\frac{2e|\phi|}{M u_0^2} \gg 1$ and $\left(\frac{\partial \phi}{\partial x}\right)_0^2 \ll 8\pi n_0 M u_0^2 \left(\frac{2e|\phi|}{M u_0^2}\right)^{\frac{1}{2}}$,

$$\begin{aligned}-\frac{\partial \phi}{\partial x} &= \left[8\pi n_0 M u_0 \left(-\frac{2e\phi}{M}\right)^{\frac{1}{2}}\right]^{\frac{1}{2}} \\ 4/3 \frac{\partial |\phi|^{3/4}}{\partial x} &= \left[8\pi n_0 M u_0 (2e/M)^{\frac{1}{2}}\right]^{\frac{1}{2}} \\ |\phi|^{3/4} &= 3/4 \left[8\pi n_0 M u_0 (2e/M)^{\frac{1}{2}}\right]^{\frac{1}{2}} x\end{aligned}$$

For a thickness d , the current density, j_0 , is related to ϕ by

$$j_0 = 4/9 (2e/M)^{\frac{1}{2}} \frac{\phi_d^{\frac{3}{4}}}{4\pi d^2} \quad (3.8)$$

This is known as the Child-Langmuir law for space charge limited flow [13, p. 248]. j_0 is established such that global charge neutrality is maintained and is fixed by the ion production rate. ϕ_d is such that the flow of electrons is equal to the ion flow rate. d then changes to suit these two parameters. A similar relationship is obtained for a cold, zero field cathode where d is the distance between the cathode (injection point) and the anode at potential ϕ_d . We shall exploit these facts in the analyses that follow.

3.5 Double Layers with Current

3.5.1 Double Sheaths

A similar analysis to the last can be made for the case of cold ions and electrons incident upon a potential drop within a plasma. This analysis

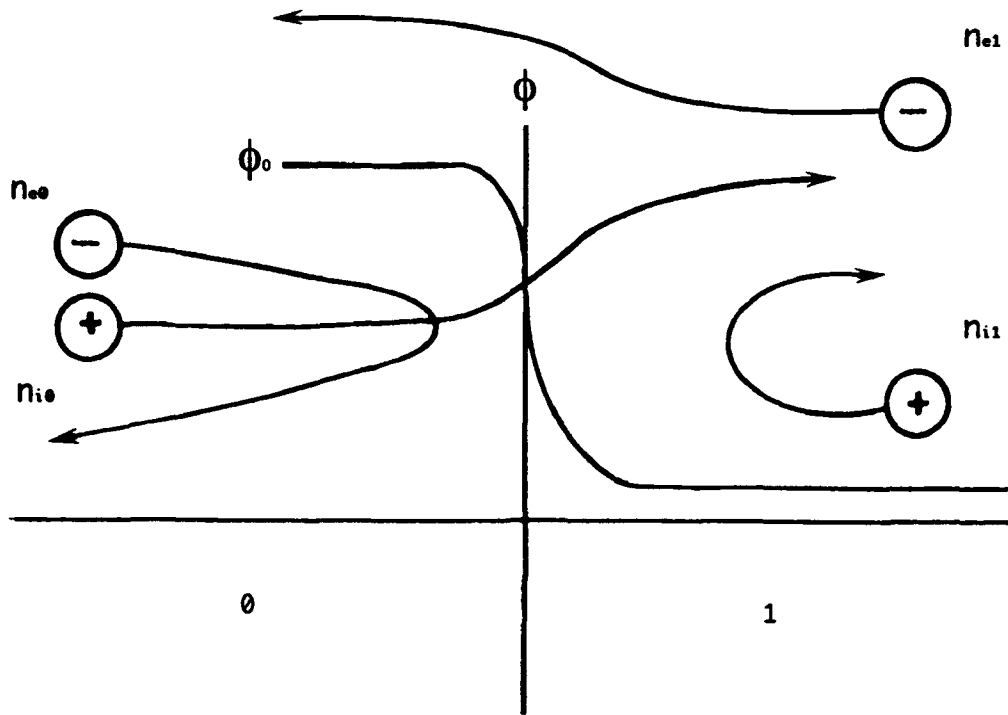


Figure 3.5: A generic model for double layer analysis with passing and trapped ions and electrons in each region 0 and 1. The height of the lines indicate the relative velocities of charges in response to the potential, ϕ .

involves participation of four different species— passing and trapped, electrons and ions. (See Figure 3.5.) The following set of equations relate the particle boundary conditions to the potential:

$$\begin{aligned}
\text{Flux:} \quad & (nu)_i = (nu)_{i0} \quad , \quad (nu)_e = (nu)_{e1} \\
\text{Energy:} \quad & \frac{Mu_i^2}{2} = e(\phi_0 - \phi) \quad , \quad \frac{mu_e^2}{2} = e\phi \\
& u_i = \left[\frac{2e}{M}(\phi_0 - \phi) \right]^{\frac{1}{2}} \quad , \quad u_e = \left(\frac{2e\phi}{m} \right)^{\frac{1}{2}} \\
\text{Poisson:} \quad & \frac{dE}{dx} = 4\pi(n_i - n_e)e \\
& \int_0^x dE \frac{dE}{dx} = - \int_0^x dx \frac{d\phi}{dx} 4\pi e \left\{ \frac{(nu)_{i0}}{\left[\frac{2e}{M}(\phi_0 - \phi) \right]^{\frac{1}{2}}} - \frac{(nu)_{e1}}{\left(\frac{2e\phi}{m} \right)^{\frac{1}{2}}} \right\} \\
& \frac{E^2}{8\pi} = \sqrt{m/2e} [j_e \sqrt{\phi} + \sqrt{M/m} j_i (\sqrt{\phi_0 - \phi} - \sqrt{\phi_0})]
\end{aligned}$$

If $E = 0$ at $\phi = \phi_0$, $j_e = \sqrt{\frac{M}{m}} j_i$. This is Langmuir's condition for a double sheath. Noting from the last section $j_e = \sqrt{\frac{M}{m}} j_i$ for single sheaths, this analysis is equivalent to treating two separate plasma sheaths in contact.

In this form Langmuir's condition clearly represents a pressure balance between the electric field on the LHS and the particle impulse on the other. Because the momentum gained by the ions and electrons in the potential drop ϕ_0 are proportional to the square root of their mass ratios, the rate at which they can be provided to the double sheath, their current densities, are inversely so. In general, Langmuir's condition is given by the expression [30, Eqn. (49), p. 973]

$$\int_{\phi_1}^{\phi_0} \rho d\phi = 0 \quad (3.9)$$

when the electric field at either end point is negligible.

3.5.2 Block Theory

Block undertook a more complete study of DLs. He derived conditions for ionospheric DLs under the condition of frozen-in magnetic flux. Ignoring collisions and gravity, he derived self-consistency requirements,

$$\begin{aligned}
(mu^2)_{i0} & \geq \gamma T_{i0} + T_{e0} \left(\frac{eE - \mu_{i0} \frac{dB}{dz}}{eE + \mu_{e0} \frac{dB}{dz}} \right)_{z=0} \\
\text{and } (mu^2)_{e1} & \geq \gamma T_{e1} + T_{i1} \left(\frac{eE + \mu_{i1} \frac{dB}{dz}}{eE - \mu_{e1} \frac{dB}{dz}} \right)_{z=1},
\end{aligned}$$

where, here, γ is the ratio of specific heats. (In terms of degrees of freedom d , $\gamma = \frac{2+d}{d}$.) These two conditions are Bohm criteria. We observe that, for

$\frac{dB}{dz} < 0$ and $E > 0$, the criteria can be satisfied for any velocities provided

$$\begin{aligned} & -\frac{e|E| + \mu_{i0}|\frac{dB}{dz}|}{e|E| - \mu_{e0}|\frac{dB}{dz}|} \geq \gamma \frac{T_{i0}}{T_{e0}} \\ \text{and } & -\frac{e|E| + \mu_{e1}|\frac{dB}{dz}|}{e|E| - \mu_{i1}|\frac{dB}{dz}|} \geq \gamma \frac{T_{e1}}{T_{i1}} \end{aligned}$$

However, when $mu_{i,e}^2 < \gamma T_{i,e} + T_{e,i}$, these constraints limit the electric field. Therefore, these stronger criteria hold for strong DLs.

These Bohm criteria provided strict conditions for DL formation—that is, the directed velocities of the ions and electrons on each side of the DL must be relatively great. Since the current density is

$$j = e[(nu)_{i0} + (nu)_{e1}],$$

these criteria led to the common observation that currentless double layers could not exist.

Similarly, Block developed a Langmuir condition identical to that of the double sheath case in the last section, $\frac{j_i}{j_e} = (\frac{m}{M})^{\frac{1}{2}}$. However, Block hinted at another possibility for the existence of double layers,

The Langmuir condition requires a supply of electrons and ions in the right proportion from both sides of the double layer. If that is not possible, the layer will be charged. The resulting external electric field will accelerate it to an equilibrium velocity such that the Langmuir condition is fulfilled in the frame of the layer [6, p. 366].

Since these criteria were derived using the fluid approximation, the possibility that these criteria may be relaxed for appropriate velocity distributions remained to be explored. These were the approaches of Kan and Lee [25] and Perkins and Sun [35], to be discussed below.

3.5.3 Kan and Lee

Kan and Lee considered the same situation as Block except that, instead of including the magnetic field explicitly, they allowed for trapped electrons

between the high field side of the DL and the increasing magnetic field of the earth. For passing electrons the waterbag distribution,

$$f_{e1} = \begin{cases} \text{const} & V_l < v < V_u \\ 0 & \text{otherwise,} \end{cases}$$

was used, where $V_{u,l} = [(v_{e1} \pm v_{the1})^2 + \frac{2e\phi}{m}]^{\frac{1}{2}}$ but $V_l = (\frac{2e\phi}{m})^{\frac{1}{2}}$ for $v_{e1} < v_{the1}$ —similarly for passing ions. Reflected ions and electrons were modeled with Maxwellians. The resulting Bohm criteria are

$$\begin{aligned} mv_{e1}^2 &\geq 2T_{e1} + T_{i1} & N_{et} < N_c \\ \text{but } v_{e1} &> 0 & N_{et} \geq N_c \end{aligned}$$

where $N_c = N_{e1} [\frac{2e\phi_0}{m(v_{e1} + v_{the1})^2}]^{\frac{1}{2}}$. Similarly $MV_{i0}^2 \geq 2T_{i0} + T_{e0}(1 + \frac{N_{et}}{N_{e0}})$. (Here, $\gamma = 2$ for 2 degrees of freedom.)

This result shows that trapped electrons can provide the necessary number density for electrons on the high field side. However, we note that, while this approach indeed relaxes the requirement on v_{e1} , N_c is a significant fraction of N_e (since $2e\phi \gg mv_e^2$ by assumption), and this approach may require an incident ion velocity significantly greater than the sound speed. So while it may be diminished, there still must be a current.

3.6 Currentless Double Layers

3.6.1 Perkins and Sun

By allowing for trapped ions, Perkins and Sun showed that DL solutions exist which require no current. In their fully kinetic treatment they chose Maxwellian distributions for electrons and high field ions and counter-streaming beams of trapped ions on the low field side. The electron density is $n_e = n_0 e^{-\psi}$ where $\psi \equiv \frac{-e\phi}{T}$. For equal ion and electron temperatures, $\tau \equiv \frac{T_e}{T_i} = 1$, the ion velocity distribution is

$$f = \begin{cases} n_0 (\frac{M}{2\pi T})^{\frac{1}{2}} e^{-\epsilon} & \epsilon > -\Delta \\ 0 & \epsilon < -\Delta \end{cases}$$

This distribution requires the low-field particle kinetic energy, $\frac{mv^2}{2T} = \epsilon + \psi$, to be greater than some minimum ($\psi_0 - \Delta$). Δ , then, determines how

deeply ions are trapped in the potential well, ψ_0 . The resulting ion density is

$$n_0 g(\psi, \Delta) \equiv n_i = \int_{-\psi}^{\infty} \left(\frac{2\pi T}{M}\right)^{\frac{1}{2}} f(\epsilon + \psi)^{-\frac{1}{2}} d\epsilon$$

[35, Eqn. (6)] and the scaled Poisson's equation (3.7) becomes

$$\frac{\partial^2 \psi}{\partial X^2} = g(\psi, \Delta) - e^{-\psi} \equiv G(\psi, \Delta)$$

Integrating by parts,

$$V(\psi, \Delta) \equiv \left(\frac{\partial \psi}{\partial X}\right)^2 = 2 \int_0^{\psi} G(\psi', \Delta) d\psi' \geq 0$$

At ψ_0 , $G(\psi_0, \Delta) = 0$ [35, Eqn. 8(a)] for quasineutrality (eqn. 3.6), while $V(\psi_0, \Delta) = 0$ [35, Eqn. 7] satisfies Langmuir's condition (eqn. 3.9). Eigenvalue DL solutions to these equations exist for particular ψ_0, Δ . A numerical solution is plotted in Fig. 3.6, as for Langmuir's sheath of Figure 3.4, the multivalued nature of $\phi(n_e = n_i)$ is to be noted. This solution also satisfies Bohm's criteria which restrict the slope of the electron distribution function on the low density side but are obviated by Δ on the high field side.

In this presentation Perkins and Sun make several important observations. First, a DL may exist in a region where quasineutrality imposes a multi-valued ϕ . Second, "only" the magnitude not the directions, of the particle parallel velocities are important. And third, the particle distributions which support the DL may be unstable. These observations have important inference for mirrors and magnetospheric potential theories.

Their approach holds for Δ a slowly varying ($L \gg \lambda_D$) function of x , for example in a mirror magnetic field, and is a generalization to analysis of axial potential profiles in thermal barrier cells [15]. Using Maxwellian distributions for electrons (and passing ions), Cohen et al accounted for trapped particles from energetic neutral pumping by charge exchange with a model distribution described by a parameter, "a".

$$f_i = n_0 \left(\frac{M}{2\pi T}\right)^{\frac{3}{2}} \exp\left[\frac{\mathcal{E} - a\mu}{(a-1)T}\right]$$

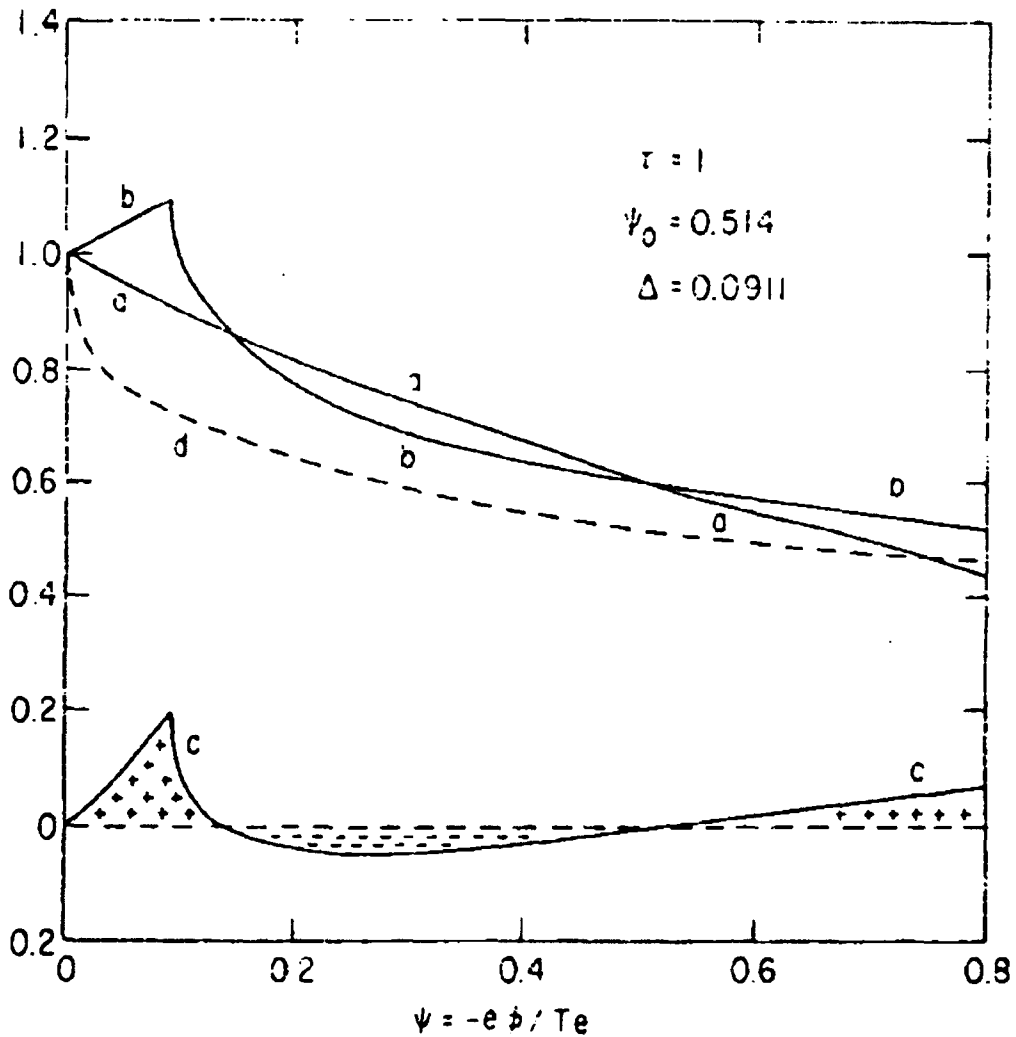


Figure 3.6: Electron and ion densities as a function of potential for $\tau = 1$. Curve a is the electron density $\exp -\psi$. Curve b is the ion density $g(\psi, \Delta)$ [Eq. (6)]. Curve c is the difference $G(\psi, \Delta)$ and depicts regions of positive and negative charge density. Dashed curve d would be the ion density if $\Delta = 0$. It is evident that the required region of positive charge density cannot exist for $\Delta = 0$ [35, Fig. 2, p. 116.]

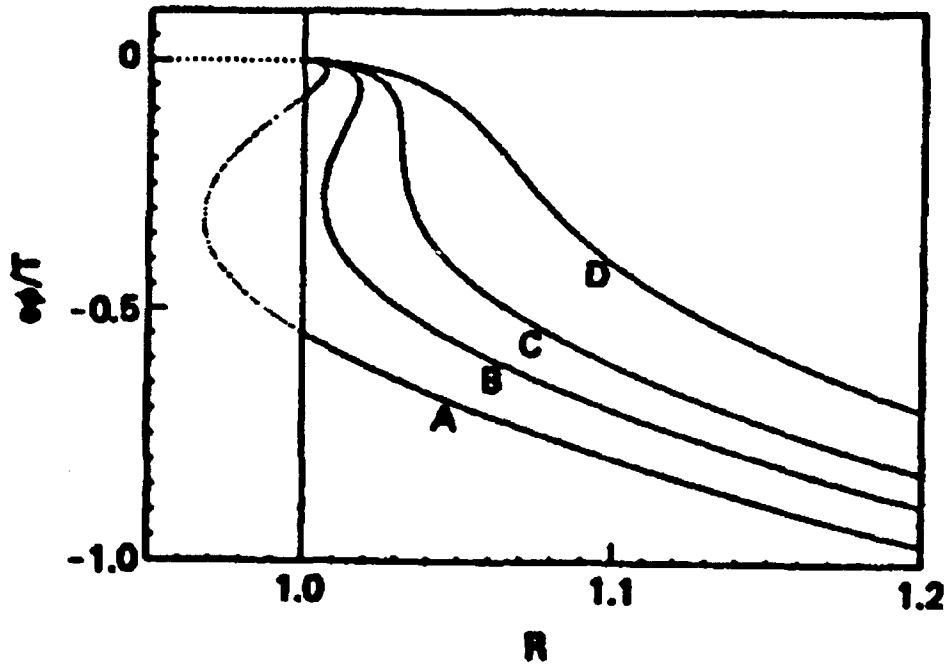


Figure 3.7: Potential profiles $\phi(R)$ obtained from quasi-neutrality for various values of the trapped -particle filling parameter a . The portions of the curves with $R < 1$, shown dotted, apply when $B > B_{throat}$ as in the dashed profile of Fig. 1. The values of a and the corresponding ratios $\rho \equiv n_i/n_e$ and $\Phi_m = -e\phi/T$ evaluated at $R=3$ are: (A) $a=1.08$, $\rho=0.085$, $\Phi_m=2.23$; (B) $a=1.12$, $\rho=0.123$, $\Phi_m=2.19$; (C) $a=1.15$, $\rho=0.15$, $\Phi_m=2.15$; (D) $a=1.20$, $\rho=0.19$, $\Phi_m=2.08$ [15, Fig. 5, p.212].

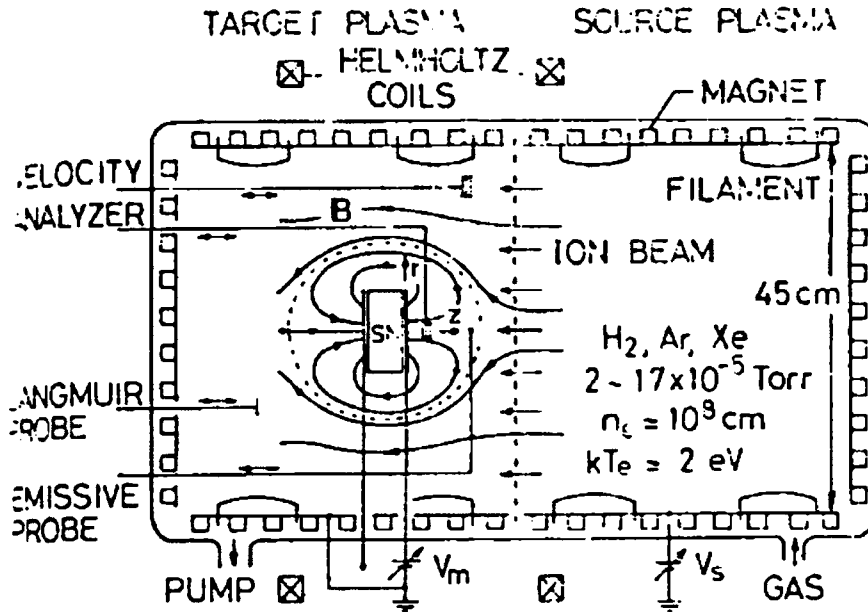


Figure 3.8: Schematic view of the experimental setup. A plane ion beam of energy eV_b is injected into the target plasma against a biased magnet ($V_m > V_b > kT_e/e$). A uniform axial magnetic field is applied opposing the magnetic dipole[44, p.709].

For $a=0$ this is a Maxwellian while for $a=1$ we have a beam of ions. Plots of quasineutral solutions, $\Delta n(\Phi_m, R) = 0$, are at Fig. 3.7. A double layer solution for appropriate values of the electric field at its boundary is possible where Langmuir's condition is satisfied.

3.6.2 Experiments

Stenzel, Ooyama and Nakamura [44] performed a series of experiments in which an ion beam from a double plasma device was injected toward a dipole magnetic field. As pictured in the accompanying sketch (Fig. 3.8), the beam was injected with kinetic energy (V_b) by biasing one half (the high potential side) of a double plasma device with respect to the other. A permanent dipole magnet ($B \sim 500\text{G}$) was situated in the opposite half

of the device and a smaller axial magnetic field ($B \sim 20\text{G}$) was applied counter to that of the dipole so that the configuration consisted of open and closed field lines (as for the earth's magnetosphere.) With magnetic potential $V_m > V_b > e\phi/kT$ a strong double layer was formed with $e\phi \approx .8V_b$, $L = \phi/E \sim 10\lambda_D$ and $\delta n/n \sim 10\%$.

In this experiment trapped particles were observed and formed a large percentage of the total electron population ($n_t/n_f \sim .48$) [44, p.715]. The role of the magnetic potential V_m was both to totally reflect the ions and to impart a drift $v_e > v_{the}$ to the electrons trapped between the double layer and the magnet. Of course, these electrons then were susceptible to the electron two-stream (Buneman) instability. However, oscillations were not recorded near the plasma frequency, indicating a lack of the ion-acoustic instability. The authors attributed this to wave-turbulence and an effective $T_i \geq T_e$ [44, p.717].

The experiment was performed with a variety of plasmas, the higher mass ions being less magnetized. (The electrons are always magnetized.) Double layers were observed in all cases, but the shape of the DL, when the ions were magnetized, assumed the so-called inverted V. Without beams weak DLs were observed.

The double layer was stable. The authors attributed the stability to a momentum balance between the electrons accelerated in the double layer, the reflected ions, and (possibly) ExB drifts in the V-shaped structure. This momentum balance is equivalent to Langmuir's condition. Charge neutrality also plays a role in that on either side of the double layer it must hold [44, p.717].

3.7 Overview

In addition to learning useful methods for obtaining the local self-consistent solutions for potential/particle systems, this chapter introduced several alternative viewpoints. On the one hand, Block's (and Langmuir's) work demonstrated the need for satisfying criteria on the incident particle velocity (Bohm's) and current density (Langmuir's) for existence of double layers. On the other, theory by Perkins and Sun, Cohen, and experiments argue for relaxation or removal of these criteria. In our review we pointed out where these criteria were embedded in each of the theories and exper-

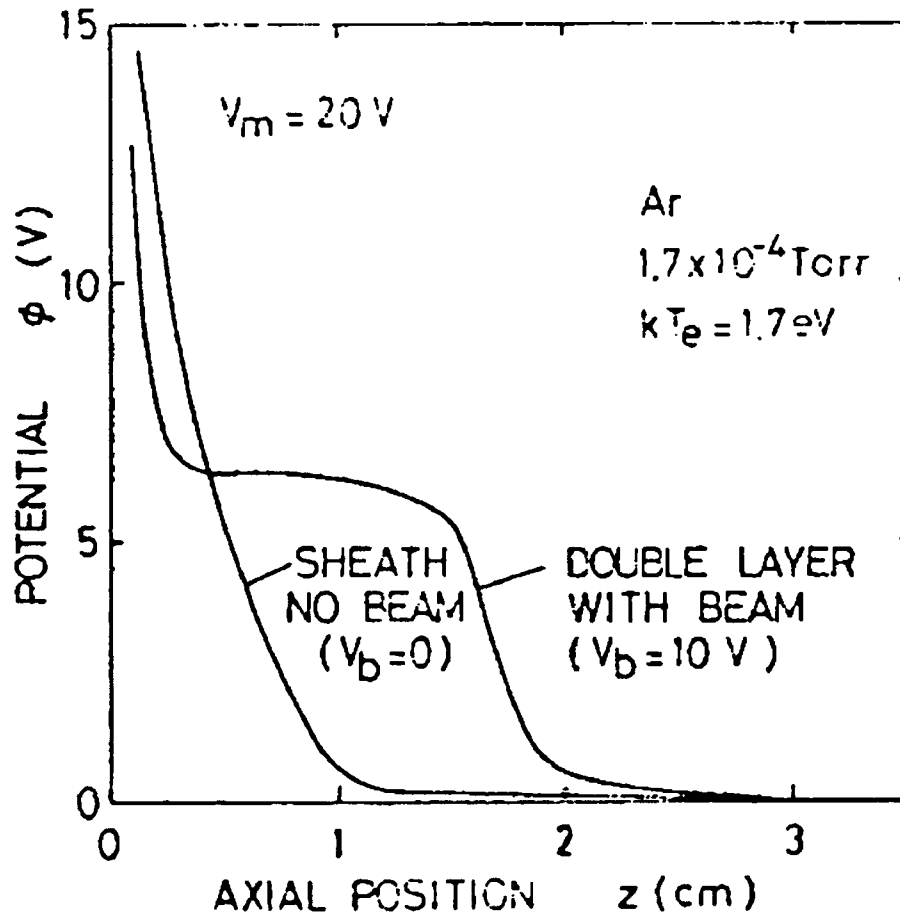


Figure 3.9: Axial plasma potential profiles $\phi(z)$ in front of magnet with bias V_m . Without ion beam a sheath is formed, with reflected ion beam a double layer appears in front of sheath. Small magnet[44, p.712].

imental conclusions, and we suggest that these differing points of view are really entirely consistent. In the next and following chapter we shall further discuss the necessity, or lack thereof for these criteria and the ultimate harmony between competing points of view.

Chapter 4

Analysis

In this chapter, we extend Serizawa and Sato theory [42] by obtaining local solutions to the coupled Vlasov-Poisson equations and explore the possibility for double layer solutions by applying the graphical and analytic techniques we learned in the previous chapter. We remind the reader that their model is that of a comoving neutral two-species plasma injected along the axis toward a dipole magnetic mirror. However, in the next chapter we wish to use particle simulations to observe dynamic behaviour. To best accomodate simulation limitations, we seek a simple model which captures essential physical aspects we wish to examine while permitting access to analytic and computational solution. We devote this chapter to analysing alternative models and comparing their implications.

4.1 Cold Model

This simple model is an asymptotic limit to the more complex models we discuss. For relatively small parallel temperatures, distributions introduced in Section 3.6 [35], [15] are approximated by beams, in which each of the particles have nearly the same parallel velocity.

At points other than injection we expect the plasma to reach equilibrium according to the Vlasov equation (3.1). It is well known that a function of the constants of motion must be a steady-state solution. In our case, for low collision frequencies and “perpendicular” frequencies much less than the ion cyclotron frequency, we take the particle energy, $\mathcal{E} = \frac{1}{2}mv_{\parallel}^2 + \mu B + q\phi$,

and the magnetic moment, $\mu = \frac{mv_{\perp}^2}{2B}$, as constants of motion and model the equilibrium velocity distributions accordingly.

For a cold plasma with no spread in perpendicular or parallel velocities an appropriate distribution for each specie is

$$f \propto \delta(\mathcal{E} - \mathcal{E}_0)\delta(\mu - \mu_0)$$

or, rewriting the functional dependence on energy in terms of parallel velocities [24, p.30],

$$f \equiv A\delta(v - u)\delta(\mu - \mu_0)/v$$

where $v \equiv v_{\parallel}$, $u \equiv [\frac{2}{m}(\mathcal{E} - \mu B - q\phi)]^{\frac{1}{2}} = [\frac{2}{m}(\frac{1}{2}mv_0^2 - \mu\Delta B - q\Delta\phi)]^{\frac{1}{2}}$, and "0" specifies the injection site.

From this distribution we calculate a density,

$$\begin{aligned} n &= 2\pi \int_0^{\infty} dv \int_0^{\infty} dv_{\perp} v_{\perp} f \\ &= \frac{2\pi A}{m} \int_0^{\infty} dv \int_0^{\infty} d\mu B \delta(v - u)\delta(\mu - \mu_0)/v \\ &= \frac{2\pi AB}{mu} \end{aligned}$$

The normalization constant, $A = \frac{mn_0v_0}{2\pi B_0}$, is evaluated by noting that $n = n_0$, $u = v_0$, and $B = B_0$ at injection. Therefore,

$$j \equiv nu = j_0\left(\frac{B}{B_0}\right), \quad (4.1)$$

identical to Schmidt's analysis of a charge-neutral homogeneous plasma moving in a strong magnetic field with weak curvature [40, Eqns. (6-53), p.167].

Using Poisson's equation (3.1(a)), we can evaluate the potential drop as a function of position (in terms of ΔB .) A particular solution results near $\Delta n = n_i - n_e = 0$, where the electric field, E , is a maximum or minimum. Assuming equal injected particle currents, j_0 , and magnetic moments, μ , for each specie, we obtain the electric potential in terms of the magnetic field,

$$\begin{aligned} U^2 &= u^2 \\ \frac{2}{M}\left(\frac{1}{2}Mv_0^2 - \mu\Delta B - e\Delta\phi\right) &= \frac{2}{m}\left(\frac{1}{2}mv_0^2 - \mu\Delta B + e\Delta\phi\right) \\ e\Delta\phi &= \frac{(1 - \frac{m}{M})}{(1 + \frac{m}{M})}\mu\Delta B \end{aligned}$$

where we use capital letters to distinguish ions and lower case for electrons. The maximum potential for this model occurs where $U^2 = u^2 = 0$ at

$$\begin{aligned}\mu\Delta B_{MAX} &= \frac{1}{2}Mv_0^2\frac{(1+\frac{m}{M})}{2} \\ q\Delta\phi_{MAX} &= \frac{1}{2}Mv_0^2\frac{(1-\frac{m}{M})}{2}\end{aligned}\quad (4.2)$$

These relationships are implicit in Schmidt's analysis [40, Eqn.(6-56)].

We observe that this solution preserves overall charge neutrality ($\Delta n \approx 0$, Eqn. (3.6)) for any ϕ . Quasineutrality specifies that the total charge contained even in a double layer [45] or a sheath, when the wall is considered, is negligible. In the global sense then, quasineutrality always holds for the plasma [15]. However, also assuming quasineutrality locally leads to an expression for the electric field

$$qE = -\frac{(1-\frac{m}{M})}{(1+\frac{m}{M})}\mu\frac{dB}{dz}$$

as a function of the magnetic field gradient. This relationship has been noted by many authors (e.g., [52] and [34]) and results in a potential depicted in Figure 4.1. Also in this figure is pictured a non-quasineutral potential with larger gradients than B. When the gradient in ϕ is so large that the gradient in B may be ignored, we may have a double layer.

To further explore the extent to which this model preserves local quasineutrality, we develop a correction to the quasineutral solution. Transforming variables to $V = V_1 + \Delta\gamma \equiv \frac{e\Delta\phi}{T}$, $\gamma \equiv \frac{B}{B_0} = (\frac{z_0}{z})^3$ for a dipole field, $T \equiv \mu B_0$, $\mu \equiv \frac{M\mu_e - m\mu_i}{M+m}$, and $K_{s\alpha} \equiv \frac{\frac{1}{2}m_\alpha u_{s\alpha}^2}{T} = \frac{\frac{m_\alpha}{2}[u_\alpha^2 - \frac{2}{m+M}(\mu_i + \mu_e)\Delta B]}{T}$, simplifies Poisson's equation to

$$\begin{aligned}-\nabla_Z^2 V_1 &= \gamma \sum_\alpha \alpha \frac{u_\alpha}{u_{s\alpha}} (1 - \frac{\alpha V_1}{K_{s\alpha}})^{-\frac{1}{2}} + \nabla_Z^2 \Delta\gamma \\ &\approx \gamma (\frac{V_1}{L^2} + \frac{12}{Z^2}) \text{ for "small" } V_1,\end{aligned}\quad (4.3)$$

where $\frac{1}{L^2} = \sum_\alpha \frac{1}{2K_{s\alpha}} \frac{u_\alpha}{u_{s\alpha}} = (1 + \frac{m}{M})\frac{1}{2k} \frac{u}{u_s}$, if $u=U$, and $Z \equiv \frac{z}{\lambda_D}$, z the axial distance from the dipole center. For $\frac{dV_1}{dz}(z_0) = 0$ and $V_1(z_0) = 0$,

$$V_1 = V_0 \left\{ 1 + \left(\frac{Z}{Z_0}\right)^3 \left[\frac{2L}{Z} \sin \frac{(Z-Z_0)}{L} - \cos \frac{(Z-Z_0)}{L} \right] \right\}$$

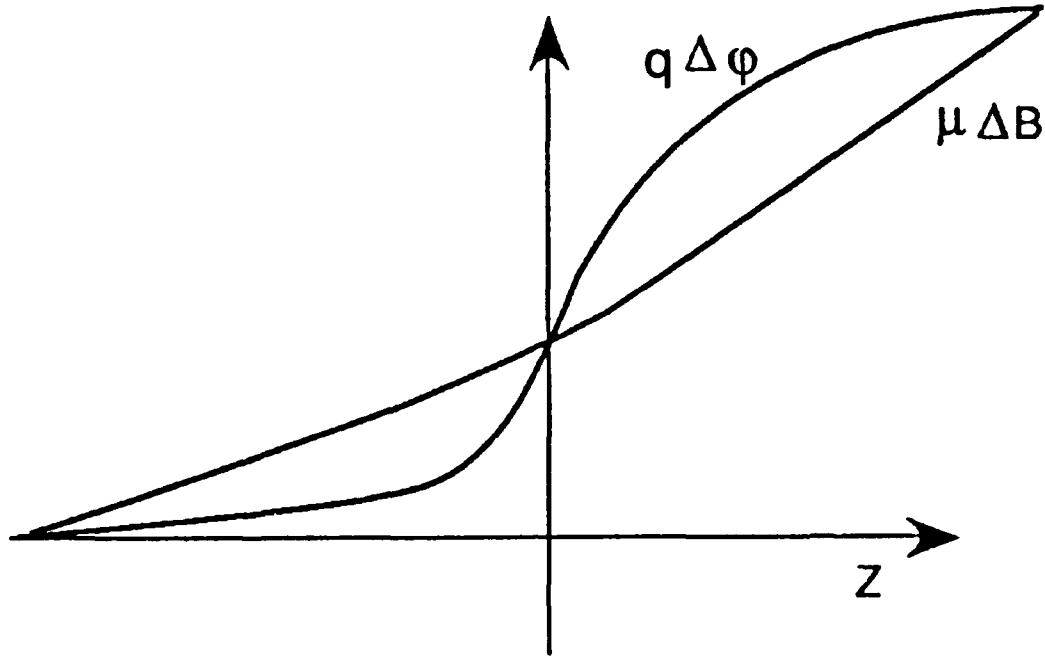


Figure 4.1: The QN solution is $E \propto \frac{dB}{dz} (q\Delta\phi \propto \mu\Delta B)$. In those cases when the gradient of B relative to E may be ignored, a non-quasineutral potential, designated by $q\Delta\phi$, results.

Far from the injection point, $Z_0 \gg Z \gg 1$,

$$V_1 \approx V_0 \equiv -12\left(\frac{L}{Z}\right)^2$$

remains “small”.

The resulting electric field $E \propto \frac{\partial B}{\partial z}$ except near $\frac{V_1}{K_s} \approx 1$ where Equation (4.3) more resembles the ion sheath equation of section 3.4.1. This point occurs near $Z = 1$ where $\mu \frac{\partial B}{\partial z} / T \sim 1$ and μ may no longer be treated as a constant of motion. Although it results in particles' ability to explore a larger spatial extent, a potential doesn't necessarily accelerate particles. The combined “potential” of the electric and magnetic fields slows both electrons and ions in this case.

Using a graphical technique evident even in Langmuir's work, as in Figure 3.4, we obtain the quasineutral solution,

$$\Delta n(V, B) = 0$$

Defining $Y \equiv \frac{\Delta B}{B_0} = \gamma - 1$, in Fig. 4.2 we plot charge density $\Delta n(V, B)$ for all values $V, Y < K$. The graph may be conveniently divided into four sections separated by two diagonals. At the middle left is the full plasma

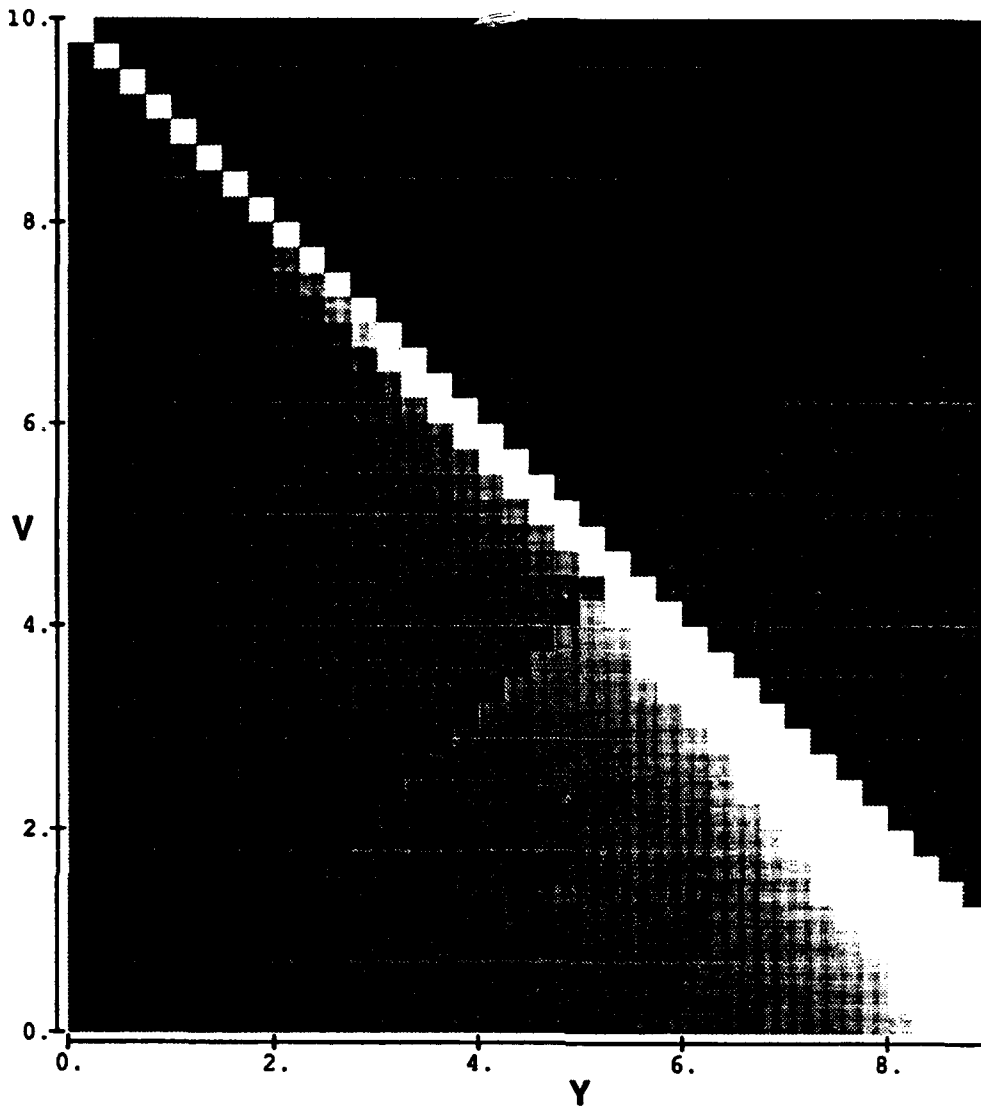


Figure 4.2: This figure is a charge density plot of $\Delta n(V, B)$ in terms of $Y \equiv \frac{\Delta B}{B_0} = \gamma - 1$. The light regions correspond to regions of positive density while the dark regions are negative. Along the diagonal extending from the lower left to the upper right is the quasineutral solution. The white line from the upper left to lower right is an ion-rich (anode) region which occurs as the ions overshoot the electrons. No electrons are allowed in the bottom quadrant. Similarly the upper (cathode) quadrant permits only electrons accelerated by the increasing potential. The actual solution of Poisson's equation is near (slightly below) the QN line until it formally becomes a sheath at the (anode) diagonal.

solution. Along the straight diagonal from the lower left to the upper right lies the quasineutral solution given by equation (3.6). Above this line the solution is increasingly positive as the electrons accelerate and the ions slow in the potential, V . Along the diagonal from the upper left to the lower right, is an anode solution where the ions are so dense that the electron contribution may be ignored. In the quadrant below the two diagonals electrons are precluded, as are the ions above. To the right neither are allowed.

As noted in the previous chapter, a DL solution requires adjacent layers of oppositely charged plasma. Since at fixed magnetic field the densities (4.1) of the two species diverge with increasing potential, these distributions are incompatible with DL solutions. However, as we shall see in the next section, the assumed initial distributions for a particular situation may not agree with the steady state potential which results. For example, in this section conversion of the cold electron velocity distributions to Maxwellian leads instead to the sheath solutions of Section 3.4.1.

4.2 Finite Perpendicular Temperature

4.2.1 Particle Currents

With finite perpendicular temperature we must consider particles that are able to transit the model's extent into the loss cone. We choose a perpendicular Maxwellian injection distribution

$$f = f(\mathcal{E}, \mu) = A\delta(\mathcal{E} - \mathcal{E}_0)\exp -\frac{\mu B_0}{T}$$

while leaving the parallel distribution cold to obtain

$$\begin{aligned} j &= 2\pi A \int_0^\infty dv v \int_0^\infty \frac{dv_1^2}{2} \delta(\mathcal{E} - \mathcal{E}_0) \exp -\frac{\mu B_0}{T} \\ &= \frac{2\pi AT}{m^2} \frac{B}{B_0} \int_0^{K_0 - V} dK \exp \frac{K_0 - V - K}{Y} \\ &= \frac{2\pi AT}{m^2} \frac{B}{B_0} [1 - \exp \frac{K_0 - V}{Y}], \end{aligned}$$

where we have used $K \equiv \frac{1}{2}mv^2$, $V \equiv \frac{e\Delta\phi}{T}$, and $Y \equiv \frac{\Delta B}{B_0} (= \frac{\leq\mu>B}{T})$.

At $j = j_0$, $\Delta B = 0$, $B = B_0$, and $\Delta\phi = 0$, giving $A = \frac{j_0 m^2}{2\pi T}$ and

$$j_{forward} = j_0 \left(\frac{B}{B_0} \right) \left[1 - \exp\left(-\frac{K_0 - V}{Y}\right) \right],$$

essentially the result produced in the previous chapter, Eqn. 4.1, modified by a correction term. In the reverse direction we must allow a loss cone for those particles with $0 < Y_{MAX} < K_0 - V_{MAX}$ so that

$$j_{reflected} = j_0 \left(\frac{B}{B_0} \right) \left[\exp\left(\frac{-K_0 - V_{MAX}}{Y_{MAX}}\right) - \exp\left(\frac{-K_0 - V}{Y}\right) \right]$$

for $K_0 > V_{MAX}$. For $K_0 < V_{MAX}$, $j \equiv j_{forward} - j_{reflected} = 0$.

$$j = j_0 \left(\frac{B}{B_0} \right) \left[1 - \exp\left(-\frac{K_0 - V_{MAX}}{Y_{MAX}}\right) \right] H(K_0 - V_{MAX}) \quad (4.4)$$

Requiring the steady state charge of the system to remain constant, implies $\Delta j \equiv j_i - j_e = 0$ at $z=0$ for equal injection currents at $z=z_0$. Assuming equal injection velocities,

$$\begin{aligned} k_0 + \frac{e\Delta\phi_{MAX}}{T_e} &= K_0 - \frac{e\Delta\phi_{MAX}}{T_i} \\ e\Delta\phi_{MAX} &= \frac{1}{2} M v_0^2 \left(1 - \frac{m T_i}{M T_e} \right) / \left(1 + \frac{T_i}{T_e} \right) \end{aligned}$$

This is the maximum potential for this model and agrees with the cold result (4.2) for equal ion and electron temperatures. Although corrections for non-monotonic ϕ may be necessary, they were not applied in the above calculation. Similarly, in the section that follows we ignore corrections due to the loss cone. However, as we shall see in the next chapter, any particular physical realization requires adjudication between these, possibly conflicting, demands on the potential.

4.2.2 Particle Densities

To obtain the local solution for this model, we begin by evaluating the particle density.

$$n = 2\pi \int_0^\infty dv \int_0^\infty dv_\perp v_\perp A \delta(\mathcal{E} - \mathcal{E}_0) \exp^{-\frac{\mu B_0}{T}}$$

$$\begin{aligned}
&= \frac{2\pi A}{m} \int_0^\infty dv \int_0^\infty d\mu B \delta\left(\frac{1}{2}mv^2 - \frac{1}{2}mv_0^2 + \mu\Delta B + q\Delta\phi\right) \exp^{-\frac{\mu B_0}{T}} \\
&= \frac{2\pi A}{m} \frac{B}{\Delta B} \int_0^\infty dv \exp^{-\frac{B_0}{\Delta B}\left(\frac{1}{2}mv_0^2 - \frac{1}{2}mv^2 - q\Delta\phi\right)} H\left(\frac{1}{2}mv_0^2 - \frac{1}{2}mv^2 - q\Delta\phi\right) \\
&= 2n_0 X_0 \frac{B}{B_0} F\left(\frac{K_0 - V}{Y}\right)^{\frac{1}{2}} \tag{4.5}
\end{aligned}$$

where we have substituted for A from above, H is the Heaviside function, and

$$X^2 \equiv \frac{K_0 - V}{Y}$$

with $X_0 \equiv X(V = 0)$. The last term in equation (4.5),

$$F(X) = \exp -X^2 \int_0^X dt \exp t^2,$$

is known as Dawson's Integral [1, p.298] and has the asymptotic values

$$\begin{aligned}
F(x) &= x \exp -x^2 \sum_{n=0}^{\infty} \frac{(-x^2)^n}{(n + \frac{1}{2})n!} \text{ for small } x \text{ [1, 262] and} \\
F(x) &= \left[1 + \sum_{n=1}^{\infty} \frac{(1)(3)(5) \cdots (2n-1)}{(2x^2)^n}\right] \frac{1}{2x} \text{ for large } x \text{ [4, p.256]}
\end{aligned}$$

In Figure 4.3 we have plotted n_i and n_e for particular values of Y. These establish the crossing points plotted in Figure 4.4, the quasineutral solutions for these charge densities. For small (Y,V) the solution is that presented in the previous section and $\Delta\phi \propto \Delta B$. For increasing ΔB an additional solution appears, but, because n_i increases with Y and F reaches a maximum at .54, an upper bound for Y exists at $\frac{1}{2X_0} = \frac{1}{2} \sqrt{\frac{Y}{k}} = .54$ (treating n_i as constant for these values of V) or $y \approx k$ —the point where the perpendicular energy equals the total injected electron energy.

A solution also exists at $e\Delta\phi \approx K_0$ for all values of Y. These solutions are obtained in the (four) limits of large and small x and X bounded by the two diagonals and lying in the four quadrants established in Figure 4.2. (X, the ion value for the argument of Dawson's integral, is a maximum at the lower left corner and decreases toward the upper right. x, its electron counterpart, is a maximum at the upper left corner and decreases toward the lower right.)

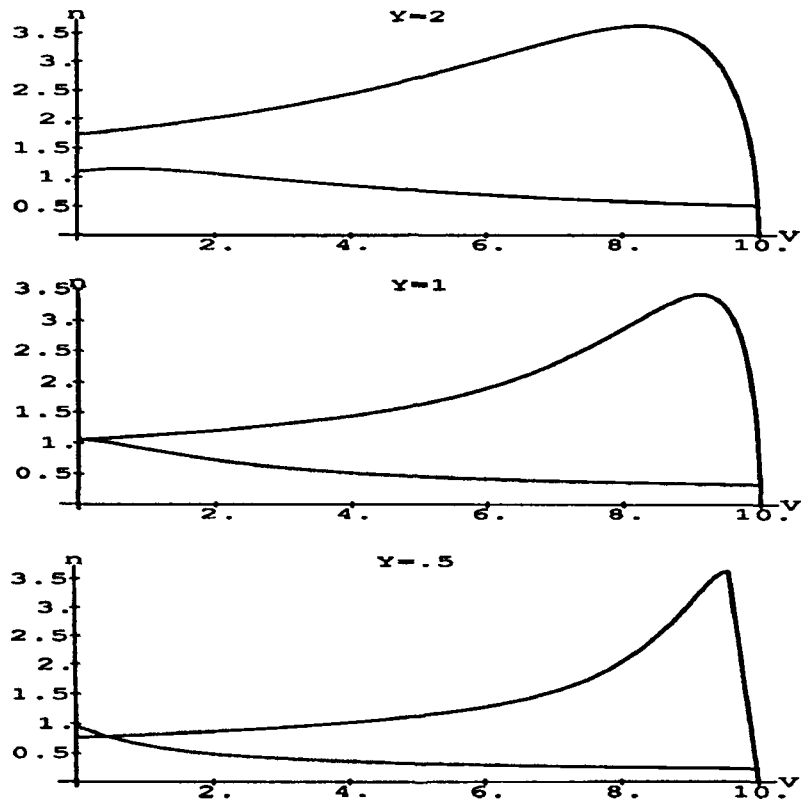


Figure 4.3: Plotted are n_i and n_e vs V for the values $Y=0.5, 1$ and 2 . The ion density is that with the peak to the right and the electron density is the smaller peaked function to the left. The points where the two densities cross represent quasineutral solutions.

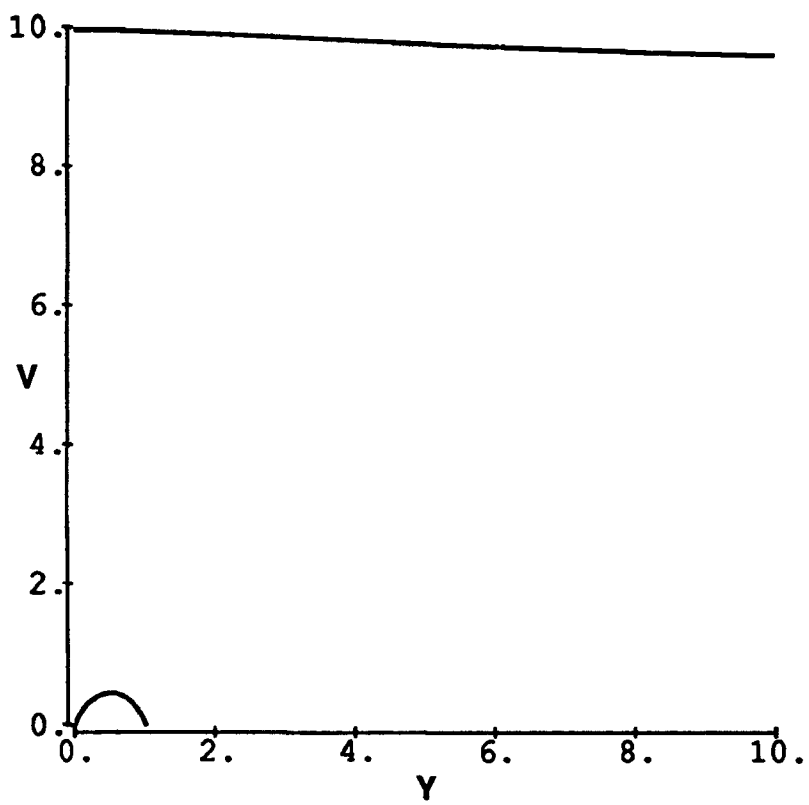


Figure 4.4: Plotted here are the contours $\Delta n = 0$ for both electron and ion densities proportional to $F(X)$.

Between the two quasineutral solutions $n_i > n_e$ and a sheath must exist. To connect these solutions requires passage through a region of strong electric field gradient. As noted by Stenzel and Ooyama [44, p.714], acceleration of electrons in this region may lead to a strong electron two-stream instability and their rapid thermalization. Designating this point as "1", we may replace the Dawsonian electron distribution with a Maxwellian

$$n = n_1 \exp \frac{e\Delta\phi_1 - \mu\Delta B_1}{T_e}$$

where $n_1 \equiv 2n_0 \frac{B}{B_0} X_0 F(\frac{K_0 - V}{Y})|_{z_1}$ and T_e represents a spread induced by thermalization, expected to be on the order of the accelerating potential.

Plotted in Fig. 4.5 is the contour $\Delta n = 0$ for $K = 25, T_e = 15$ and z_1 at $Y=1$. Near z_1 the potential V is double-valued, allowing a DL solution when Langmuir's condition, eqn. (3.9), is also satisfied. We remark that the shapes of these model distributions lead to double layer solutions, as Perkins and Sun [35] postulated and we demonstrate in the next chapter.

4.2.3 Langmuir's Condition

Holding B constant, an exact integral of $F(X)$ over ϕ is

$$\begin{aligned} e \int_0^\phi F(X) d\phi / T &= \int_0^V dV \exp -X^2 \int_0^X dt \exp t^2 \\ &= \int_0^V dV \exp -\frac{K_0 - V}{Y} \int_0^X dt \exp t^2 \\ &= Y[F(X)|_0^V - \int_0^V dV \frac{\partial X}{\partial V}] \\ &= Y[F(X) - X]|_0^V, \end{aligned}$$

This result is useful for establishing Langmuir's condition:

$$\begin{aligned} q \int (n_i - n_e) d\phi &= T_i \{ 2n_0 \frac{B}{B_0} X_0 [F(X) - X]|_0^V \} - T_e (n - n_0) \\ T_i (n - n_0) - T_e (n - n_0) - (X - X_0) (2n_0 X_0 \frac{B}{B_0}) &= 0 \\ \Delta T \Delta n - \Delta X (2n_0 X_0 \frac{B}{B_0}) &= 0 \end{aligned}$$

Together with quasineutrality, this condition yields a double layer solution, visually evident in Figure 4.5 when the integrated particle densities

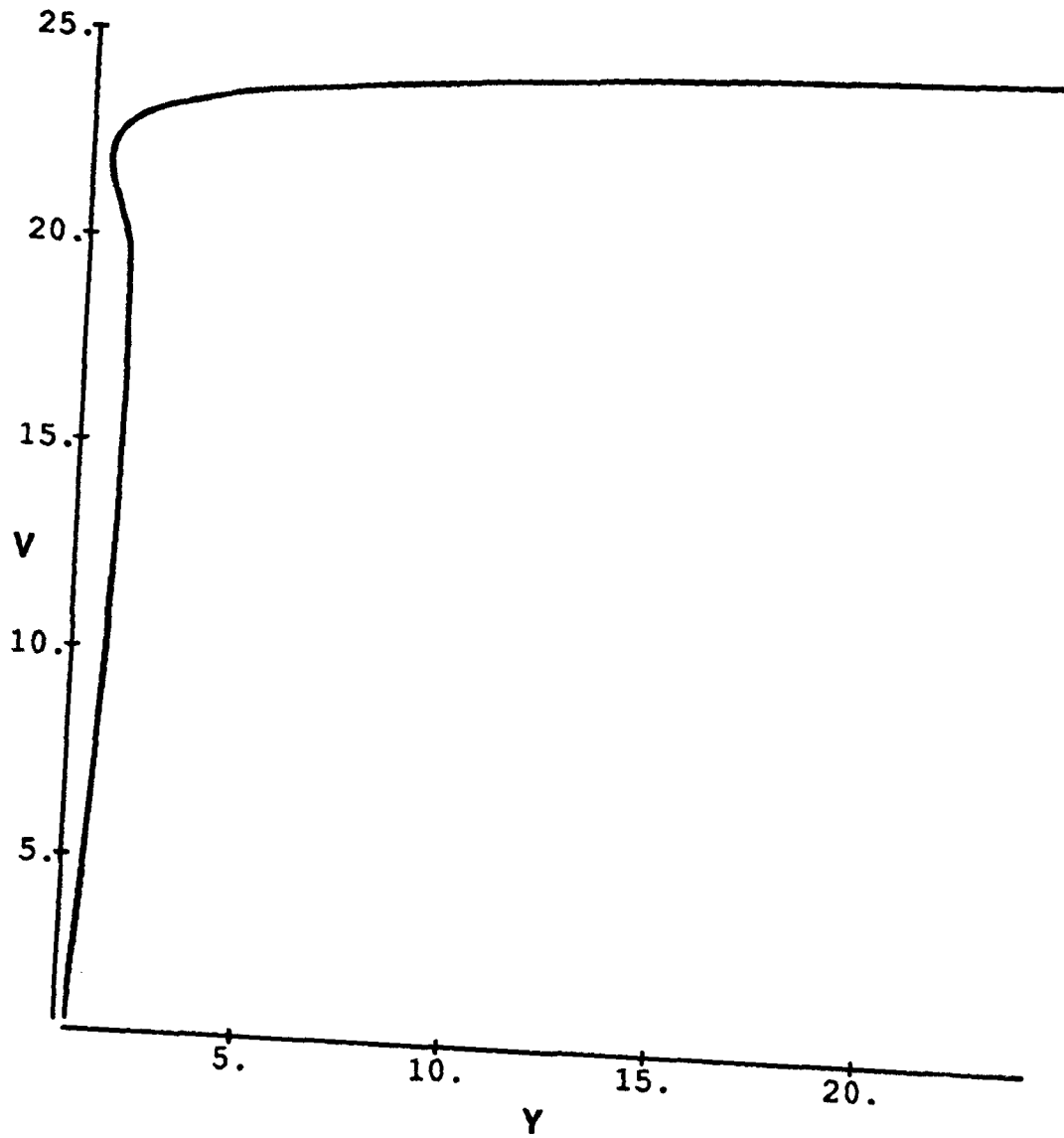


Figure 4.5: In this figure we have plotted the contour $\Delta n = 0$ for Maxwellian Electrons and Dawsonian Ions. The solution is obviously double-valued in V , and a DL solution exists where Langmuir's condition is satisfied.

over the potential enclosed by two areas on either side of a line drawn perpendicular to the Y axis and the quasineutral solution are equal. Since by assumption $\Delta X < 0$ and $\Delta n > 0$, $T_e > T_i \equiv \langle \mu_i \rangle > \Delta B$ is required to satisfy Langmuir's condition, consistent with streaming instabilities[47]. While this distribution will prove valuable in our particle simulations, instabilities will permit observation of the more general model we discuss below.

4.3 Generalization to Drifting Maxwellian

4.3.1 Current Density

We generalize our results to a drifting Maxwellian by integrating over the distribution

$$h(u) = A \exp -\frac{m(v_0 - u)^2}{2kT_{\parallel}}$$

with the boundary condition

$$j_0 = n_0 \int_0^{\infty} h(u)u du \equiv n_0 \langle u \rangle$$

for both species. Using Eqn. (4.4), we evaluate the particle current density as

$$\begin{aligned} j &= n_0 \left(\frac{B}{B_0}\right) \int_{u_{\min}}^{\infty} du u h(u) \left[1 - \exp -\frac{K - V}{Y}\right] \\ &= n_0 \left(\frac{B}{B_0}\right) \left[\langle u \rangle - \int_0^{\infty} du u h(u) \exp -\frac{K - V}{Y} - \int_0^{u_{\min}} du u h(u) \left(1 - \exp -\frac{K - V}{Y}\right)\right] \\ &\equiv j_0 \left[1 - \frac{\Delta j}{j_0} - \frac{j_1}{j_0}\right] \end{aligned}$$

where

$$u_{\min} = \begin{cases} (2e\phi/m)^{\frac{1}{2}} & \text{for ions} \\ 0 & \text{for electrons} \end{cases}$$

and we redefine $T \equiv T_{\parallel}$ and $\mu \equiv \langle \mu \rangle$. K , V and Y have their former values multiplied by the quantity $\frac{T_{\perp}}{T_{\parallel}} \equiv \frac{\mu B_0}{T}$. For example, $V = \left(\frac{q\phi}{T_{\perp}}\right) \left(\frac{\mu B_0}{T}\right) \equiv K_{\min}$. We recognize j_0 as the cold particle current density, Eqn. 4.1.

For $K_0 - V \gg 1$, $\langle u \rangle \approx \frac{2AT}{m} \sqrt{K_0} \int_0^\infty d\Delta x \exp -\Delta x^2$, and we may approximate Δj

$$\begin{aligned} \Delta j &\approx \frac{2n_0(\frac{B}{B_0})ATV}{m} [R(\frac{Y}{Y+1})]^2 \exp -\frac{V}{Y} [R^2(\frac{Y}{Y+1}) \mp 1] \int_{-1}^\infty d\Delta x \exp -(\frac{K_0 Y}{1+Y}) \Delta x^2 \\ &\approx j_0 \frac{B}{B_0} (\frac{Y}{1+Y})^{\frac{3}{2}} \exp -\frac{V}{Y} [R^2(\frac{Y}{Y+1}) \mp 1] \end{aligned}$$

where $R \equiv \sqrt{\frac{K_0}{V}} = \frac{v_0}{u_{\min}}$. Similarly,

$$\begin{aligned} j_1 &\approx An_0 (\frac{B}{B_0}) u_{\min}^2 [\frac{\exp -V(1-R)^2}{2V(R-1)} - \frac{\exp -V(1-R)^2}{2V(R-\frac{Y+1}{Y})}] \\ &\approx -\frac{j_0 \frac{B}{B_0}}{2\sqrt{\pi K_0}} [\frac{1/Y}{(R-\frac{Y+1}{Y})(R-1)}] \exp -V(1-R)^2 \end{aligned}$$

The ratio of the last two terms is $|\frac{j_1}{\Delta j}| = \frac{K \exp -V(1-R)^2}{Y 2\sqrt{\pi K}^{\frac{1}{2}} (R-1)^2}$ for large Y .

Requiring $\ln x = 0$ for charge conservation, we set

$$x = \frac{\Delta j_i}{\Delta j_e} = \frac{\Delta j}{\Delta j_e} + \frac{j_1}{\Delta j_e} = x_0 + x_1$$

Since $\ln x(V_0 + V_1) \approx \ln x_0(V_0) + \frac{1}{x_0(V_0)} [x_1(V_0) + \Sigma_\alpha \frac{\partial x_0}{\partial V_\alpha} |_{V_0} V_{1\alpha}] = 0$, to lowest order $\ln x_0(V_0) = 0$ and

$$\begin{aligned} \frac{V}{Y} + \frac{v}{y} &= \frac{K}{1+Y} - \frac{k}{1+y} - \frac{3}{2} \ln [\frac{y}{Y} (\frac{1+Y}{1+y})] \\ V &= K \frac{(\frac{1}{T_i + \mu_i \Delta B} - \frac{M}{T_e + \mu_e \Delta B}) - \frac{3}{2} \ln [(\frac{T_i + \mu_i \Delta B}{T_e + \mu_e \Delta B}) (\frac{\mu_e}{\mu_i})]}{\frac{1}{\mu_i \Delta B} + \frac{1}{\mu_e \Delta B}} \\ &= \frac{\mu_i \Delta B}{(1 + \frac{\mu_i}{\mu_e}) T_i + \mu_i \Delta B} \frac{K}{M} [(1 - \frac{m T_i + \mu_i \Delta B}{M T_e + \mu_e \Delta B}) \\ &\quad - \frac{3}{2} \ln [(\frac{T_i + \mu_i \Delta B}{T_e + \mu_e \Delta B}) (\frac{\mu_e}{\mu_i})] \end{aligned}$$

For $T = \mu B_0$, $T + \mu \Delta B = \mu B$ and

$$V = K \frac{(1 - \frac{m T_i}{M T_e})}{(1 + \frac{\mu_i}{\mu_e})} (\frac{\Delta B}{B_{MAX}}) \quad (4.6)$$

In the limit of large injection energy to parallel temperature ratio, this asymptotic evaluation of the potential has resulted in an analytic expression which agrees exactly with the "semi-empirical" result obtained by Serizawa and Sato [42, Eqn. 7] but provides corrections which account for biMaxwellian temperature distributions.

4.3.2 Particle Density

We compare the density for this distribution to that of the previous sections. Integrating over (4.5)

$$n = 2n_0 \frac{B}{B_0} \int_{\sqrt{V}}^{\infty} F\left(\frac{z^2 - V}{Y}\right)^{\frac{1}{2}} \exp -(z - \sqrt{K_0})^2 dz \left(\frac{z^2}{Y}\right)^{\frac{1}{2}} / \int_0^{\infty} \exp -(z - \sqrt{K_0})^2 dz$$

The integral can be evaluated by a variation on the method of steepest descent[4]. We begin by changing variables to $t = z/\sqrt{V}$, $r = \sqrt{K_0}/\sqrt{V}$. Noting that $F(X)$ may be written

$$F(X) = \exp -X^2 \int_0^X dx \exp x^2 = X \int_0^1 dy \exp -(1 - y^2)X^2,$$

$$n(t, y) = 2n_0 \frac{B}{B_0} \frac{V}{\sqrt{\pi Y}} \int_1^{\infty} dt \int_0^1 dy \left[\frac{V}{Y}(t^2 - 1)\right]^{\frac{1}{2}} t \exp -\left[(1 - y^2)\frac{V}{Y}(t^2 - 1) + V(t - r)^2\right]$$

Setting $\phi(t, y) = (1 - y^2)(t^2 - 1) + Y(t - r)^2$, we note

$\nabla\phi_{t,y} = 0$ at $\{t_0, y_0\} = \{1, [1 + Y(1 - r)]^{\frac{1}{2}}\}$ and $\{t_0, y_0\} = \{\frac{rY}{1+Y}, 0\}$, where

$$\Delta\phi \equiv \left(\Delta t \frac{\partial}{\partial t} + \Delta y \frac{\partial}{\partial y}\right)^2 \phi|_{t_0, y_0} = \begin{cases} Y\Delta t^2 - 4y_0\Delta y\Delta t \\ (1 + Y)\Delta t^2 - (t_0^2 - 1)\Delta y^2 \end{cases}$$

These two points correspond to the combined contribution from the two peaks in F and the Maxwellian.

$$\begin{aligned} \text{For } t_0 < 1 \quad n &= 2n_0 \frac{B}{B_0} \frac{V}{\sqrt{\pi Y}} \exp -V(1 - r^2) \\ &\times \int_0^{\infty} d\Delta t \int_{-y_0}^{1-y_0} d\Delta y \left[\frac{V}{Y}\Delta t(2 + \Delta t)\right]^{\frac{1}{2}} (1 + \Delta t) \exp -V[r\Delta t^2 - 4\frac{y_0}{Y}\Delta y\Delta t] \end{aligned}$$

Letting $\Delta y = m\Delta t$, we integrate along a path of steepest descent in the $\Delta y, \Delta t$ plane for $m = -\frac{4y_0}{rY}$ yielding

$$\begin{aligned} n &\approx -\frac{2n_0 \frac{B}{B_0} \frac{V}{\sqrt{\pi Y}}}{(1+m^2)} \exp -V(1-r)^2 \int_{-(1-y_0)}^{\infty} dP \exp -rV \frac{m^2}{(1+m^2)} P^2 I[x(P)] \Big|_{x_{\min}}^{x_{\max}} \\ &\approx -\frac{2n_0 \frac{B}{B_0} X_0}{r(1+m^2)} \exp -V(1-r)^2 \left[\frac{\sqrt{1+m^2}}{\sqrt{r}m} I(-m(1-y_0)) + \frac{1+m^2}{2\sqrt{\pi V} m^2 r} I(-m) \right] \end{aligned}$$

with $I(x) = \frac{1}{3}[(1+x)^2 - 1]^{\frac{3}{2}}$, $x_{\max} = -m[(1-y_0) + P]$, and

$$x_{\min} = \begin{cases} 0 - (1-y_0) < P < y_0 \\ -m(-y_0 + P)y_0 < P < \infty \end{cases}$$

so that n decays exponentially from $r=1$.

Similarly for $t_0 > 1$,

$$n \approx 2n_0 \frac{B}{B_0} \sqrt{\frac{K}{Y}} \left(\frac{Y}{1+Y} \right)^{\frac{3}{2}} \exp -V(t_0 - r)^2 F\left[\frac{V}{Y}(t_0^2 - 1) \right]^{\frac{1}{2}},$$

which corresponds to the original distribution shifted in Y and diminished by an exponential factor. Finally, for $t_0 \approx 1$ and $y_0 \approx 0$ the contribution from the two peaks coalesce giving

$$n \approx 2n_0 \frac{B}{B_0} \frac{V}{\sqrt{\pi Y}} \sum_{n=0}^{\infty} \frac{\sqrt{2}}{n!} \left(\frac{1}{2} \right)^n \left[\frac{\Gamma(\frac{n+\frac{3}{2}}{2})}{[\frac{V}{Y}(1+Y)]^{\frac{n+\frac{3}{2}}{2}}} \frac{\Gamma(\frac{n+\frac{5}{2}}{2})}{[\frac{V}{Y}(1+Y)]^{\frac{n+\frac{5}{2}}{2}}} \right] \exp -V(1-r)^2$$

A slowly converging function yielding a broad peak.

These three equations correspond with the original quadrants in Figure 4.2. The last essentially divides the plane along the quasineutral line, above and below are regions of small and large t_0 respectively, apparent as the high V and low V areas in Figure 4.6, where we have plotted the densities for $Y=1$ and 4. We see that, as expected, the peak is spread. Although the inflection point is lowered, it permits the ion density to cross a constantly increasing n_e at three points in V . The shift in the peak lowers the range of n values, but not necessarily the magnitude of double layer potentials. Just as in the previous section, opportunity for a DL solution diminishes with increasing B . We shall observe the consequences of this analysis in the next chapter.

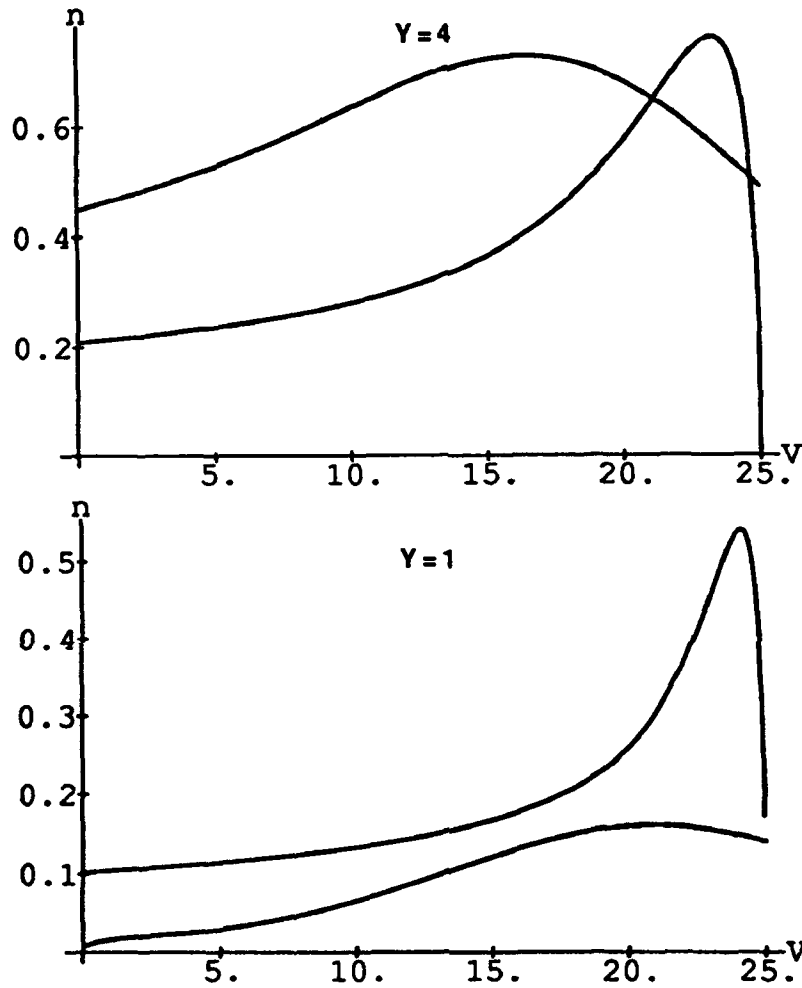


Figure 4.6: In this figure are plotted ion distribution functions where injected velocities are drawn from a Drifting Maxwellian. Comparison to the F distribution of the previous section shows that the peak in this distribution is less pronounced. Similarly the inflection point has shifted to the left (toward injection). However, presence of the inflection point together with a sufficiently large electron temperatures should allow DL solutions in the cases we consider.

4.4 Summary

The analysis of the potentials we developed in these sections contrasts between the global requirement which maintains overall charge neutrality and the local one which permits double layer solutions. The latter potential is dependent on the self consistent constituent particle distributions both in slope (in terms of Bohm criteria) and in integrated charge density over the potential (in terms of Langmuir's condition.)

The results of this section showed that, in limited circumstances of the cold one-dimensional plasma in presence of a magnetic field, the only potential solution is one in which the plasma must either reach quasineutrality or leave a region unexplored. First order corrections show explicitly that large scale potential drops do not result in double layers or even particle acceleration. Thus, the global and the local requirements are equivalent.

With the added freedom to redistribute energy between parallel and perpendicular velocities the plasma may explore beyond boundaries for the cold plasma. Indeed, the plasma has access to an infinitude of quasineutral solutions. The alternative it chooses is that required for pressure balance as demanded by Langmuir's condition. However, the conditions for double layers are stringent, and for large mass ratios a double layer solution is difficult to attain with Dawsonian electrons.

When instabilities alter particle distributions, as we allowed in the case of cold parallel electrons, they may present opportunities for double layer solutions. Changing the electron distribution in Section 4.2 to that of a Maxwellian immediately leads to double layer solutions pictured in Figure 4.5. These distributions and results agree with those first proposed by Perkins and Sun [35]. Addition of parallel temperatures softens distribution shapes, but still permits double layer solutions to exist. Indeed, apparent from graphical methods, local perturbations may even provide opportunity for multiple closely spaced double layers.

In each case we demonstrated Langmuir's condition in the role of pressure balance and couched Bohm's criteria as a requirement on the slope of the distributions functions. This view provides different emphasis from but demonstrates the consistency between frameworks established by other authors.

Our global analysis confirms Serizawa and Sato [42]. We demonstrate that their solution varies little between cold (Eqn. 4.2) and warm (Eqn.

4.6) particles except for a multiplicative factor of order unity, attesting to a weak dependence on the mirror ratio T_{\parallel} brings. Additionally, the physical distribution of Serizawa and Sato in section 4.3 should permit double layer solutions. As demonstrated, the model distribution of section 4.2 well approximates both the global and local results expected with their distributions. However, to observe the time-dependent behaviour of these scenarios, we resort to particle simulation as presented in the next chapter.

Actual solutions depend greatly on not their initial values but on the time-dependent behaviour of the resulting self-consistent particle distributions actually explored. To investigate these, it is necessary to resort to particle simulation techniques. In Chapter 5 we investigate a simulation equivalent to the cold T_{\parallel} , warm T_{\perp} distribution of section 4.2. As pointed out above, the adequacy of this model was demonstrated by its accessibility to double layer solutions and the close resemblance it bears to the expected analytical results when a thermal parallel distribution is added. In the subsequent chapter we extend our one-dimensional results to preliminary ones in two dimensions.

Chapter 5

One Dimensional Particle Simulation

In the previous chapter we explored the static local and global solutions to Poisson-Vlasov equations. This, as well as previous theory, lacks from the ability to observe time dependent behaviour—instabilities, stationarity, and accessibility. While experiments allow observation of these phenomena, often they suffer from constraints of physical accessibility, range of parameter exploration and cost. In this chapter we compare the solutions in the previous chapter to those using particle simulation.

Previous simulations were limited in variety of particle and field boundary conditions allowed. Our model advances beyond these to allow injection with floating potentials in a bounded simulation so that the double layer isn't predisposed by initial conditions. While the electric field is calculated in one dimension only, thus 1D, the magnetic field is a realistic one required for observing effects of the magnetic moment. Once injected, particles are free to explore all of position and velocity space allowed by the one-dimensional potential and the three-dimensional magnetic field.

5.1 Physical Model

The physical model is that of auroral field lines with one end tied near one of the earth's magnetic poles and the opposite embedded near the reconnection zone far from the earth, but this model may apply equally to other "mirror" configurations.

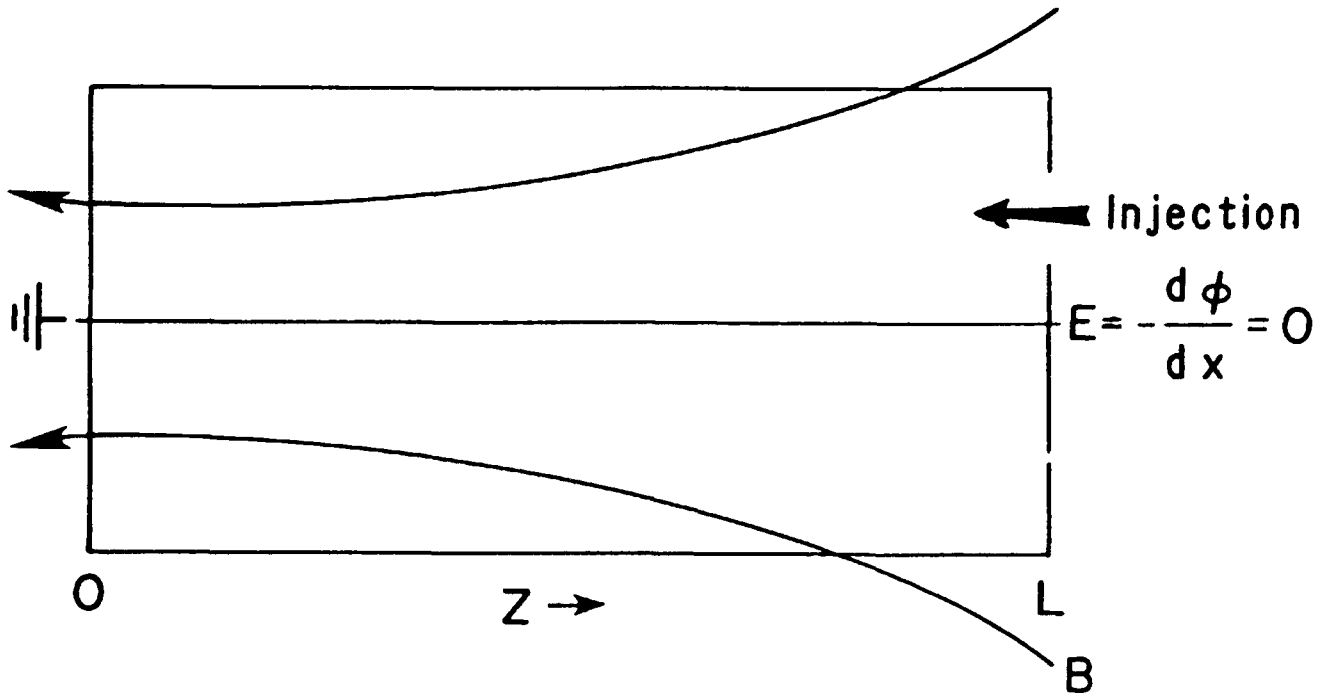


Figure 5.1: A projection of the simulation region. Particles are injected into a box at the right boundary ($z=L$) where symmetry requires the electric field to be zero. The axis of the simulation is that of the dipole magnetic field. The potential on the left boundary ($z=0$) is defined as $\phi=0$.

5.1.1 Particles

Currentless plasma enters the modeled region from the reconnection zone streaming towards the earth with injection velocities $v_d \sim 1000 \text{ km/s}$, yielding ion kinetic energies $K \sim 10 \text{ keV}$. Temperatures are $T_e < T_i \sim 1 \text{ keV}$. Both the density and magnetic field are functions of distance from the earth, R . Extrapolating $v_A = 500 \text{ km/s}$ [38, p. 7180] in the tail region of the magnetosphere where $R \sim 10R_E$ to the ionosphere where $R \sim R_E$ and using $v_A \propto \frac{B}{\sqrt{n}}$ and $n \propto B$ yield densities $n \sim 100 \text{ cm}^{-3}$.

In this region particle and field scale lengths are

$$\lambda_D \sim \rho_e \ll \rho_i \ll R, \lambda_D \leq l \leq R,$$

where R is the B field scale length and l is that expected for E . Similarly, the frequency ordering is

$$\Omega_i < \omega_{pi} \sim \omega \ll \Omega_e \sim \omega_{pe},$$

Ω the gyrofrequency. Particle collisions may be ignored.

5.1.2 Electric Field

For these parameters, $\beta \ll 1$. In this regime electrostatic (ES) and electromagnetic (EM) waves are decoupled [46, p. 224] and [28, p. 427], and we

may choose an ES solution to Maxwell's equations. The boundary conditions for the electric potential are chosen as $\phi = 0$ at $z=0$ (the ionosphere or mirror throat) and $E=0$ at $z=L$ (the magnetosphere or mirror center.) Assuming that the same physical processes drive phenomena at both the North and South poles requires these potentials and charge distributions to mirror one another about the equatorial plane of the earth. While disallowing odd solutions to Poisson's equation, this assumption leads to the condition $E(L)=0$. The condition at $z=0$ derives from the presence of high density regions of ionized gas near the earth's poles. Taking the poles as electric ground while assuming local charge neutrality requires $E=0$ throughout the regions and $\phi(0) = 0$. (For discussion of these boundary conditions see [15] and [48].)

5.1.3 Magnetic Field

We use the exact dipole field of Section 2.2.1. However, taking the electric field scale as K/l with $l \ll R$ for a double layer and $mv^2 \sim T$,

$$\frac{mv^2/R}{qE} \ll 1,$$

permitting us to ignore curvature drifts by centering the model and aligning the direction of the electric field along the magnetic field axis. The value of the field is chosen so that at the model's center the magnitude of the field is equal to that at $R = 2.5R_E$ directly above the poles. However, to reduce the size of the simulation region, the magnetic field scale length is reduced while maintaining the above relative parameters. Bounding the computational model are injection and loss planes perpendicular to the magnetic field axis.

5.2 The Computational Model

We primarily choose parameter values for our simulation to maintain frequency and length scalings. In part, these values mirror those of the physical model (Figure 5.1.) However, a particle simulation is limited by numbers of particles and simulation size and duration. Therefore, use of this tool requires careful abstraction of both physical processes and parameters.

5.2.1 Electric Field

Electric Field Grid

To calculate the electric field we divide the computational model at equispaced grid points defined by intersection of intermediate planes perpendicular to the magnetic axis. At each time step particles are assigned to grid points centered between planes to obtain charge density. The electric field is solved and the particles are moved according to the electric force interpolated to their positions.

The grid length, Δ , is chosen as λ_D . 1D simulation theory for no (or constant) magnetic field has demonstrated the effectiveness of this choice [23]. In the presence of magnetic field gradients, however, the density is not uniform and one may propose the smallest " λ_D " to capture fine scale behaviour at the highest densities. We have chosen λ_D at the injection point.

Charge Sharing/Force Interpolation

In our 1D simulation we use an interpolation scheme which assigns particle charges to grid points, x_g ,

$$\delta_{ig} \equiv \begin{cases} q(1 - \frac{|x_i - x_g|}{\Delta}) & , |x_i - x_g| < \Delta \\ 0 & , |x_i - x_g| > \Delta \end{cases}$$

and interpolates particle force from electric fields at gridpoints, E_g ,

$$F_i = \sum_g \delta_{ig} E_g$$

Because electric fields are calculated in the axial direction only, the same equations are obtained by considering particles to be constant density slabs of infinite cross section but finite thickness, Δ , and basing charge sharing/force interpolation on the particle volume in each cell. This scheme is known as cloud-in-cell (CIC) weighting [5, p. 311].

Poisson Solver

The charge sharing scheme above results in a grid charge density

$$\rho_g = \sum_i \delta_{ig},$$

where the summation is over individual particles, i .

Direct integration of Poisson's equation 3.1(a) in 1D,

$$E_g - E_{g+1} = \rho_{g+\frac{1}{2}}\Delta,$$

is fast and easily implemented. However, especially for diagnostics, advantages accrue by using a Fourier solver. Some authors have advocated straightforward application of continuous Fourier transforms to the discrete case [17]. In general, these methods don't account for effects of aliasing, which may predominate in bounded simulations. After correcting for these aliases, using techniques developed in Appendix B, their effects are ameliorated and the Fourier transform results closely agree with those obtained by direct integration. Thus, direct integration was used for the 1D simulation while post-processing diagnostics incorporated corrected Fourier transforms.

5.2.2 Particles

Particle Pusher

While taking advantage of axial symmetry, particle acceleration is calculated with a full pusher or, for electrons, a guiding center (gc) pusher. In this chapter we primarily report results from the full pusher,

$$\vec{v}_{\frac{1}{2}} - \vec{v}_{-\frac{1}{2}} = \frac{q\Delta t}{m} \left[\vec{E}_0 + \left(\frac{\vec{v}_{\frac{1}{2}} + \vec{v}_{-\frac{1}{2}}}{2} \right) \times \frac{\vec{B}_0}{c} \right]$$

This equation, along with its position counterpart,

$$\frac{\vec{x}_1 - \vec{x}_0}{\Delta t} = \vec{v}_{\frac{1}{2}},$$

constitutes the "Leap-Frog" scheme (Eqn. A.1).

In the next chapter we report results in 2D using a gc pusher (Eqn. A.3). The full and gc pushers yield similar results in 1D. In practice, however, the charge to mass ratio (q/m) is chosen to retain the appropriate scale lengths while relaxing the required number of time steps to observe the desired physical phenomena. At injection care is taken to retard particle positions by a half time step in adherence to the leap-frog scheme.

Particle Velocity Distributions

Particles are injected at the low-field side of our cylindrical box of length $L \equiv N\lambda_D$. To simulate a warm plasma accelerated by external processes, the injected particles would be drawn ideally from a drifting Maxwellian velocity distribution. However, previous authors demonstrated “energy instabilities” attributed to current flow through a boundary at floating potential [48]. Because we expected a time-dependent potential at the injection boundary, we sought a computational model which retained features of particle mirroring and drift while allowing simple and current-free injection.

For both ions and electrons we use a cold (delta-function) distribution,

$$f_0 = An_0\delta(v - u) \exp \frac{-mv_{\perp}^2}{2T},$$

the injection probability is simply $P=1$ for $v \equiv v_{\parallel} = u$ and 0 otherwise. This approach permits a simple numerical algorithm for particle injection while avoiding these “energy instabilities.” As presented in Section 4.2, this distribution allows straightforward comparison to results expected from a more general drifting Maxwellian. Indeed, while this distribution results in simulations consistent with our analyses, thermal processes permit direct extension of our results to more general situations than this simple approach might suggest. These aspects will be discussed below.

Particle Injection

The number of particles penetrating a boundary of cross section, A , during each time step, Δt , is

$$\int d\vec{A} \cdot \int f\vec{v}d\vec{v}\Delta t \equiv \Gamma\Delta tA$$

The flux for an azimuthally symmetric distribution along the magnetic field axis,

$$\Gamma = \pi \int dv_{\perp}^2 \int dv_{\parallel} f(v_{\parallel}, \vec{v}_{\perp})v_{\parallel},$$

is weighted by its parallel velocity.

At any particular time step the probability for injection with perpendicular velocity of magnitude greater than $v_{\perp} \equiv |\vec{v}_{\perp}|$ is

$$P(v_{\perp}^2) = \int_{v_{\perp}^2}^{\infty} dv_{\perp}^2 g(\vec{v}_{\perp}) / \int_0^{\infty} dv_{\perp}^2 g(\vec{v}_{\perp}) \text{ where } g \equiv \int_{-\infty}^{\infty} dv_{\parallel} f(v_{\parallel}, \vec{v}_{\perp})$$

Noting that $P(0)=1$, to distribute velocities for a perpendicular Maxwellian distribution ($g \propto \exp -mv_{\perp}^2/2T$), we simply choose

$$v_{\perp}^2 = \frac{2T}{m} \ln P(x)$$

where $P(x)$ is a uniform probability distribution and x is a pseudo-random number distributed on the interval $x \in [0,1]$.

In our simulation the particle injection rate is $N/\Delta t = n_0 v_0 A$. This quantity is fixed by choice of the three parameters, n_0, v_0 , and Δt . To inject discrete particles, one may either choose these parameters for integer injection number, N , or he must account for residual particles left behind at each time step. To maintain a currentless boundary, the actual injection was most often performed by placing electron guiding centers on top of ions' and injecting a fixed number of these pairs with identical parallel velocities at each time step.

Particle Boundary Conditions

Particles that exit at $z=L$ are mirrored to the position $2(L-z)$ with perpendicular velocities identical to, but parallel velocities opposite, the previous time step. Various schemes were used at $z=0$.

Replacing particles at $z=0$ without considering their attributes, such as "recycling" particles by exchanging those lost at $z=0$ with replacements at $z=L$, generally do not conserve energy. Therefore, particles lost at $z=0$ were most often simply allowed to escape, requiring the potential to maintain overall system charge neutrality. That is, a sheath was formed.

One alternative was to replace hot plasma, lost during time scales of interest, with backscattered ionospheric particles cooled by collisions with neutrals. Steady state requires that the total flux of hot charge balances that of cold. Approximating $v \approx \sqrt{\frac{T}{m}}$,

$$\begin{aligned} \Gamma_{cold} &= -\Gamma_{hot} \\ n_{cold} &= \frac{(nv)_{hot}}{v_{cold}} \approx n_{hot} \sqrt{\frac{T_{hot}}{T_{cold}}} \end{aligned}$$

This technique was used to study the effects of these fluxes on simulation results and agrees with results we report below except, as noted, the approximation $\Delta\Gamma = 0$ ameliorates the need for a sheath.

5.3 Simulation Results

5.3.1 Simulation Parameters

We present results from a simulation with $N_g \equiv L/\lambda_D = 1024$, $M/m = 25$, $\omega_{pe}\Delta t = 0.25$, and mirror ratio $\gamma \approx 25$ with B at the center point of the model equal to that at $R = 2.5R_E$ and an injection density $n_0 = 100\text{cm}^{-3}$. Perpendicular velocities are normally distributed with $T_i = 2T_e = 1\text{keV}$. The ions and electrons share a common injection velocity $v_{inj} = .6\sqrt{2}v_{the}$. These values yield $\omega_{pe} \sim \Omega_e \sim 10^5$, $\lambda_D \sim \rho_e \sim 10m$, and $\rho_i \sim 100m$. Even in the absence of particle collisions the ion bounce time and loss cone size determine the extent to which the ion velocity distribution is characterized by the injected beam. A crude estimate of the bounce time is $\tau_b \sim 1000/\omega_{pe}$ which allows sufficient time for the bulk of the injected ions to be reflected by the magnetic field, but only few ions may complete an “orbit” in z .

5.3.2 Chronology

In Figure 5.2 are plots of velocity space vs axial position at times $\omega_{pet} = 2100$ and 3300 for a charge neutral plasma injected at $z=L$. The instantaneous relative charge density and electric field are also plotted and can be compared to the simulation’s progress in velocity space.

As the plasma drifts into the dipole magnetic field, a strong electric field is evident by the acceleration of electrons and slowing of ions at $z \approx 700\lambda_D$ for $\omega_{pet} = 2100$ and $z \approx 750\lambda_D$ for $\omega_{pet} = 3300$. Acceleration is apparent in the growth of phase space and increase in average velocity to $\langle v_e \rangle \approx 1.25-1.5v_{the}$ at $\omega_{pet} = 2100$ and $\langle v_e \rangle \approx 2.0v_{the}$ at $\omega_{pet} = 3300$ for electrons and by their contraction and decrease for ions. The instantaneous electric field and charge densities are maximum near these points, indicating a potential drop.

Electrons are rapidly scattered in parallel velocity while ions slowly fill velocity space behind the potential. The width of the electron distributions implies that their effective parallel temperature is much greater than the injection temperature. Underlying the velocity space plots are oscillations $\Delta v_e \sim v_{the}$ with scale lengths $\lambda \sim 10s\lambda_D$ for both ions and electrons. One also notes that the potential moves toward the “equator” at a velocity $v_{DL} \sim (100\lambda_D)/(1200/\omega_{pe}) \sim .1v_{the} \leq v_{thi}$ and that its movement coincides

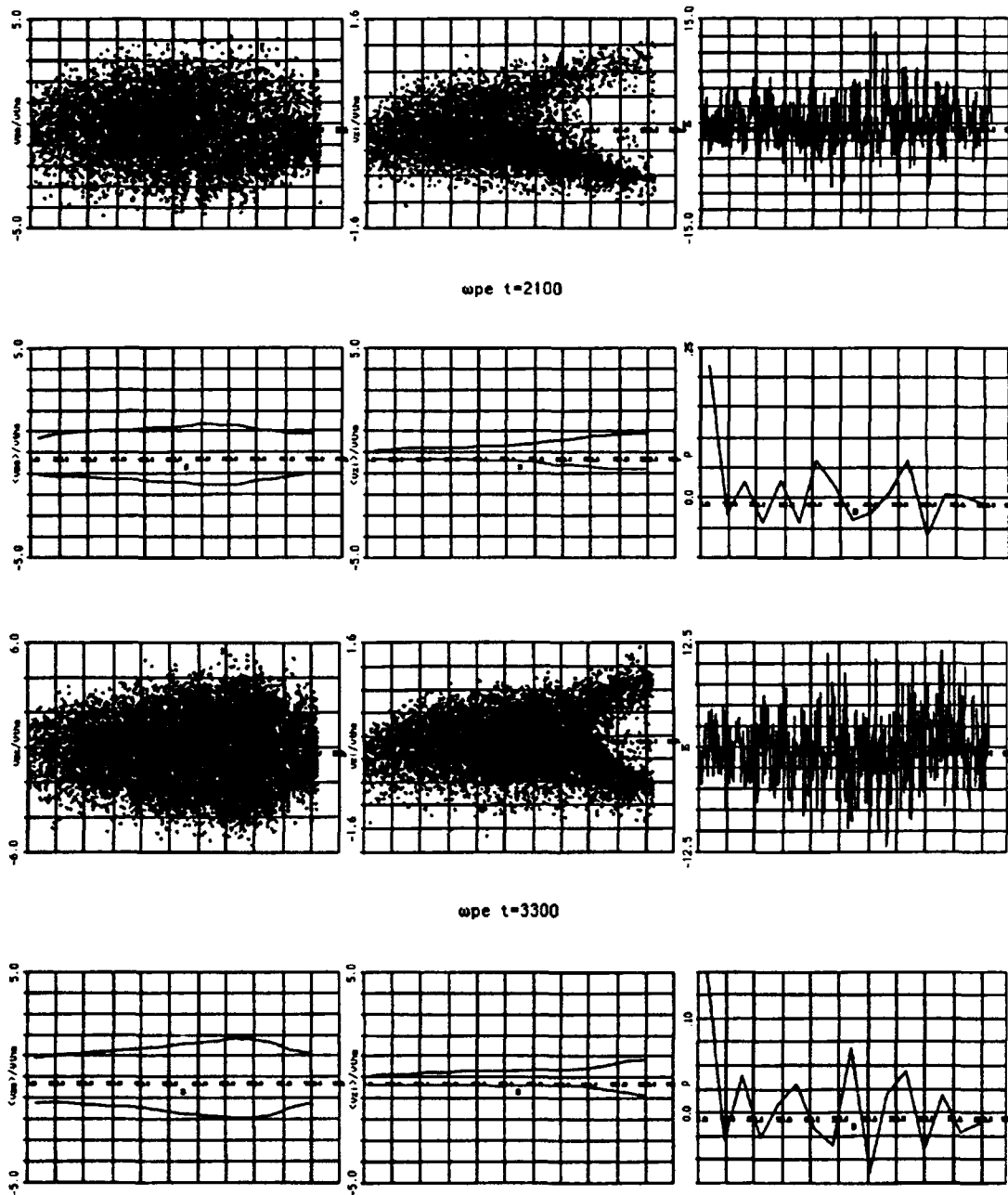


Figure 5.2: Plotted in these two sets of panels are phase space ($v_z - z$) (top) and average velocities (bottom) for electrons (left) and ions (center) in units of electron thermal velocity, plots of the electric field acceleration per time step (change in parallel velocity) normalized to the thermal velocity (top right), and instantaneous charge density normalized to the injected particle density averaged over several cells (bottom right). The spatial grid is graduated in units of $s \equiv z/\lambda_D = 100$. For this simulation particles are injected at $s=1024$ on the right with the “ionosphere” on the left at $s=0$. The plots are for two different times $\omega_{pe}t = 2100$ (above) and 3300 (below).

with the filling of ion velocity space.

5.3.3 Velocity Distributions

Shown in Figure 5.3 are electron and ion velocity distributions at times $\omega_{pe}t = 2100$ (top) and 3300 (bottom) at eight equally spaced grid points from $s \equiv z/\lambda_D = 64$ (upper left) to 960 (lower right). For large z two ion beams are clearly present. The peaks of these beams converge until, beyond the potential drop of Figure 5.2, they are indistinguishable. The asymmetry in the electron distribution at large z indicates velocity components in both, but particularly the forward (injection), directions. For intermediate z values the effect of the electric field is evident where the electron distribution spreads and flattens. At smaller z the distribution spreads to greater and greater widths but then again narrows.

Accounting for differences in mass, the spread of the two species' velocities are comparable at large and very small z , indicating roughly the same temperatures. However, near the potential drop the ions remain beams and their velocities spread relatively less than those of the thermal electrons. These observations are borne out in the next two figures (5.4 and 5.5) obtained for a gc simulation with parameters identical to this simulation except for $\frac{T_i}{T_e} = 1$ at injection.

5.3.4 Stringer Plots

Figures 5.4 and 5.5, as those presented by Stringer[47], display velocity differences and temperature ratios as functions of position for each pair of constituents in counterstreaming plasmas. One set, Figure 5.4, portrays differential (current-carrying) flows between ions and electrons. The other set, Figure 5.5, displays differential ion-ion, electron-electron and ion-electron flows between counterstreaming neutral beams. At right of each set of differential velocity and temperature ratio plots are their point values for each of several positions along the axis. Comparison of these plots to regions of instability, while considering differences in ion mass and a factor of two difference in like species counterstreaming velocities, were intended to identify possible regions of instability.

Stringer's plots were based on drifting Maxwellian distributions and a realistic mass ratio (1836). But, as discussed in Section 5.4.3 below, our

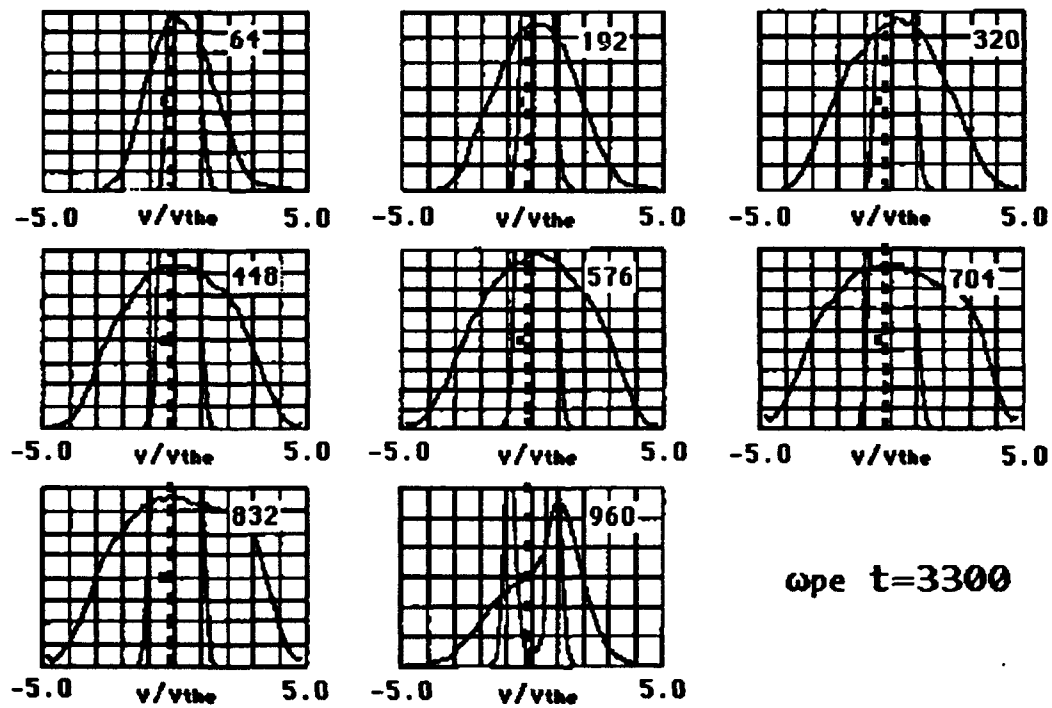
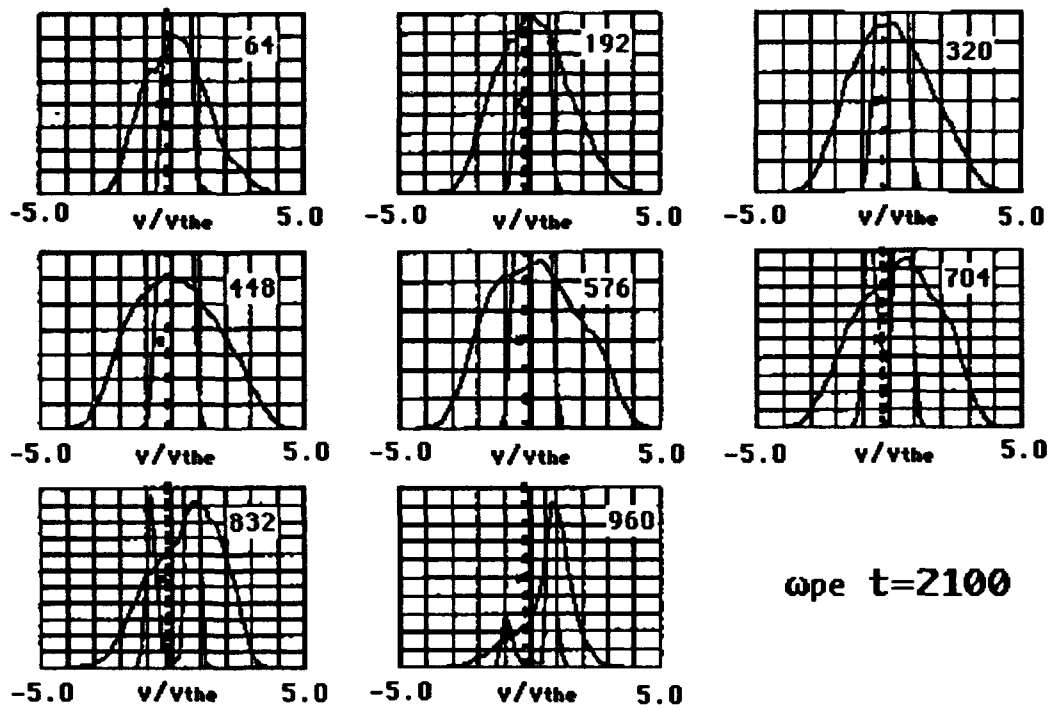


Figure 5.3: Relative densities of electrons and ions in velocity space graduated in units of v_{the} .

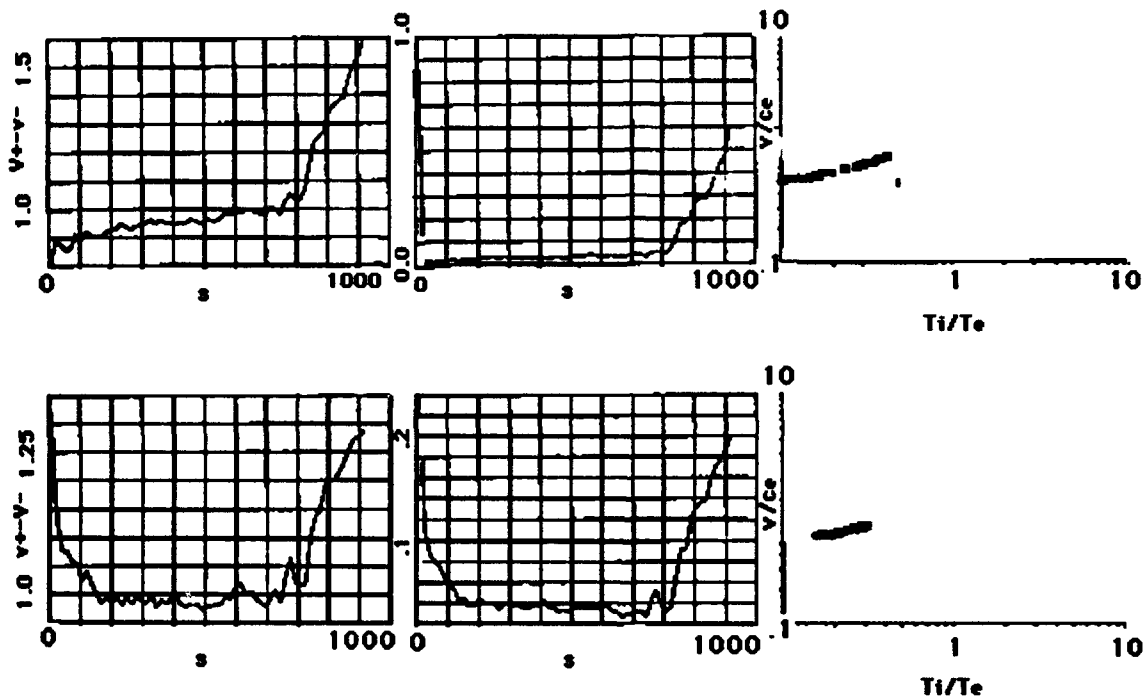


Figure 5.4: These are current carrying flows at $\omega_{pe}t = 2600$. The top figure displays positive flowing ions and negative flowing electrons. The bottom is the opposite comparison. Differential velocities are in units of v_{the} while the position is graduated in units of 100s of Debye lengths.

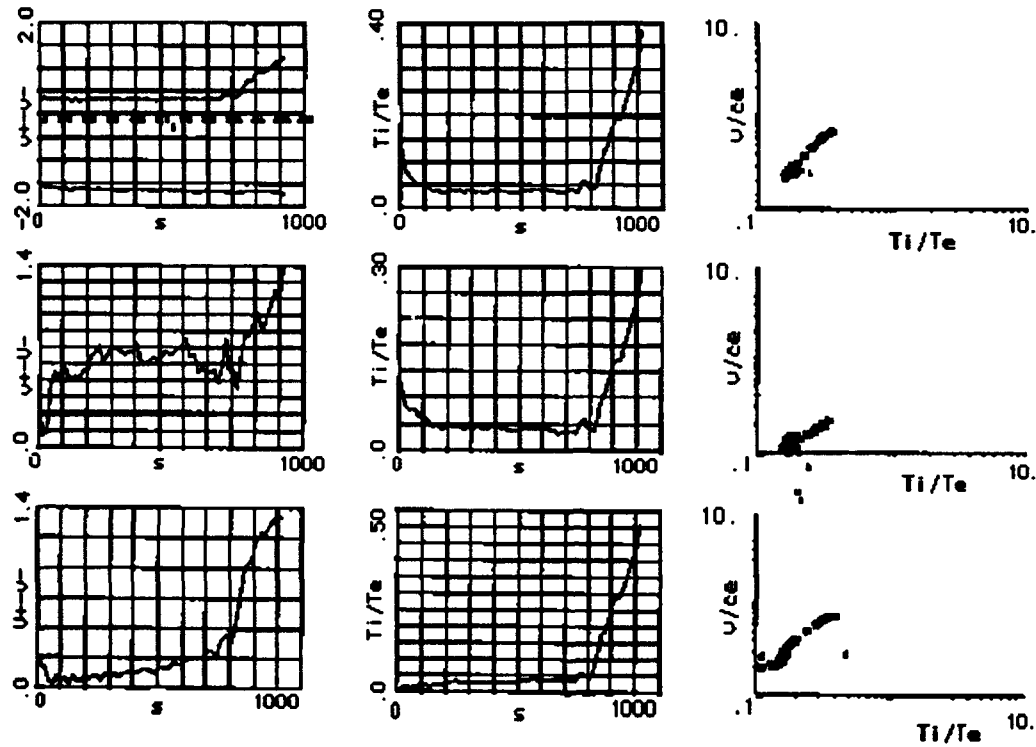


Figure 5.5: The same comparisons as the previous figure's but for counterstreaming neutral beams. The top left panel represents counterstreaming ions (positive velocities) and electrons (negative velocities). Because the e-e wave is unstable at any temperature for $\Delta v > 2.6v_{the}$, it is omitted from the adjoining two plots. The two bottom rows represent the negative (top) and positive (bottom) ion beams interacting with the combined electron beams.

simulation certainly leads to other nearby distributions. Therefore, comparison of these plots to those of Stringer yield only marginal evidence of instabilities. However, of note are the depressed temperature ratios between component ions and electrons, roughly coinciding to the region following the double layer. These plots are also useful for observing the velocities of individual beam components. At left, in Figures 5.4, we have the presence of a sheath. In Figure 5.5, the top left panel indicates the effect of the potential in slowing the ions. Irregularity of negative velocities in the middle left plot admits to instabilities.

5.3.5 Electric Field Potential

The relative charge densities, electric field, and electric potential are plotted in Figure 5.6 around $\omega_{pe}t = 2750$. While the electric field acceleration remains small during any time step, the cell to cell variation in density can be quite large. A smoothing algorithm, used to “best fit” the data within bands of fixed “standard deviation”, resulted in the continuous curves in the density and electric field plots. A double layer is evident at $z = 800\lambda_D$, where there is a large potential drop, a spike in the electric field, and the characteristic back to back positive and negative layers of charge. A smaller double layer is apparent at $z \approx 875\lambda_D$. The magnitude of the maximum potential drop is $V \sim 6.5 - 7.5$, while the total potential difference between particle injection at $z=L$ and loss at $z=0$ is 3.25. Also apparent is a sheath at $z = 0$, indicated by the presence of the negative electric field gradient and the jump in potential.

5.3.6 Wave Spectra

At right of the electric field and potential in Figure 5.6 are the energy densities in k-space. The mode structure gives wavelengths most strongly peaked near $k = 0$ and around $k\lambda_D/\pi \sim .1$. These correspond to longer scale lengths visible in the electric field, $l \sim 40\lambda_D$, and shorter ones, $\frac{T}{cE} \sim 20\lambda_D$, apparent in the potential and charge density.

Plotted in Figure 5.7 are the frequency spectra for different positions. These spectra are measured in the rest frame of the simulation but are Doppler shifted ($\omega \pm kV$) by the constituents’ velocities. The units of the abscissa are tenths of $\pi\omega_{pe}$. The spectra are most strongly peaked

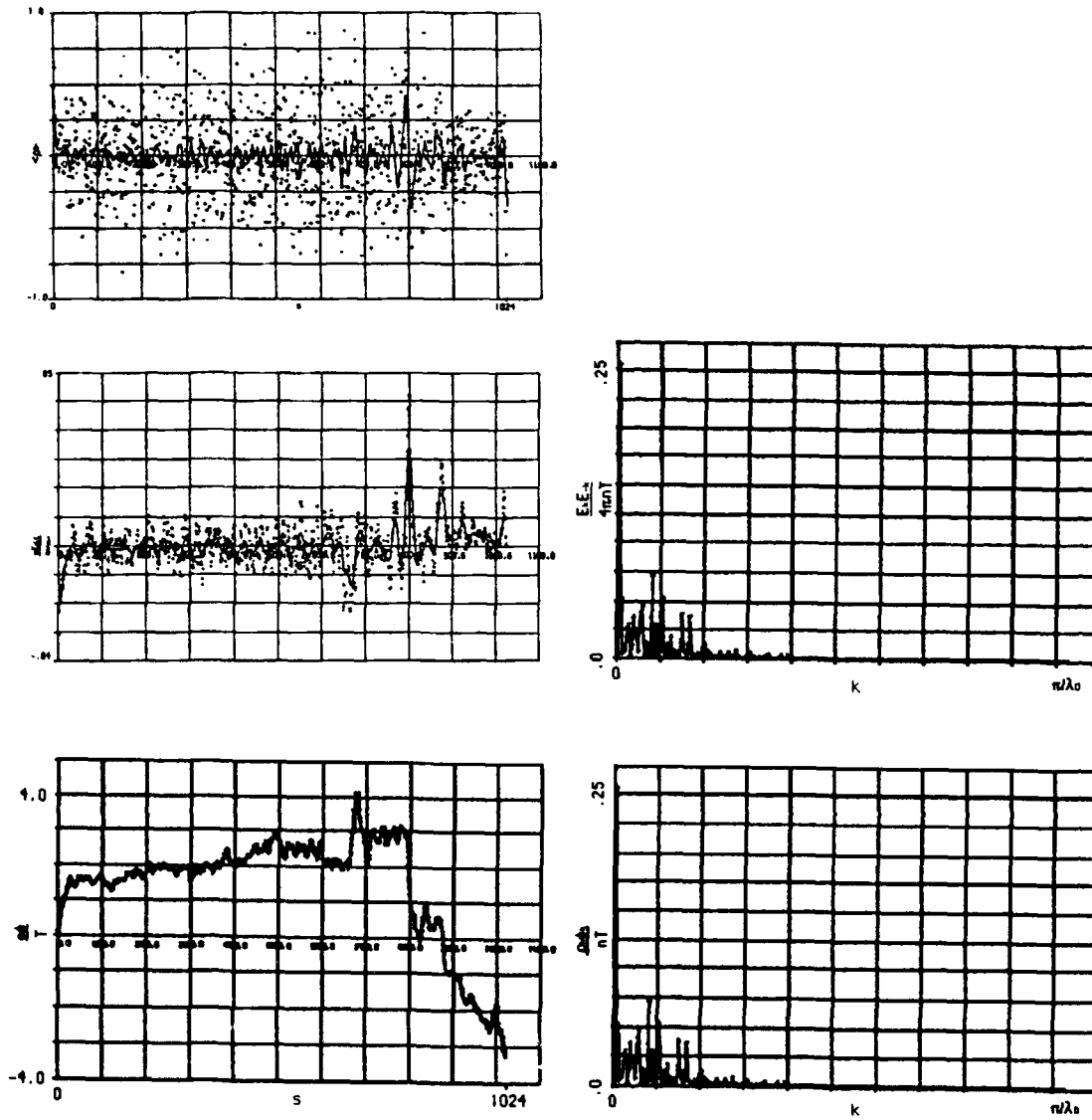


Figure 5.6: Plotted on this panel at left are the normalized charge density (top) and electric field (middle) averaged from $\omega_{pe}t = 2750$ to 3000. On the bottom is the electric potential normalized to the perpendicular injection temperature. At right are the Fourier energy densities $E_k^2/4\pi$ (top) and $\rho_k \phi_k$ (bottom) normalized to particle thermal energy density. The abscissa for these plots is the wavenumber $n = \frac{N_e \lambda_D}{\lambda}$. The potential and spectra are averaged over $100 \omega_{pe} \Delta t$ centered at $\omega_{pe}t = 2750$.

near 0.3 for large z and around .06 and its harmonics for decreasing z . These correspond to oscillations at the electron and ion plasma frequencies respectively.

5.3.7 Energies

In Figure 5.8 we plot energies normalized to the injected energies of the particles measured during the simulation. By $\omega_{pe}t \approx 1250$ the plasma has crossed the simulation region and energy is lost at $s=0$. Loss rates of ion and electron energies indicate comparable exit currents as required to maintain overall charge neutrality in the simulation. The collective potential energy is a small fraction of the total. Midway through the simulation the waves have saturated and the ion and electron energies approach steady state with the ion energy about twice that of the electrons. As evident in the first panel, total energy is conserved to within much less than 1 percent.

5.4 Discussion

5.4.1 Plasma Instabilities

Although a spread in parallel velocities is a natural consequence for mirroring particles with thermal perpendicular velocities, the observed shape of the distributions in these simulations is accounted for only by additional processes. In absence of "collisions" the parallel distribution function for the two species is, using the notation of Chapter 4 (Eqn. 4.5),

$$g \propto \frac{2\pi A}{m} \frac{B}{\Delta B} \exp\left(-\frac{K_0 - V - K}{Y}\right) H(K_0 - K - V)$$

and the peaks of the two species separate as they encounter the increasing quasineutral potential. Owing to the Heaviside function, the shape of these distributions presents a cold ion beam but thermal electron distribution to waves traveling at speeds greater than the ion drift velocity but less than that of the electrons and ions, oscillating at their plasma frequency, may be excited by electrons drifting through them. This instability accounts for the observed drifting electron distribution with a peak coincident to the ions', but with a "temperature" on the order of the electric field potential, $e\Delta\phi \sim \mu\Delta B$, necessary to maintain quasineutrality. This temperature

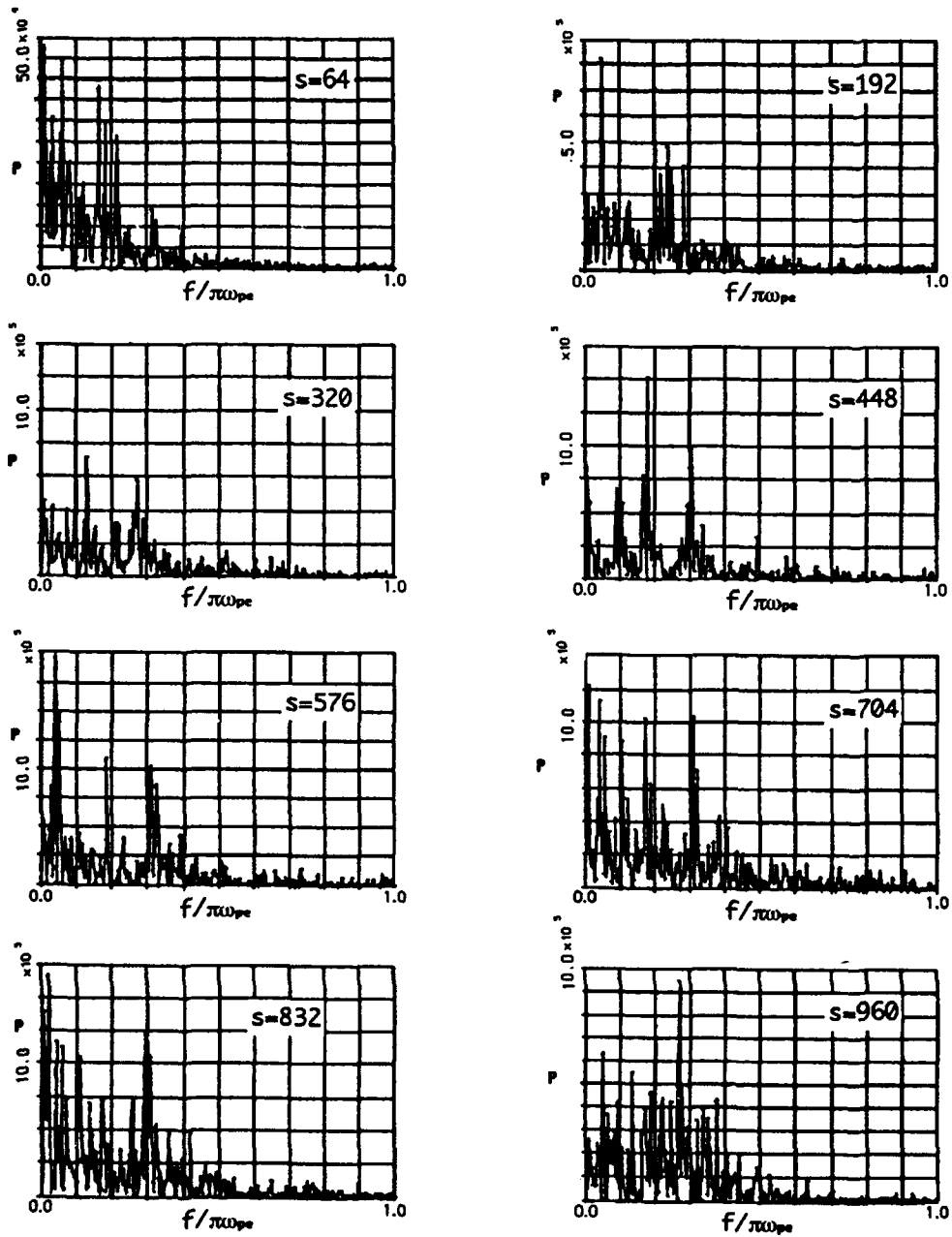


Figure 5.7: In this figure we have obtained the frequency spectra $E_j^2/4\pi$ at different spatial positions as indicated. The abscissa is the frequency normalized to the maximum frequency $f/\pi\omega_{pe}$.

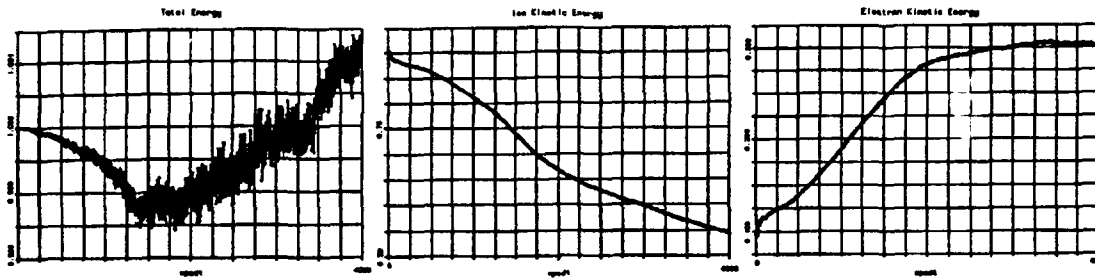
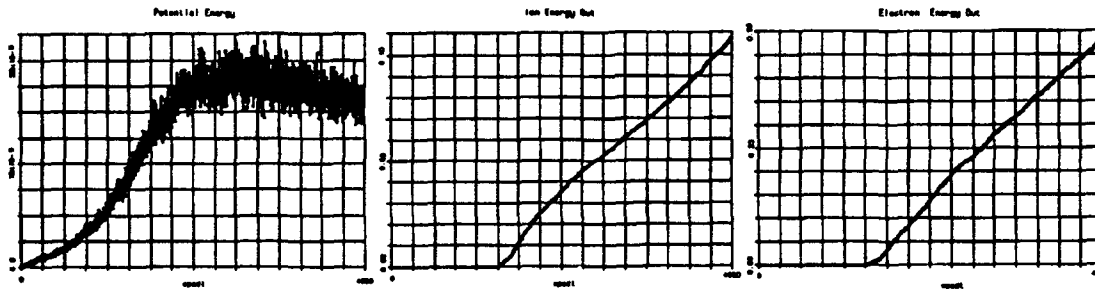


Figure 5.8: Plotted in these panels is the energy budget vs. time ($\omega_{pe}t$) for the simulation. At upper left is total particle energy normalized to the total injected energy. This account is divided between energies of ions and electrons as displayed in the two succeeding panels. At bottom left is the normalized potential energy ($\sum_i q\phi_i/E_{inj}$). To its right is the energy contained in particles lost from the system.



spread is evident both in the plots of the particles' phase-space (Fig. 5.2) and their velocity distributions (Fig. 5.3).

As the beams are reflected by the magnetic field and electrons are accelerated in the double layer potential, the constituents become susceptible to other two-stream instabilities. Electrons in one beam, excited by those in the opposing beam both with mean velocities $v > 1.3v_{the}$, take part in oscillations with $\omega \approx \omega_{pe}$ and $\lambda \sim \lambda_D$ and acquire a spread in velocities on the order of the ions' drift [47].

With $T_i \ll T_e$ the plasma is vulnerable to electron/ion instabilities at the ion plasma frequency. Figures 5.4 and 5.5 show temperature ratios, particularly for down-streaming ions on the high potential side of the double layer, potentially unstable to electron beams drifting through them with velocities greater than $V_c \equiv .924(1.2)\sqrt{2}$ [27], either combined or singly, with two attendant possible modes of oscillation. Consistent with the observed spectra, these oscillations have $\omega \approx \omega_{pi}$ and wavelengths on the order of λ_{Di} , the local λ_D for $T_e \sim \frac{1}{2}Mv_D^2$. Both ions and electrons participate in these oscillations. However, most of the excitation energy is converted to ion thermal energy when the wave, having trapped the ion peak, breaks and heats ions at expense of the bulk of electrons, accelerated by the electric potential. Paranthetically, the ion-ion wave is not permitted in our simulation, since we average charge over a debye length.

5.4.2 A Kinetic Approach to Double Layers

The Langmuir condition requires that the difference in electric field pressure across the double layer be zero. Any difference in pressure will result in movement of the double layer until equilibrium is reached. This equilibrium need not be stationary.

In the rest frame the double layer momentum is

$$P = \sum_{\alpha} \int_{x_-(x,t)}^{x_+(x,t)} A dx \int dv m_{\alpha} f_{\alpha}(x, v, t) v$$

where, as depicted in Figure 5.9, x_+ and x_- are the time-dependent spatial limits of the double layer defined by $n_i = n_e$ and A is its constant cross section. The pressure on its surface must be

$$p = \frac{dP}{Adt} = \sum_{\alpha} \int dv m_{\alpha} v \left[\int dx \left(\frac{\partial f}{\partial t} + \vec{v} \cdot \nabla f \right) + \left(\frac{dx_+}{dt} - \frac{dx_-}{dt} \right) f \right]_{\alpha},$$

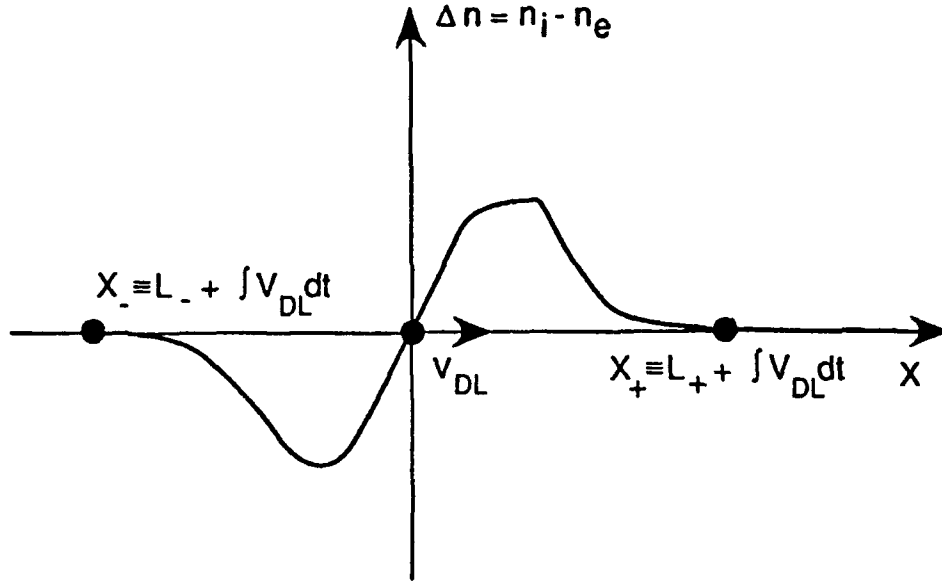


Figure 5.9: This shows the symbology we use for integration through the DL.

where the second term in parentheses is the change in momentum due to movement and changing size of the DL while the first term is the pressure due to the time-dependent behaviour of the particle distributions.

Ignoring collisions and in the absence of instabilities, the Vlasov equation 3.2(a) allows us to substitute for the first term

$$\left(\frac{\partial f}{\partial t} + \vec{v} \cdot \nabla f\right) = -\vec{a} \cdot \nabla_v f$$

The second term may be broken into motion of the DL with velocity $v_{DL}(x, t)$, defined at its center where $n_i = n_e$, and the rate of change in its volume due to movement of its endpoints

$$\frac{dx}{dt} = \frac{d}{dt}\left(L + \int_0^t v_{DL} dt\right) = \frac{dL}{dt} + v_{DL}$$

The equation for the pressure becomes

$$p = \sum_{\alpha} \int dv m_{\alpha} v \left[- \int dx \vec{a} \cdot \nabla_v f + \left(v_{DL} + \frac{dL}{dt}\right) f \Big|_{x_-}^{x_+} \right]_{\alpha}$$

Only acceleration and reflection of ions and electrons in the electric field of the DL contribute to its recoil. This component is present in the first term while the second term admits the resulting movement of the DL.

When the first term is in balance, an equilibrium may exist with $v_{DL} + \frac{dL}{dt} = 0$. For stationary double layers and symmetric velocity distributions the second term vanishes and, in absence of external forces, an equilibrium can only be established with

$$\begin{aligned} \sum_{\alpha} m_{\alpha} \int dx a_E \int dv v \frac{\partial}{\partial v} f_{\alpha} &= \sum_{\alpha} q_{\alpha} \int dx E (v f|_{-}^{+} - \int dv f)_{\alpha} \\ &= \sum_{\alpha} q_{\alpha} \int dx E n_{\alpha} = \int dx E \frac{\partial E}{\partial x} = 0, \end{aligned}$$

where we have integrated by parts and used Poisson's equation 3.1(a). This is Langmuir's jump condition. In steady state, for stationary double layers and non-symmetric particle distributions, current must flow to maintain a momentum balance between accelerated ions and electrons [6].

When one includes wave particle interactions, an additional term, $\frac{\partial f}{\partial t}|_{coll}$, contributes to evolution of particle distributions. The distributions for an injected/reflected pair of beams will no longer be symmetric since reflected beams "carry the memory" of changes in their distributions along the entire path they traverse. That is $f(x, v-) \neq f(x, v+)$. In this instance a non-stationary equilibrium

$$\begin{aligned} \sum_{\alpha} \int dv m_{\alpha} v (v_{DL} + \frac{dL}{dt}) f_{\alpha}|_{-}^{+} &= - \sum_{\alpha} \int dv m_{\alpha} v \int dV (\frac{df_{\alpha}}{dt}|_{coll}) \\ \text{or } P(v_{DL} + \frac{dL}{dt})|_{-}^{+} &= RHS \\ \text{with } v_{DL} &= \frac{RHS}{\Delta P} - \frac{PdL/dt}{\Delta P}|_{-}^{+} \end{aligned}$$

may be found. The physical interpretation is that the double layer will move or change in volume in response to changes in particle momentum [26, p. 5, eq. 27 a,b] until an equilibrium with $v_{DL} + \frac{dL}{dt} = 0$ is reached.

Formally, we may approximate the collision term as

$$\frac{\partial f}{\partial t}|_{coll} = -(\vec{a}_0 \cdot \nabla_v f_1 + \vec{a}_1 \cdot \nabla_v f_0)$$

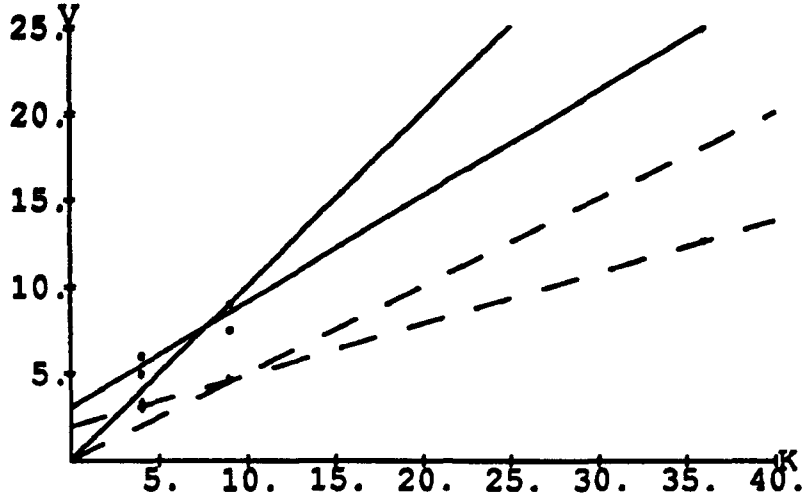


Figure 5.10: Plotted in this figure is maximum potential energy vs. injected ion energy in terms of the particle thermal energy. The analytic expression for the expected points plotted in this graph is given by Eqn. 4.6.

If the scale length of the DL is far removed from the wavelength of the instability ($L \gg \lambda$), we may ignore the contribution of the DL potential to velocity space diffusion from instabilities, that is

$$\frac{\partial f_0}{\partial t}|_{coll} = -\frac{\partial}{\partial v} \left(\frac{q}{m} \right)^2 \frac{E_1^2}{\omega - kv} \frac{\partial f_0}{\partial v},$$

In our simulation with $\frac{\partial f}{\partial t}|_{coll} \approx -\nu f$, $\nu \leq \omega_{pi}$, and $dx \approx \lambda_D \left(\frac{e\phi}{T} \right)$ a rough estimate of the equilibrium drift velocity is $v_{DL} = \nu \lambda_D \left(\frac{e\phi}{T} \right) \leq c_s$ [18], on order of that observed.

5.4.3 Comparison with Plasma Jet Analysis

In Chapter 4 we calculated the potential due to a neutral jet of plasma with constant parallel velocity but with perpendicular Maxwellian velocity distributions. Plotted at Figure 5.10 are the kinetic energies of injected ions vs maximum and total potentials for simulations with different mass ratios. Simulations with cold plasma injected at the “ionosphere” exhibited

little difference between the two potentials and therefore appear as single points.

The two sets of lines visible in the data are estimates of the maximum potential (solid lines) and total potential difference from injection to exit (dotted lines). As discussed in Chapter 4, the maximum maintains local quasineutrality while the injection voltage assures global charge conservation. Our analysis predicted a roughly linear dependence between both potentials and the injected ion kinetic energy. Additionally, the total potential is dependent on both the temperature ratio and the mass ratios of the two species and the mirror ratio between injection and exit. In the limit of large mass and mirror ratios the expected slope for the total potential was $\frac{1}{2}$ of the ion kinetic energy for $T_i = T_e$. These predictions are the two lines passing through the origin.

The second set of lines with non-zero y-intercepts are the least-squares best fits to the data. Use of cold ions and electrons, effective $T_e/T_i \neq 1$, instabilities which modified particle distributions, and caused non-monotonic potentials contributed to differences between the two sets of lines.

We compare the potential expected from two drifting Maxwellians to that from a beam of ions and Maxwellian electrons by dividing the potential into four regions. In the first, the ion density is approximately that for a cold beam where $n_i \propto F \sim \frac{1}{2X}$. For quasineutrality

$$\begin{aligned} n_{eI} = n_{i0} &\equiv n_0 \frac{B_I}{B_0} / \left(1 - \frac{V_I}{K_0}\right)^{\frac{1}{2}} \\ \frac{e\phi_I - \mu\Delta B}{T} &= \ln \frac{B_I}{B_0} - \frac{1}{2} \ln \left(1 - \frac{V_I}{K_0}\right) \\ V_I &\approx \left(\ln \frac{B_I}{B_0} + Y_I\right) / \left(1 - \frac{1}{2K_0}\right) \end{aligned}$$

and, unlike the case for drifting Maxwellians, the potential in region I is only weakly dependent on the ion kinetic energy.

The boundaries of the second region are defined by points just before and after the double layer. Noting that the ion density may increase from its injected value before an inflection point at $F(1.5) = .43$ to a maximum defined by $F(.92) = .54$ [1, p.298], a rough estimate of the magnitude of the DL is obtained by setting the argument of F to 1.

$$\frac{K_I - V_{II}}{Y_I} \approx 1$$

$$V_{II} \approx K_I - Y_I$$

and the maximum potential is $V_M = V_I + V_{II} \approx K_I + \ln \frac{B_I}{B_0}$. The value of the potential drop is directly dependent on the ion kinetic energy at the DL's base. Indeed, since the DL must begin before the inflection point, $\frac{K_I - V_{II}}{Y_I} < 2.25$ or $K_I > V_{II} > K_I - 2.25Y_I$ and $Y_I < K_I/2.25$. The fact that the potential is less than the injected ion kinetic energy relates to the investment of ion energy into thermal energy of the electrons.

One key to double layer existence is the slope of the electron distribution function vs that of the ions. Again, using $n_i \propto F$,

$$\frac{n_{iII}}{n_{iI}} = F\left(\frac{K_0 - V_{II}}{Y_{II}}\right)^{\frac{1}{2}} / F\left(\frac{K_0 - V_I}{Y_I}\right)^{\frac{1}{2}} \leq 2(.54)X_I$$

Similarly, quasineutrality demands

$$\begin{aligned} n_{eII}/n_{eI} &\leq 2(.54)X_I \\ \exp^{V_{II}} &\leq 1.08X_I \\ V_{II} &\leq \ln X_I \\ &\leq \frac{1}{2} \ln \frac{K_I}{Y_I} \end{aligned}$$

This condition is equivalent to a Bohm criteria where the electron slope at the double layer's start is required to be greater than the ions' ($\frac{n_e}{T} > \frac{n_i}{F} \frac{\partial F}{\partial \phi}$) but less than that at the inflection point ($\frac{n_e}{T} < \frac{n_i}{F} \frac{\partial F}{\partial \phi} |_{x=1.5}$). Satisfaction of a similar relationship at the high potential end of the double layer is guaranteed by the shape of the ion distribution function [35].

Because electrons gain and ions lose a substantial fraction of the ion kinetic energy at the double layer, in the third region a decreasing potential may be required to maintain quasineutrality. Generally, however, the potential is relatively flat ($V_{III} = 0$) and we approximate both ions and electrons as beams.

In the fourth region, at the boundary of the simulation, a sheath must exist to balance the electron and ion current losses. For cold beams a rough estimate of the needed potential is

$$V_{IV} = \frac{K_{II} - k_{II}}{2}$$

$$\begin{aligned}
&\approx \frac{Y_I - (V_{II} + k_I)}{2} \\
&= \frac{Y_I - (K_I - Y_I) - k_I}{2} = -\left(\frac{K_I + k_I}{2} - Y_I\right)
\end{aligned}$$

so the total potential for current equality is

$$\begin{aligned}
V_I + V_{II} + V_{III} + V_{IV} &= \left(\ln \frac{B_I}{B_0} + Y_I\right) + (K_I - Y_I) + 0 - (K_I/2 - Y_I + k_I/2) \\
&\approx \ln \frac{B_I}{B_0} + Y_I + K_I/2 - k_I/2
\end{aligned}$$

While the intercepts of the two potentials are sensitive to double layer location and the actual distributions of ions and electrons, the relative slopes between the two potentials observed in our simulations agree well with this heuristic approach.

Chapter 6

2D Simulation

Results for two-dimensional runs are presented for comparison to the one-dimensional results of the previous chapter. Although the physical model is the same as for 1D, the two dimensional simulation requires extending the Poisson solver beyond simple integration used in the previous chapter. We discuss these aspects more fully in Appendices B and C. Similarly, as discussed in Appendix A, refinement of the particle pusher is required to permit following greater numbers of particles contained in our two dimensional “volume” for a reasonable period of time.

6.1 Computational Model

6.1.1 Electric Field

Electric Field Grid

The model and boundary conditions, pictured in the accompanying sketch, are similar to those in z for 1D, but now the electric potential also varies radially in r . Now, to collect charge and compute the potential, a two-dimensional mesh in r and z overlays the simulation region. The cell size for both directions is λ_D , as in the 1D case.

Charge Sharing/Force Interpolation

The weighting scheme chosen in 1D may be interpreted as a dipole expansion of the charge density about the midpoint between cells [29]. In two

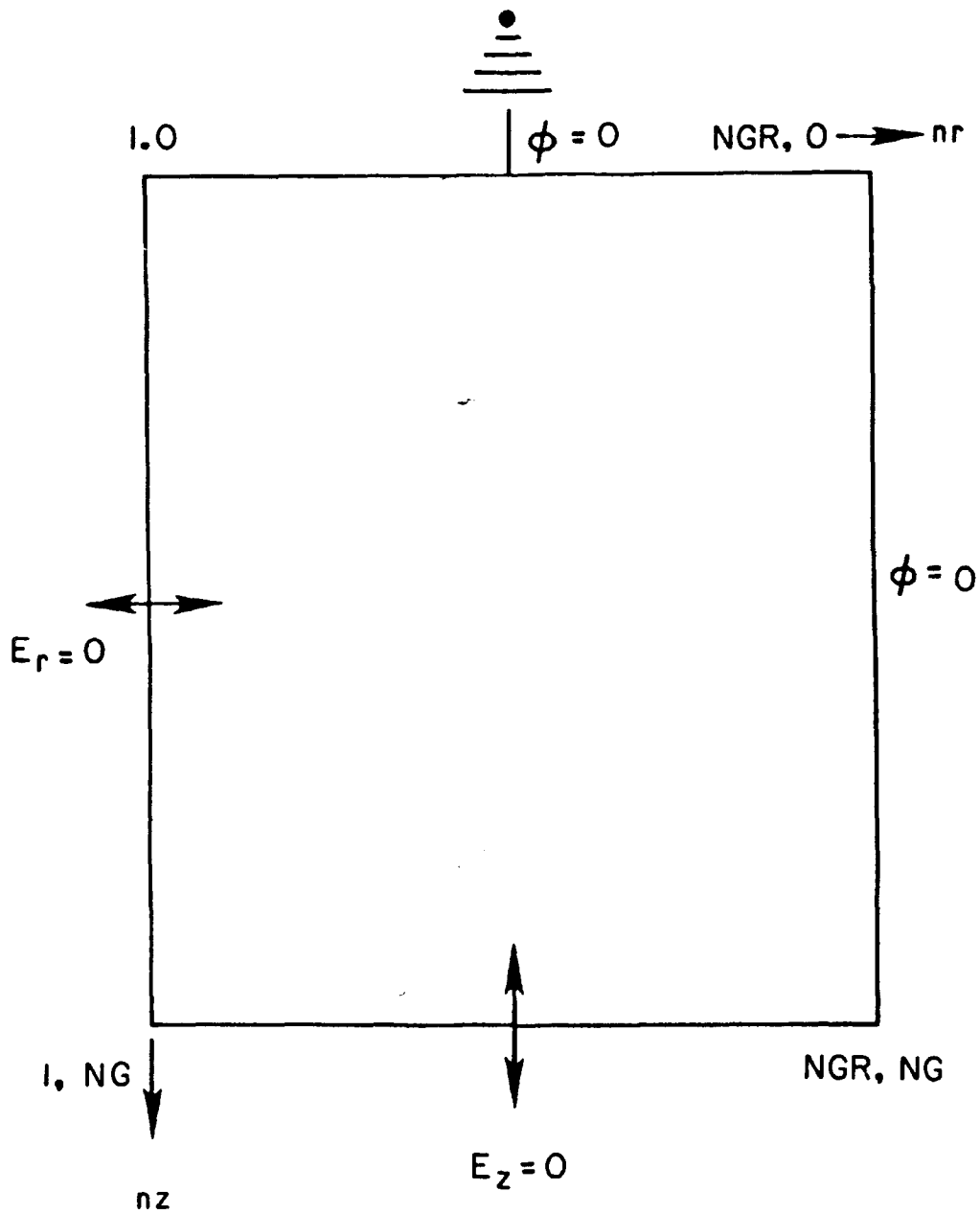


Figure 6.1: The two dimensional model. The coordinates at top left are $z, r=0$. At bottom right they are $z=L, r=R$. Boundary conditions in z are those for 1D. That at $r=0$ are appropriate for continuous charge distributions. Although we show $\phi(R) = 0$, the boundary condition at $r=R$ is flexible.

dimensions a similar expansion including a quadrupole term yields a scheme known as area weighting [5, p. 244]. This approach is roughly equivalent to the scheme used here.

In 1D charge sharing/force interpolation derived from treating particles as plates, one-cell thick of uniform charge density. In two-dimensions (r-z) we may use the same approach in the z direction. In r, however, we treat the particle as a one cell thick ring which varies radially to maintain total charge, $q = \pi\rho(r_{i+\frac{1}{2}}^2 - r_{i-\frac{1}{2}}^2)\Delta z$. Therefore,

$$\rho = \begin{cases} \frac{q}{2\pi r_i \Delta z \Delta r} & i > \frac{1}{2} \\ \frac{\pi r_{i+\frac{1}{2}}^2 q}{\pi r_{i+\frac{1}{2}}^2 \Delta z} & i < \frac{1}{2} \end{cases}$$

where $r_{i+\frac{1}{2}}$ and $r_{i-\frac{1}{2}}$ are the outer and inner bounds of the particle.

Using Gauss' Law, the electric fields at a radial location, r, are

$$rE_r = r_+[\delta E_r(r_+, z_+) + (1 - \delta)E_r(r_+, z_-)]\left(\frac{r^2 - r_-^2}{r_+^2 - r_-^2}\right) \\ + r_-[\delta E_r(r_-, z_+) + (1 - \delta)E_r(r_-, z_-)]\left(\frac{r_+^2 - r^2}{r_+^2 - r_-^2}\right)$$

$$E_z = \delta[E_z(r_+, z_+)\left(\frac{r^2 - r_-^2}{r_+^2 - r_-^2}\right) + E_z(r_-, z_+)\left(\frac{r_+^2 - r^2}{r_+^2 - r_-^2}\right)] \\ + (1 - \delta)[E_z(r_+, z_-)\left(\frac{r^2 - r_-^2}{r_+^2 - r_-^2}\right) + E_z(r_-, z_-)\left(\frac{r_+^2 - r^2}{r_+^2 - r_-^2}\right)],$$

where the pluses(+) and minuses(-) indicate the upper and lower cells into which the particle extends.

The radial and axial electric forces are then calculated as

$$F_r = 2\pi \int_{r_-}^{r_+} r dr \rho E_r \equiv q_+ E_{r_+} + q_- E_{r_-}, \\ \frac{F_z}{q} \equiv E_z = \delta E_{z_+} + (1 - \delta) E_{z_-}$$

One must use care in calculating the force due to the magnetic field. This force should act at the charge center of the particle [8] which is located

at

$$\begin{aligned} r_c &= \sqrt{r_i^2 + \frac{1}{4}} \quad r_i > \frac{1}{2} \\ &= (r_i + \frac{1}{2})/\sqrt{2} \quad r_i < \frac{1}{2} \end{aligned}$$

Poisson Solver

Computation of the electric field is obtained by implementing Buneman's algorithm for mixed boundary conditions (Appendix C), solving for the potential and ultimately the electric fields.

Boundary Conditions

The boundary conditions at $z = 0$ and L are those of the preceding chapter. The boundary condition at $r=0$ attests to the continuous particle distributions—no line charge. For high order radial modes the boundary condition at $r=R$ is flexible. In two dimensions we may express the solutions to Poisson's equation 3.1(a) in terms of Bessel functions (Appendix B)— $\phi(R) = 0$ or $E_r(R) = 0$ just shifts the solution by a node. Since we model a wide enough radial region to expect the presence of several modes, this choice is not critical.

At $r = R$ and $z = 0$ we allow the charge in particles "hanging over the edge" to be lost. At $z = L$ we take advantage of inversion symmetry and mirror particles as for 1D.

6.1.2 Particles

Particle Pusher

For the ions we retain the full Boris pusher of the previous simulations. For the electrons, however, we adopt a guiding center pusher, as described below. In particle pushing schemes including gyromotion, length of the time step is constrained by the gyroperiod (Appendix A.) In a simulation with a magnetic field gradient, such as a dipole's, this limits the magnitude of the magnetic field at exit, and, when the field at injection assumes particular values, ultimately the mirror ratio. We desire to adopt a scheme which

ameliorates this condition. Averaging particle motion over Larmor orbits results in the set [32]

$$\frac{m}{e} \frac{dv_{\parallel}}{dt} = E_{\parallel} - \frac{\mu}{e} \frac{\partial B}{\partial s} + \frac{m}{e} \vec{u}_E \cdot \left(\frac{\partial \hat{e}_1}{\partial t} + v_{\parallel} \frac{\partial \hat{e}_1}{\partial s} + \vec{u}_E \cdot \nabla \hat{e}_1 \right)$$

$$\dot{\vec{R}}_{\perp} = \frac{\hat{e}_1}{B} \times \left\{ -c\vec{E} + \frac{\mu c}{e} \vec{\nabla} B + \frac{mc}{e} \left[v_{\parallel} \frac{d\hat{e}_1}{dt} + \frac{d\vec{u}_E}{dt} \right] \right\}$$

The desirability of time-centered schemes is discussed in Appendix A. In general, this set of equations is not amenable to time-centering. However, in cylindrical coordinates, because both \vec{E} and stationary \vec{B} lie in the $\vec{\rho}, \vec{z}$ plane,

$$\frac{dv_{\parallel}}{dt} = \frac{eE_{\parallel}}{m} - \frac{\mu}{m} \frac{\partial B}{\partial s} + \vec{u}_E \cdot (\vec{u}_E \cdot \vec{\nabla}) \hat{b}$$

and

$$\vec{v}_{\perp} = r \dot{\phi} \hat{\phi} = \vec{v}_d + \frac{q \langle \vec{E} \rangle \times \hat{b}}{m \Omega},$$

where $\vec{v}_d = \left[\frac{\mu(\vec{\nabla} B)_{\perp}}{m\Omega} + \frac{v_{\parallel}^2}{\Omega} \left(\frac{\partial \hat{b}}{\partial s} \right)_{\perp} + \frac{v_{\parallel}}{\Omega} \left(\frac{\partial \vec{u}_E}{\partial s} \right)_{\perp} - \frac{b_z}{\Omega \rho} u_E^2 \right] \hat{\phi}$ is entirely in the $\hat{\phi}$ direction for low oscillation frequencies ($\omega \ll \Omega$) and small radial scale lengths ($\rho \ll R_e$). With axial symmetry this perpendicular component can be ignored in moving particles.

Subtracting \vec{v}_{\perp} from

$$\frac{d\vec{x}}{dt} = \dot{r} \hat{r} + r \dot{\phi} \hat{\phi} + \dot{z} \hat{z}$$

leaves

$$\vec{v}_{\parallel} = \dot{r} \hat{r} + \dot{z} \hat{z}$$

and differentiating the parallel velocity leads to a time-centered expression in the r-z plane,

$$\frac{d\vec{v}_{\parallel}}{dt} = \ddot{r} \hat{r} + \ddot{z} \hat{z} = \frac{dv_{\parallel}}{dt} \hat{b} + v_{\parallel}^2 \left(\frac{\partial b_r}{\partial s} \hat{r} + \frac{\partial b_z}{\partial s} \hat{z} \right)$$

$$\frac{\dot{r}_{\frac{1}{2}} - \dot{r}_{-\frac{1}{2}}}{\Delta t} \hat{r} + \frac{\dot{z}_{\frac{1}{2}} - \dot{z}_{-\frac{1}{2}}}{\Delta t} \hat{z} = \left[\frac{dv_{\parallel}}{dt} \hat{b} + 3v_{\parallel}^2 (1 + \cos^2 \theta) b_{\theta} (\hat{b} \times \hat{\phi}) / r / (1 + 3 \cos^2 \theta) \right]_0$$

Strictly, the guiding center approximation is not applicable within the double layer itself. However, as demonstrated in one dimension, for sufficiently narrow double layers, the pusher well models the bulk of the simulation volume.

Particle Injection

The particles are distributed in r and injected uniformly at the injection boundary. As for our 1D simulation the full dipole magnetic field is superimposed on our mesh. However, for the two dimensional model the dipole is mirrored at the injection boundary ($z = L$), and the symmetric field calculated accordingly. This technique allows injection entirely in the z direction while distributing the particles in r . The radial injection is designed to extend many ion Larmor radii while keeping plasma from being lost out the sides.

6.2 Two Dimensional Results

6.2.1 Simulation Parameters

The attached plots are for a mass ratio of 25, a mirror ratio $\gamma \sim 11$, simulation length of $L = 128\lambda_D$ and width $R = 64\lambda_D$. Temperatures are $T_i = 2T_e = 1000keV$. Both ions and electrons are injected uniformly with $v_{drift} \sim 3\sqrt{2}/5v_{the}$ at the boundary $z = L$ for $r < 32\lambda_D$. These are the same values as for the previous simulations and therefore have the same relative scale lengths and times.

6.2.2 Chronology

As pictured in Figure 6.2, the electrons are reflected rapidly by the mirror field. Initially the electrostatic potential is $\sim kT_e$, as the ions attempt to neutralize the front-going electrons. As for the one-dimensional case, they rapidly attain an effective parallel temperature $\sim kT_e$. Particles with large drift velocity may result from $E \times B$ drifts.

6.2.3 Velocity Distributions

Underlying velocity space plots for both ions and electrons are oscillations of amplitude $\leq kT_e$. As in the one dimensional case, ions fill velocity space. The profile of the velocity distributions, Figure 6.3, moderately into the injection region shows ion velocities embedded in a two-peaked electron velocity distribution. The relative drifts between the electrons not only

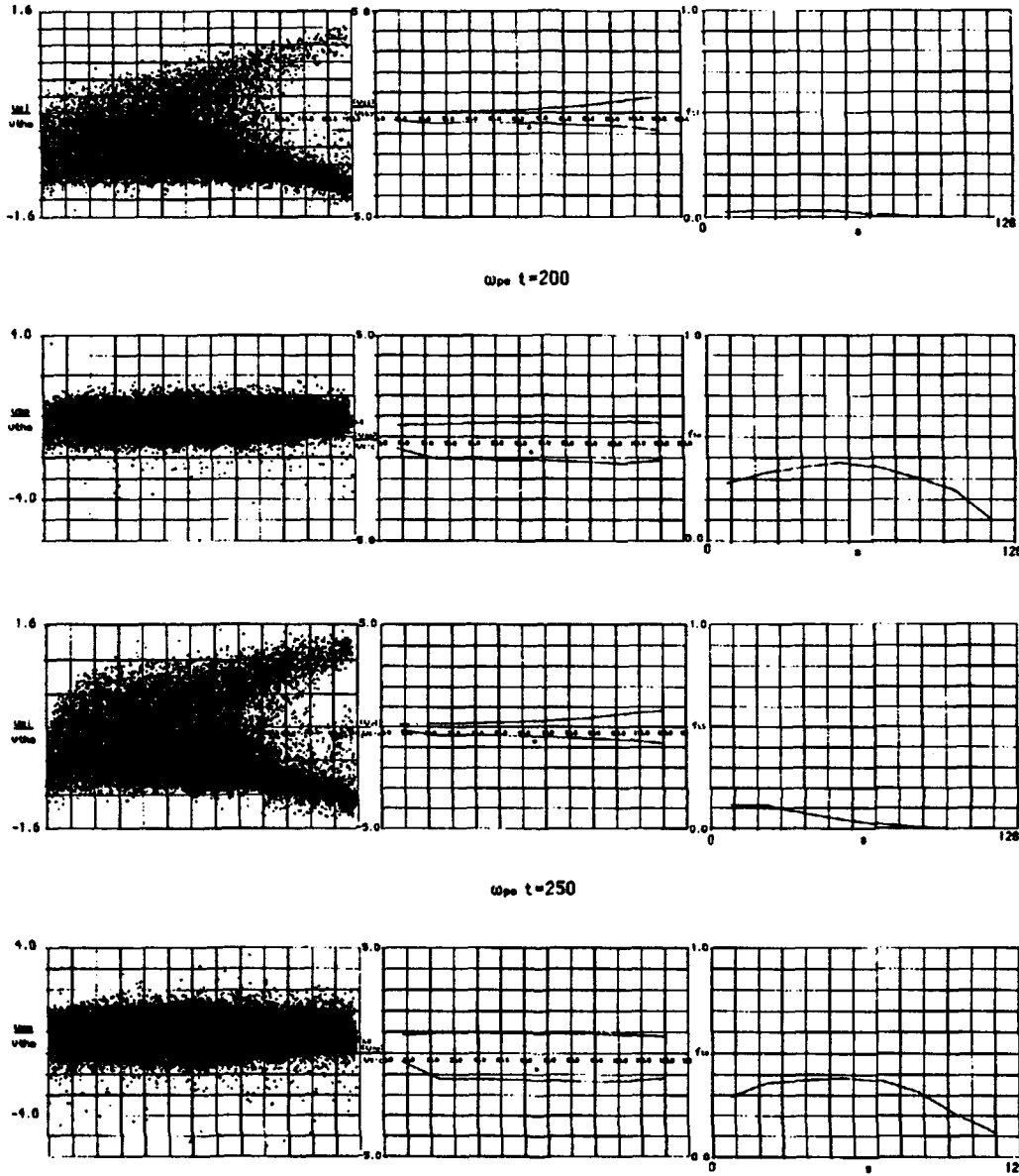


Figure 6.2: Plotted in this chapter are run results for $\omega_{pe}t = 200$ (top) and $\omega_{pe}t = 250$ (bottom). In this figure the left plots are normalized ion (top) and electron (bottom) velocities, the middle set is average velocities, and at right are fractions of trapped (reflected) particles versus axial position. Ion velocities in the left panels are normalized to half the electron thermal velocities ($\omega_{pe}\Delta t = .5$) to which the remainder are normalized.

allow the ions to interact with both distributions but may be sufficient for an electron-electron two-stream instability.

While use of the guiding center pusher eliminates opportunity to observe electron cyclotron waves (partially responsible for diffuse aurorae), one would expect electrostatic ion cyclotron modes ($k_{\perp} \gg k_{\parallel}$) to be present. Even though the simulation proceeds for many $\Omega\Delta t$, the influence of these waves cannot be distinguished from these plots. Overall, the gross results compare well with the ion acoustic scenario presented in the previous section.

6.2.4 Electric Field Potential

The large scale potential is of the order to maintain charge neutrality. At later times, $\omega_{pe}t \sim 200$, a sharp potential drop is readily apparent from $s \sim 75$. The magnitude is $\sim 7kT_e$. However, its movement is not apparent, or it actually may be receding. Reminiscent of the V-shaped potentials encountered in nature [51], the potential contour plots clearly evidence a gross radial scale size of the jet $\sim 32\lambda_D$ (as broadened by the ion gyroradius) necking down to about 1/3 that value at the left boundary, corresponding with a similar increase in B. The local scale size for the potential is far more granular.

Also plotted here, the densities show a marked increase as the particles slow down in the effective potential and then slowly decrease to the left boundary as particles are reflected.

6.3 Discussion

Quantitatively and qualitatively the two-dimensional simulation results agree well with the one-dimensional results. This is evidenced particularly in the velocity space diagnostics. Although we may expect break-down of the guiding center approximation for $\int E_{\parallel} dt$ too great and from ignoring components of particle movement, gross simulation energy is well conserved, as shown in Figure 6.5. The question of stationarity in 2D is open. While, the solutions may be altered by the additional source term ($\frac{\partial^2 \phi}{\partial r^2}$) in the Poissons equation from its 1D form [9], the additional degree of freedom for particles and waves need further exploration.

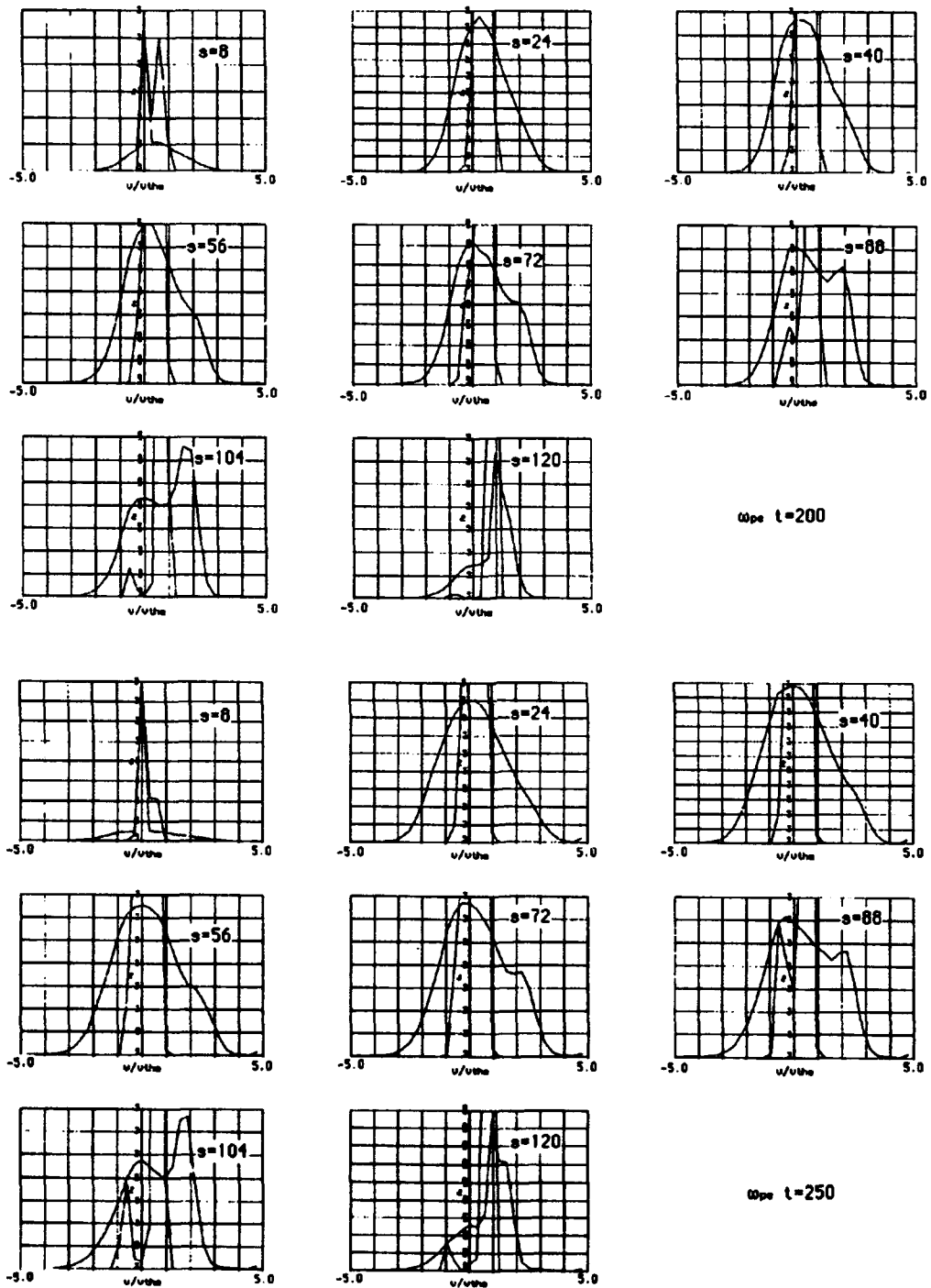


Figure 6.3: Plotted are the velocity distributions for the electrons and ions at eight points from $z = 0$ (top left) to $z = L$ (bottom center).

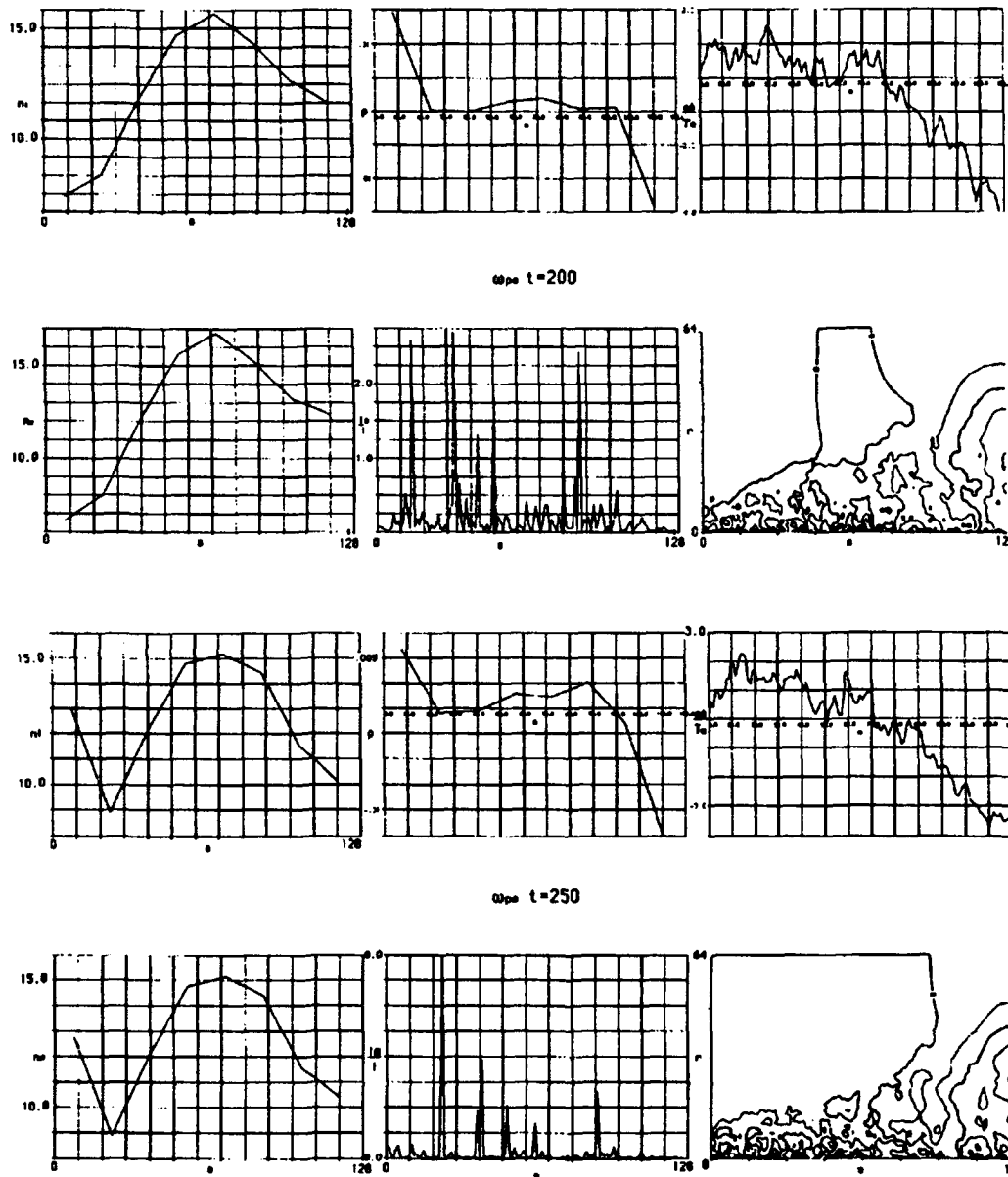


Figure 6.4: Plotted in this figure are the particle densities (at left), relative charge number (top center), and scale length (bottom center). The right set of plots portray the potential along the axis and radially by axial position.

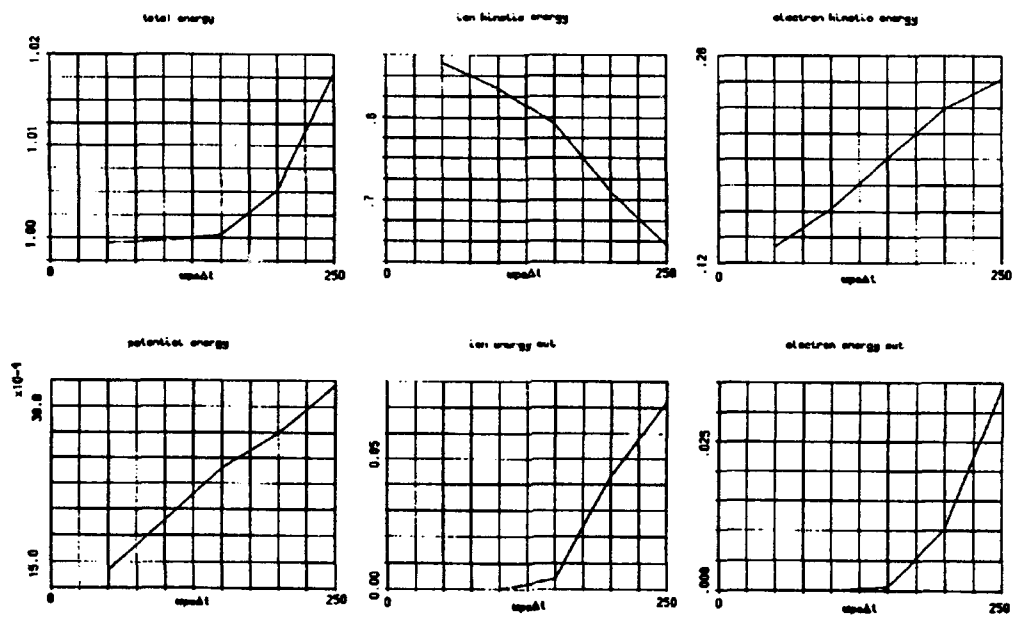


Figure 6.5: These plots show the same energies for the 2D case as for the similar plots in 1D (Figure 5.8).

Chapter 7

Conclusion

Our dissertation goal was to investigate the detailed spatial and temporal behaviour of potentials in the scenario of Serizawa and Sato [42]. We obtained analytic confirmation of their semi-empirical result that global large scale potentials may exist for plasmas injected into a dipole magnetic field. The potential is proportional to the kinetic energy of the injected ions, as given by equation (4.6). However, our analyses in Section 4.3 further suggest that local double layer solutions are to be expected in the parameter regimes considered. These expectations were verified by particle simulation in one and two dimensions and the results are described in Chapters 5 and 6.

We were led to our analytic results in search of a simple computational model. We therefore investigated analytic properties of increasingly more realistic particle distributions. In a cold drifting plasma the current and density are locked together by equation (4.4) so that the global and local solutions are inextricably linked. Thus, in Section 4.1 we demonstrated that, although a large scale potential, equation (4.2), exists, it neither permits local double layer solutions nor guarantees acceleration of incident particles.

With perpendicular and parallel temperatures, global potentials, Eqn. (4.6), retain the same functional dependence on ion kinetic energy ($\sim K_i$) as for the cold case, and maps of their relative charge densities exhibit remarkably constant properties. However, some distributions lead to local double layer solutions, others do not. In sections 4.2 and 4.3 we demonstrated that the local double layer solutions are provided opportunity by

the Maxwellian plasmas and cold (parallel) ions. Local analyses indicated this in section 4.3.2 and Figure 4.6.

The analytic results can be couched in terms of global and local requirements for charge neutrality. Global neutrality is guaranteed by equal exit currents into the loss cone while demands of local neutrality may lead to double layers. The conditions for a double layer are indicated by multi-valued solutions to the quasi-neutral equation (3.6). These solutions are present only when the slopes of underlying velocity distributions permit (as allowed by Bohm's criteria discussed in Section 3.4.1) and the momentum balance of particles rebounding or accelerating in the potential is maintained (Langmuir's condition.) Equivalently, Langmuir's condition, equation (3.9), may be interpreted graphically as areas of equal charge densities integrated over the double layer potential (Section 5.4.2.)

Indeed Bohm criteria and Langmuir's condition are just as operative as ever. All the theory of Chapter 3 is consistent. In section 3.4 we showed that the Bohm criteria were equivalent to conditions on the charge density. In section 3.6 we related these conditions to treatment of currentless double layers. However, the Bohm criteria are necessary but not sufficient to guarantee a solution. While the frame of the double layer is important, the real requirement is on particle distributions, not average quantities such as injection velocity.

To explore the temporal behaviour of our analytic results, in Chapters 5 and 6 we simulated a drifting plasma incident upon a dipole magnetic field in one and two dimensions. While previous double layer simulations modeled constant magnetic fields and fixed potentials [43], to our knowledge this is the first simulation of DL formation combining particle injection, floating potentials, and realistic magnetic fields. In the one dimensional simulations, a double layer of several kT with scale length $l \sim \lambda_D \ll R$, the magnetic field scale length, is clearly apparent in Figure 5.6.

As discussed in section 5.4.3 and shown in Figure 5.10, our simulation results compare well with analytic predictions [42], and correspond qualitatively with laboratory experiments [44], theory, and simulations examining the role of plasma jets into the earth's polar regions [42] and agree in magnitude with their predictions. In contrast, previous theory [52] and simulations [14] predicted an electric field $E \propto \frac{dB}{ds}$ ($l \sim R$.) These, however, assumed self-consistent distributions of particles in quasineutral electrostatic fields, thereby ignoring those portions of solution space reserved for

double layers. Our results bear out Stern's more general approach[45] of treating the double layer as an extension of quasineutrality but on a coarser (than λ_D) scale.

Our simulations have proven valuable in considering access to double layer solutions which match the required global potential[42]. While theory shows that double layers may form with self-consistent particle distributions, consideration of overall charge neutrality demands that the total potential drop across the model boundaries be constrained to a particular value. Local and global solutions need not match. Adjudication of any difference between these opposing potentials obeys the spatially dependent solution of Poisson's Equation coupled to the particles' distributions throughout the simulation region. While the global condition depends on the presence of particles in the loss cone, the double layer solution ultimately depends on local conditions. In our simulations differences between the boundary solution required for global charge neutrality and the local solution for the potential resulted in a sheath at the exit boundary.

Potential and particle distributions must be self-consistent in time. Perkins and Sun [35] analyzed the instability criteria for distributions such as ours. As expected, both ion and electron beams are subject to streaming instabilities. The instabilities, evident in temperature and velocity space plots of Figures 5.1-5.5, are consistent with the ion acoustic instability (with both electron beams) in one dimension. At first, the electrons rapidly thermalize while the ions remain cold. The waves scatter the ions in velocity space. Coincident with this scattering, the double layer moves to the low field side. The double layer approaches and rests near the boundary ($z=L$).

In consonance with [35] and suggested by [6], the frame of the double layer is important. When stability is reached the final distributions must be consistent with the final potential, and instabilities affect both. The role of instabilities is to alter particle distributions, and this requires the double layer to move. In section 5.4 we explained the movement in terms of momentum conservation, or Langmuir's condition, versus Block's description in electrical terms. Momentum conservation demands that the double layer adjust itself to where a local solution exists. The momentum lost is attributed to waves, in analogy with quasilinear theory [26]. Unlike ours Stenzel et al' double layers were stationary[44]. However, they attributed this property to a species of trapped electrons characteristic of their experiment.

The theory we have reviewed is essentially 1D but requires considerations of a second dimension. The two dimensional code has been successfully employed, but 2D results remain quite preliminary. It shares the same global behaviour but not all details of the local behaviour of the 1D results. In particular the 2D results lead to smaller magnitude double layers, and their movement is not apparent. Because our 2D diagnostics were not as extensive as in one dimension, we are unable at this time to verify the role of electrostatic ion cyclotron waves. However, the code should see future utility in more fully observing the effect of the extra degree of freedom. For example, in two dimensions it may be useful to model off-axis behaviour for our scenario or to model other scenarios such as that of Perkins and Sun. We discuss below.

Our B field provided an adjustable parameter called for by [35]. However, we modeled a sudden entrance of plasma into a region to simulate behaviour during a substorm. In our scenario we observe a rapid injection with few bounce times. The distributions are dominated by injected particles. Other situations may allow many bounce times, such as when particles are injected into a magnetic mirror [15]. In this model both ions and electrons are Maxwellian, because the ions have time to explore adjacent cells where collisions predominate. In our model instabilities we observe play a similar role. Given more than a few bounce times or increased collision frequency and sufficient confinement time, we expect to similarly populate our model, in which case an equilibrium with stationary double layers should be reached [35], [15]. Under these conditions a particle undergoing many bounces will lose memory of its injection velocity. Ultimately, however, the Langmuir's condition must be satisfied, requiring the double layer to adjust to some stationary equilibrium.

Longer simulation runs may be needed to explore the full behaviour of the double layers such as these. In that regard, usefulness of a guiding center pusher, developed in Appendix A, was demonstrated. Even in two dimensions it requires no corrector for stability. However, a more rigorous implementation of the guiding center approximation would be most useful for considering perpendicular phenomena in the E,B plane.

Simulations depending on Fourier transforms to solve for the potential [17] may be plagued by errors in the field calculation. In our 1D simulations these errors were traced to aliasing in a bounded plasma. In Appendix B a correction for aliasing has been derived to ameliorate its effects, and

this correction was successfully employed in one dimension. Our approach suggests an “optimal” particle shape based on two-body correlations to account for collisions. In Appendix C we developed Buneman’s algorithm for the mixed boundary conditions of our bounded 2D simulation.

In our simulations we used a simple injection scheme to avoid “energy instabilities.” This is analogous to and suffers from the same problems as “quiet starts” [5] to distribute particles in angles. It proved adequate for the 1D results. However, random injection with varying velocities (and densities) of particles would be more realistic and still avoid some of the cautions for steady injection.

Ideally, if charge neutrality is to be observed throughout the simulation region, $\int ds(\frac{\partial E}{\partial t} = -J) = 0$ at the boundaries. Writing this law in terms of the total charge entering a flux tube originating at the earth, we must have $\int J_{\parallel} \cdot dA_{end} = -\int J_{\perp} \cdot dA_{sides}$. The influx of current into the magnetic field flux tubes must be balanced by that across the magnetic field. If there is to be a net current out of the simulation, then, to be totally self-consistent, one needs to treat it as part of a circuit as did Sato and Okuda [37]. For discussion see Reference [43].

Finally, the role of background plasma in, for example, adjudicating the potential difference between local and global conditions has yet to be fully explored. Its role was discussed to some extent in section 5.2.3. Such techniques are worthy of future consideration.

Appendix A

Particle Pushers

A.1 The “Leap Frog” Scheme

A non-relativistic charged particle in external electric and magnetic fields obeys the Lorentz force law

$$\vec{F} = m \frac{d\vec{v}}{dt} = q(\vec{E} + \frac{\vec{v} \times \vec{B}}{c}) \quad (3.3)$$

[24, p.572]. To advance particles with discrete time steps (Δt), we seek a difference equation analog to (3.3) together with the similar expression for the velocity, $\frac{d\vec{x}}{dt} = \vec{v}$, which accurately models particle trajectories and is also stable to small deviations (due to round-off error, etc.) from the correct solution.

A MacLaurin expansion of (3.3) gives to lowest order in Δt

$$\vec{v}_{\frac{1}{2}} - \vec{v}_{-\frac{1}{2}} = \frac{q\Delta t}{m} \left[\vec{E}_0 + \left(\frac{\vec{v}_{\frac{1}{2}} + \vec{v}_{-\frac{1}{2}}}{2} \right) \times \frac{\vec{B}_0}{c} \right] + o(\Delta t^2) \quad (A.1)$$

This equation along with its position counterpart,

$$\frac{\vec{x}_1 - \vec{x}_0}{\Delta t} = \vec{v}_{\frac{1}{2}},$$

is known as the “Leap-Frog” scheme. Its name derives from alternate determination of velocities and functions of position, as pictured in Fig. A.1. We shall note that this time-centered scheme provides accuracy and favorable stability properties.

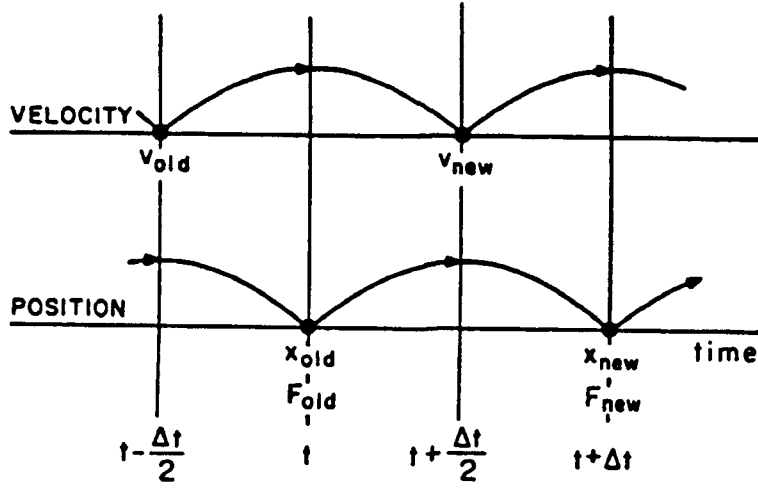


Figure A.1: Pictured here is the Leapfrog scheme in which velocities and functions of position are determined at interleaved time steps. (After [5, Fig. 2-4a, p.13].)

When \vec{E} and \vec{B} fields are constant, we may obtain the solution to (3.3) by substituting $\vec{v} = \vec{u} + \vec{w}_E$ where $\vec{w}_E = c \frac{\vec{E} \times \vec{B}}{B^2}$, leaving

$$\frac{d\vec{u}}{dt} = \frac{q}{m} \left[\frac{(\vec{u} \times \vec{B})}{c} + \vec{E}_{\parallel} \right],$$

where $\vec{E}_{\parallel} = \vec{E} \cdot \vec{B} / Bb$. Setting $\vec{\Omega} = \frac{q\vec{B}}{c}$ and operating on both sides with $\times \vec{\Omega}$ gives $\frac{d^2 \vec{u}_{\perp}}{dt^2} = -\Omega^2 \vec{u}_{\perp}$ where $\vec{u}_{\perp} \equiv \vec{u} - \vec{u}_{\parallel}$ and $\vec{u}_{\parallel} \equiv \vec{u} \cdot \vec{B} / Bb$. Using the initial conditions, $u_{20} \equiv u_2(0) = 0$ and $u_{30} \equiv u_3(0) = u_{\perp 0}$, the continuous solution for the perpendicular velocity is $\vec{u}_{\perp} = u_{\perp 0} [\cos \Omega t \hat{3} - \sin \Omega t \hat{2}]$.

The solution to (A.1) is obtained in a similar fashion. To lowest order,

$$\frac{\vec{u}_{\frac{1}{2}} - \vec{u}_{-\frac{1}{2}}}{\Delta t} = \frac{\vec{u}_{\frac{1}{2}} + \vec{u}_{-\frac{1}{2}}}{2} \times \vec{\Omega}_0 + \vec{E}_{\parallel 0}$$

Multiplying each side by Δt and adding $2\vec{u}_{-\frac{1}{2}}$ yield

$$\begin{aligned} \vec{u}_{\frac{1}{2}} + \vec{u}_{-\frac{1}{2}} &= \frac{\vec{u}_{\frac{1}{2}} + \vec{u}_{-\frac{1}{2}}}{2} \times \vec{\Omega}_0 \Delta t + 2\vec{u}_{-\frac{1}{2}} + \vec{E}_{\parallel 0} \Delta t \\ &= -[\vec{u}_{\frac{1}{2}} + \vec{u}_{-\frac{1}{2}}]_{\perp} \alpha^2 + \vec{u}_{-\frac{1}{2}} \times \vec{\alpha} + 2\vec{u}_{-\frac{1}{2}} + \vec{E}_{\parallel 0} \Delta t \\ \vec{u}_{\frac{1}{2}} &= \frac{1 - \alpha^2}{1 + \alpha^2} \vec{u}_{\perp - \frac{1}{2}} + \vec{u}_{-\frac{1}{2}} \times \frac{2\alpha}{1 + \alpha^2} \hat{\alpha} + \vec{u}_{\parallel - \frac{1}{2}} + \vec{E}_{\parallel 0} \Delta t \end{aligned}$$

where $\vec{\alpha} \equiv \frac{\vec{\Omega}_0 \Delta t}{2}$.

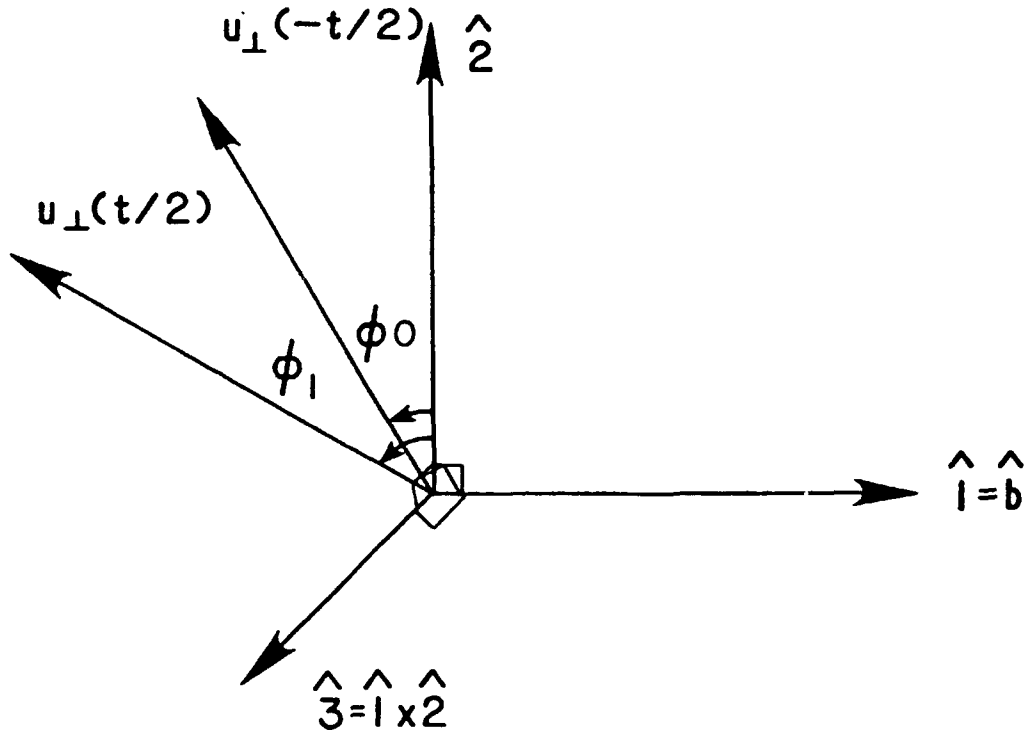


Figure A.2: This is the magnetic coordinate system.

Separating this (vector) equation into its three scalar components according to the coordinate system defined in Figure A.2,

$$\begin{aligned} u_{1\frac{1}{2}} &= u_{1-\frac{1}{2}} + E_{1_0}\Delta t \\ u_{2\frac{1}{2}} &= f_1 u_{2-\frac{1}{2}} + f_2 u_{3-\frac{1}{2}} \\ u_{3\frac{1}{2}} &= f_1 u_{3-\frac{1}{2}} - f_2 u_{2-\frac{1}{2}}, \end{aligned}$$

where $f_1 = \frac{1-\alpha^2}{1+\alpha^2}$ and $f_2 = \frac{2\alpha}{1+\alpha^2}$. The last two equations may be most conveniently expressed as $\vec{u}_{\perp\frac{1}{2}} = \vec{R} \cdot \vec{u}_{\perp-\frac{1}{2}}$ where \vec{R} is the tensor

$$\vec{R} = \begin{bmatrix} f_1 & f_2 \\ -f_2 & f_1 \end{bmatrix}$$

We note that the determinant $|\vec{R}| = f_1^2 + f_2^2 = \left(\frac{1-\alpha^2}{1+\alpha^2}\right)^2 + \left(\frac{2\alpha}{1+\alpha^2}\right)^2 = 1$ so the operator \vec{R} is a pure rotation in the plane perpendicular to \vec{B} . This means that the magnitude of the velocity component perpendicular to \vec{B} is conserved.

Because our particle maintains its perpendicular velocity in constant E and uniform B fields, its guiding center moves at the correct velocity,

$\vec{v}_{gc} = v_{\parallel}\hat{e}_1 + \vec{w}_E$, and along its correct path. However, corrections must be introduced to maintain the trajectory for the particle. Using half-angle formulas for the sine and cosine [41], after one time step the continuous phase angle is $\Omega\Delta t = \tan^{-1}\left(\frac{2\tan\frac{\Omega\Delta t}{2}}{1-\tan^2\frac{\Omega\Delta t}{2}}\right)$. However, since

$$\begin{aligned} u_{21} &= \frac{2\alpha}{1+\alpha^2}u_0 \\ u_{31} &= \frac{1-\alpha^2}{1+\alpha^2}u_0, \end{aligned}$$

the discrete phase angle is $\tan^{-1}\left(-\frac{u_2}{u_3}\right) = \tan^{-1}\left(\frac{-2\alpha}{1-\alpha^2}\right)$. While equal in the limit $\Delta t \rightarrow 0$, only $\alpha \equiv \tan\alpha$ maintains the same phase for all Δt .

Similarly, for \vec{u}_{\perp} to represent the correct particle orbit, we must equate the difference equation

$$\frac{\vec{\rho}_1 - \vec{\rho}_0}{\Delta t} = \vec{u}_{\frac{1}{2}}$$

to

$$\frac{d\vec{\rho}}{dt} = \vec{u}$$

where here $\vec{\rho}$ is the Larmor radius. Using the known solution for the correct particle position, $\vec{\rho} = \rho(0)(\cos\Omega t\hat{2} + \sin\Omega t\hat{3})$, the discrete solution is

$$\vec{\rho}(\Delta t) - \vec{\rho}(0) = \vec{u}_{\frac{1}{2}}\Delta t = \Omega\rho_0\left[-\sin\frac{\Omega\Delta t}{2}\hat{2} + \cos\frac{\Omega\Delta t}{2}\hat{3}\right]\Delta t$$

giving the particle position after one time step as

$$\rho_2(\Delta t) = \rho_0 - \rho_0 \sin\left(\frac{\Omega\Delta t}{2}\right)\Omega\Delta t$$

$$\rho_3(\Delta t) = \rho_0 \cos\left(\frac{\Omega\Delta t}{2}\right)\Omega\Delta t$$

with Larmor radius

$$\rho_1 = \sqrt{\rho_{21}^2 + \rho_{31}^2} = \rho_0\left[1 + 4\alpha^2\left(1 - \frac{\sin\alpha}{\alpha}\right)\right]^{\frac{1}{2}}$$

This agrees with the continuous solution only for $\sin\alpha = \alpha$.

Recognizing that, in general, the solution to the difference equation does not match the physical solution, we may introduce coefficients, $\lambda(\Delta t)$,

into the difference equations to obtain identical continuous and discrete trajectories for all Δt while the difference and continuous equations are the same in the limit of small time steps, $\lim_{\Delta t \rightarrow 0} \lambda = 1$. Defining $\lambda_\rho = \frac{\sin \alpha}{\alpha}$ and $\lambda_\Omega = \frac{\tan \alpha}{\alpha}$, we have

$$\begin{aligned} \frac{\vec{x}_1 - \vec{x}_0}{\Delta t} &= \lambda_{\rho \frac{1}{2}} \vec{u}_{\perp \frac{1}{2}} + \vec{w}_{E \frac{1}{2}} + \vec{v}_{\parallel \frac{1}{2}} \\ \left(\frac{\vec{v}_{\frac{1}{2}} - \vec{v}_{-\frac{1}{2}}}{\Delta t} \right) &= \frac{q}{m} [\vec{E}_{0\parallel} + \lambda_{\Omega 0} (\vec{E}_{0\perp} + \frac{\langle \vec{v}_0 \rangle \times \vec{B}_0}{c})] \end{aligned} \quad (\text{A.2})$$

where $\langle \vec{v}_0 \rangle \equiv \frac{\vec{v}_{\frac{1}{2}} + \vec{v}_{-\frac{1}{2}}}{2}$. A particularly efficient implementation of this scheme breaks the equation for the velocity into an acceleration by the electric field and a pure rotation by the magnetic field, and is known as the Boris algorithm [8].

Accuracy

This scheme was derived for constant \vec{E} and \vec{B} and is the correct solution for the first RHS term in (A.1). Setting $\vec{x} = \vec{x}_0 + \Delta \vec{x} + \vec{\epsilon}$, we obtain the error after one time step.

$$\begin{aligned} \vec{x}_{\pm \frac{1}{2}} - \vec{x}_0 &= \int_0^{\pm \frac{1}{2} \Delta t} dt \vec{v} \\ \Delta \vec{x} &= \vec{v}_0 \Delta t \\ \vec{\epsilon} &= \int \vec{v} dt - \Delta \vec{x} \\ &\sim \left(\frac{d\vec{a}}{dt} \Big|_0 \right) \frac{\Delta t^3}{24} \end{aligned}$$

Stability

For simplicity consider (A.2) only for constant \vec{B} and one-dimensional $\vec{E} = E_{\parallel}(s)\hat{b}$. Setting $\vec{x}_n = \vec{x}_{n0} + \delta \vec{x}_n$, the difference equation for the error, $\delta \vec{x}$, in the parallel direction is

$$\begin{aligned} \delta(\vec{x}_1 - 2\vec{x}_0 + \vec{x}_{-1}) &= (\delta \vec{x}_0 \cdot \vec{\nabla}) \frac{q \vec{E} \Delta t^2}{m} \\ &= \left(\frac{q}{m} \nabla \cdot \vec{E} \Delta t^2 \right) \delta \vec{x}_0 \end{aligned}$$

$$= \frac{-4\pi\delta n\epsilon^2\Delta t^2}{m}\delta\vec{x}_0$$

The maximum $\delta\vec{E}$ occurs for $\sum_{i=1}^N\delta\vec{x}_{i0} = N\delta\vec{x}_0$ or $\delta n = n_0$. This is equivalent to displacing all the particles together. We may obtain a dispersion relation for this scheme by (z) transforming to $\delta x_n = \delta x_0 e^{in\omega\Delta t}$ [21, page 664],

$$\begin{aligned} e^{i\omega\Delta t} - 2 + e^{-i\omega\Delta t} &= -(\omega_{pe}\Delta t)^2 \\ -4\sin^2\omega\Delta t/2 &= \end{aligned}$$

requiring $\omega_{pe}\Delta t < 2$ for stability to parallel displacements. A more careful analysis reveals that the actual stability requirement is $\omega_{pe}\Delta t < 1.62$ [5, p. 184].

A.2 Gyrokinetic Solution

A similar analysis shows perpendicular displacements to be stable. However, the full dispersion relation includes non-physical effects from aliasing in frequency which causes instabilities analogous to cyclotron waves [5, p. 201]. In general, aliasing can be reduced by choosing smaller values of $\Omega\Delta t$ [5, p.202-203]. Thus, in particle pushing schemes including gyromotion the time step is limited by the time to complete a gyrorbit. It is desirable to use a scheme which eliminates this stability restriction.

Such a scheme results from an (analytic) averaging over particle orbits. When we average the single particle equation of motion over the gyromotion, to order $\epsilon \sim \frac{m}{q} \sim \frac{\omega}{\Omega} \sim \rho/L$ (with $L \equiv |B/\nabla B|$ [31]),

$$\ddot{\vec{R}} = \frac{e}{m}[\vec{E}(R) + (\dot{\vec{R}}/c) \times \vec{B}(R)] - \left(\frac{\mu}{m}\right)\nabla\vec{B}(R) + o(\epsilon)$$

[32, eqn (12),p. 84] where $\mu \equiv \frac{mv_{\perp}^2}{2B}$. This equation is as difficult to solve as the original equation and carries unphysical properties with it [32]. A substitute for this equation is the coupled set, to $o(\epsilon^2)$,

$$\frac{dv_{\parallel}}{dt} = \frac{e}{m}E_{\parallel} - \mu\frac{\partial B}{\partial s} + \vec{u}_E \cdot \left(\frac{\partial\hat{e}_1}{\partial t} + v_{\parallel}\frac{\partial\hat{e}_1}{\partial s} + \vec{u}_E \cdot \nabla\hat{e}_1\right)$$

and

$$\dot{\vec{R}}_{\perp} = \frac{\hat{e}_1}{\Omega} \times \left[-\frac{e}{m} \vec{E} + \frac{\mu}{m} \vec{\nabla} B + (v_{\parallel} \frac{d\hat{e}_1}{dt} + \frac{d\vec{u}_E}{dt}) \right]$$

[32, eqn (17),(20)] In our model B is stationary and both \vec{E} and \vec{B} are in the $\hat{\rho}, \hat{z}$ plane so that $\vec{u}_E = u_E \hat{\phi}$. Invoking azimuthal symmetry ($\frac{\partial}{\partial \phi} = 0$) the parallel equation reduces to

$$\frac{dv_{\parallel}}{dt} = \frac{eE_{\parallel}}{m} - \frac{\mu}{m} \frac{\partial B}{\partial s} + \vec{u}_E \cdot (\vec{u}_E \cdot \vec{\nabla}) \hat{b}$$

and

$$\begin{aligned} \dot{\vec{R}}_{\perp} = & \left[-c \frac{E_{\perp}}{B} + \frac{\mu(\vec{\nabla} B)_{\perp}}{m\Omega} + \frac{v_{\parallel}^2}{\Omega} \left(\frac{\partial \hat{b}}{\partial s} \right)_{\perp} + \frac{v_{\parallel}}{\Omega} \left(\frac{\partial \vec{u}_E}{\partial s} \right)_{\perp} - \frac{b_z}{\Omega \rho} u_E^2 \right] \hat{\phi} \\ & + \left(\frac{1}{\Omega} \frac{\partial u_E}{\partial t} + \frac{u_E b_{\rho} v_{\parallel}}{\rho \Omega} \right) (\hat{b} \times \hat{\phi}) \end{aligned}$$

where \perp denotes the direction $\hat{\phi} \times \hat{b}$. All except the last two terms in $\dot{\vec{R}}_{\perp}$ are in the $\hat{\phi}$ direction. In general, these equations are not amenable to time-centering.

Formally these equations were derived for $\vec{E}_{\parallel} \sim \epsilon$, $\vec{E}_{\perp} \sim 1$. In some instances the additional assumption that $E_{\perp} \sim E_{\parallel}$ holds and the last terms and others involving \vec{u}_E may be ignored. In our simulation we assume instead $\frac{\partial}{\partial t} \sim \omega \ll \Omega$, [$\omega(\frac{\mu}{\Omega}) \sim \epsilon^2$], where ω is the time scale for large field changes so that the first of these terms may be ignored. Additionally, for weak curvature the second term is on the order of $\rho/r \sim \epsilon$ in comparison to other terms in the perpendicular velocity.

Writing the velocity in cylindrical coordinates, we have

$$\vec{v} = r\dot{\hat{r}} + r\dot{\phi}\hat{\phi} + z\dot{\hat{z}}$$

and the parallel and perpendicular velocities separate into their components

$$\begin{aligned} \vec{v}_{\parallel} &= r\dot{\hat{r}} + z\dot{\hat{z}} \\ \vec{v}_{\perp} &= r\dot{\phi}\hat{\phi} = \vec{v}_d + \frac{q}{m} \frac{\langle \vec{E} \rangle \times \hat{b}}{\Omega} \end{aligned}$$

where $\vec{v}_d = \left[\frac{\mu(\vec{\nabla} B)_{\perp}}{m\Omega} + \frac{v_{\parallel}^2}{\Omega} \left(\frac{\partial \hat{b}}{\partial s} \right)_{\perp} + \frac{v_{\parallel}}{\Omega} \left(\frac{\partial \vec{u}_E}{\partial s} \right)_{\perp} - \frac{b_z}{\Omega \rho} u_E^2 \right] \hat{\phi}$ is the ϕ component of the perpendicular velocity less the $\vec{E} \times \vec{B}$ drift.

Differentiating the parallel velocity

$$\begin{aligned}
\frac{d\vec{v}_{\parallel}}{dt} &= \frac{d(v_{\parallel}\hat{b})}{dt} = \frac{dv_{\parallel}}{dt}\hat{b} + v_{\parallel}\frac{d\hat{b}}{dt} = \ddot{r}\hat{r} + \ddot{z}\hat{z} + \dot{r}\dot{\hat{r}} + \dot{z}\dot{\hat{z}} \\
\frac{d\hat{b}}{dt} &= \frac{d}{dt}(b_r\hat{r} + b_z\hat{z}) = \dot{b}_r\hat{r} + b_r\dot{\hat{r}} + \dot{b}_z\hat{z} + b_z\dot{\hat{z}} \\
\ddot{r}\hat{r} + \ddot{z}\hat{z} &= \frac{dv_{\parallel}}{dt}\hat{b} + v_{\parallel}(\dot{b}_r\hat{r} + \dot{b}_z\hat{z}) \\
\frac{\dot{r}_{\frac{1}{2}} - \dot{r}_{-\frac{1}{2}}}{\Delta t}\hat{r} + \frac{\dot{z}_{\frac{1}{2}} - \dot{z}_{-\frac{1}{2}}}{\Delta t}\hat{z} &= \frac{dv_{\parallel}}{dt}\hat{b} + v_{\parallel}^2\left(\frac{\partial b_r}{\partial s}\hat{r} + \frac{\partial b_z}{\partial s}\hat{z}\right) \\
&= \frac{dv_{\parallel}}{dt}\hat{b} + [3v_{\parallel}^2\frac{(1 + \cos^2\theta)b_{\theta}}{r(1 + 3\cos^2\theta)}(\hat{b} \times \hat{\phi})]_0 \quad (\text{A.3})
\end{aligned}$$

where we have used $\vec{v}_{\parallel} \cdot \hat{z} = v_{\parallel}, \hat{b}_z = \hat{z}$. We observe that the above equation consists of an acceleration and a pure rotation so that we may apply the Boris algorithm with $\vec{v}_{\perp} \rightarrow v_{\parallel}$ and $\Omega \rightarrow 3v_{\parallel}^2(1 + \cos^2\theta)b_{\theta}/r(1 + 3\cos^2\theta)$.

Appendix B

Poisson Solvers

B.1 Charge Aggregation and Force Interpolation

B.1.1 Pairwise Force Calculation

The most obvious way to calculate the force on a particle is to calculate the force from the local B field and the resultant pairwise electric field. Naively this method involves $O(n^2) \sim \frac{n(n-1)}{2}$ calculations for n particles. In one dimension the number of calculations may be reduced to $\sim n \log n$ by particle sorting. In higher dimensions we are unable to use this technique, and even in 1D the number of calculations may be prohibitive.

B.1.2 E Field Grid

At the expense of some loss in precision an alternate route may be taken. A grid may be superimposed upon the model, then charges are assigned to and Poisson's equation is solved at each grid point[23]. Besides avoiding computation of pairwise forces, the grid facilitates study of field behaviour in space and time and smooths collisions among the limited number of particles.

B.1.3 Direct Integration

Once we know the electric field at grid points, we must calculate the force on particles between points. We could interpolate, using a Taylor series expansion. An equivalent approach in one dimension, with strong physical appeal, is direct integration.

$$\int_{x_g}^x dx (\nabla \cdot \vec{E}) = E(x) - E_g = 4\pi \int_{x_g}^x \rho dx$$

Similarly $E_{g+1} - E_g = 4\pi \int_{x_g}^{x_{g+1}} \rho dx \equiv 4\pi \langle \rho \rangle \Delta$

or $E(x) = E_g + (E_{g+1} - E_g)\delta - 4\pi \int_{x_g}^x (\langle \rho \rangle - \rho) dx$

$$= \delta E_{g+1} + (1 - \delta)E_g + o(\Delta^2)$$

where $\delta \equiv \frac{(x-x_g)}{\Delta}$ and $\langle \dots \rangle$ denotes the average. Thus the particle force is

$$F(x) = q[\delta E_{g+1} + (1 - \delta)E_g]$$

While it is possible to mix schemes for charge sharing and force calculation, due to the reciprocal nature of fields and density, use of a single scheme for both prevents unphysical self forces from arising [5, p.162-3].

B.2 Electric Field Calculation

B.2.1 Difference Equations

In the 1D case we may integrate Poisson's equation (3.1(a)), suitably interpolating ρ between grid points. This approach is equivalent to a finite difference solution,

$$E_g - E_{g+1} = \rho_{g+\frac{1}{2}} \Delta x + o(\Delta x^2),$$

where we have used the difference analog to the operator $\frac{dA}{dx}$, $A_{g+\frac{1}{2}} - A_{g-\frac{1}{2}}$, A a quantity defined at the grid point g .

In the 1D electrostatic case Poisson's Equation (3.1(a)) becomes

$$\phi_{g+1} - 2\phi_g + \phi_{g-1} = -4\pi\rho_g\Delta^2$$

We may obtain the solution for ϕ_g after inverting the resulting tridiagonal equation. The Buneman algorithm, as presented in Appendix C, is a particularly efficient application of this scheme in more than one dimension.

B.2.2 Fourier Transform Solution

Discrete Fourier Transforms

Solution of Poisson's equation can be obtained by using discrete Fourier transforms, just as one would use Fourier transforms in the continuous sense. The discrete Fourier transform of (B.4) on the interval $x = 0, L$, with grid points at $x_g = g\Delta + x_0, g = 0, 1, 2, \dots, N$, is obtained from the continuous (finite) transform as

$$\begin{aligned}\rho_k &= \int_0^L dx' \rho(x') e^{-ikx'} \\ &= \sum_g q_g \int_0^L dx' \delta(x' - x_g) e^{-ikx'} \\ &= \Delta \sum_g \rho_g e^{-ikx_g}\end{aligned}$$

The inverse is found by noting that

$$\sum_{k=\frac{2\pi}{L}}^{\frac{2\pi}{L}} e^{ik(x_g - x_{g'})} = \begin{cases} N & g = g' + lN \\ 0 & g \neq g' + lN, \end{cases}$$

l an integer, so that $\rho_g = \frac{1}{N\Delta} \sum_k \rho_k e^{ikx_g}$, where k takes on the values $m\Delta k$, $m = 1, 2, \dots, N$ and $\Delta k = \frac{2\pi}{L}$.

To solve a linear equation such as Poisson's, we apply the operator $\Delta \sum_g e^{-ikx_g}$, obtaining the k-space solution as

$$\begin{aligned}\mathcal{L}g &= f \\ g_k &= \mathcal{L}_k^{-1} f_k\end{aligned}$$

We then apply the inverse transform to obtain g . On its face this procedure appears to require $\sim N^2$ operations ($\sim N$ summations for each $k \times N$ ks.) However, the Fast Fourier Transform (FFT), has decreased that number to $\sim N \log N$, a huge savings[16]. We shall write the FFT algorithm as

$$FFT(A) = \sum_n A_n e^{-\frac{2\pi i mn}{N}} \quad n, m \text{ discrete}$$

We are able to compute the transform of quantities defined at points displaced from the grid by including a phase factor:

$$\begin{aligned}
\sum_g e^{-ikx_g} A_g &= \sum_g e^{-ik(g\Delta+\delta)} A_g \quad x = g\Delta + \delta \\
&= \sum_g (A_g e^{-ik\delta}) e^{-\frac{2\pi ikg}{N}} \\
&= FFT(A_g e^{-ik\delta}) \\
A_k &= e^{-ik\delta} FFT(A_g)
\end{aligned}$$

Similarly, the phase factor must be included when we find the inverse transform

$$\frac{1}{N} \sum_k e^{ikx} [e^{-ik\delta} FFT(A_g)] = A(x)$$

These notions are useful when examining charge sharing and interpolation schemes, but for grid quantities where $x=x_g = g'\Delta + \delta$, we have

$$A(x_g) = \sum_k e^{\frac{2\pi ikm}{N}} FFT(A_g) = FFT^{-1}[FFT(A_g)]$$

and the phase factor is unneeded.

1D Green's Function Solution to Poisson's Equation with Mixed boundary conditions

Continuous Solution We desire to solve the continuous Poisson's equation for E and use it as a basis for the discrete solution in our simulation. Thus, we seek the solution to the 1D boundary value problem:

$$-\nabla^2 \phi = 4\pi\rho, \quad \phi(0) = 0, \quad \phi'(l) = 0$$

The solution may be expressed in terms of a Green's function which satisfies the equation

$$\nabla'^2 G = -4\pi\delta(\vec{x} - \vec{x}')/A, \quad (\text{B.1})$$

with boundary conditions on G to be determined. Defining $g = \int_A G da'$, we multiply (B.1) by ϕ and integrate by parts to obtain

$$\phi(\vec{x}) = \int_V \rho(\vec{x}') G(\vec{x}, \vec{x}') d^3x' + \frac{1}{4\pi} \oint_S [G(\vec{x}, \vec{x}') \frac{\partial \phi}{\partial n'} - \phi(\vec{x}') \frac{\partial G(\vec{x}, \vec{x}')}{\partial n'}] da'$$

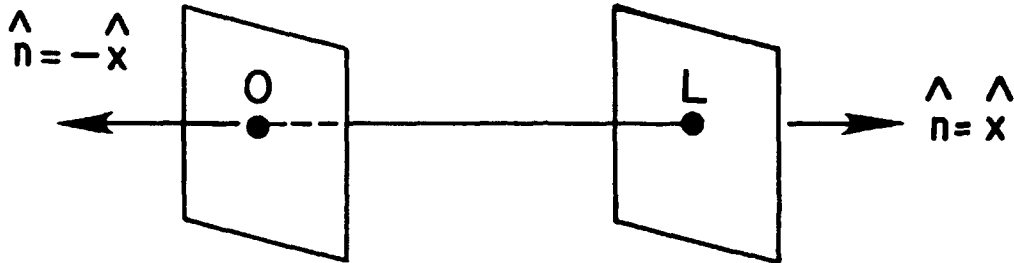


Figure B.1: This sketch shows the area of integration used in evaluating the Green's function solution to Poisson's equation.

$$= \int_0^L dx \rho(x)g + \frac{1}{4\pi} \left(g \frac{\partial \phi}{\partial x'} - \phi \frac{\partial g}{\partial x'} \right) \Big|_0^L [24, p.41]$$

At $x=0$ where $\phi = 0$ it is most convenient to remove the second term by requiring $G=0$. At $x=L$ where $\phi' = 0$ we can, at best, satisfy the boundary condition imposed by Poisson's Equation:

$$\int d^3 x' \nabla'^2 G = \oint \frac{\partial G}{\partial n'} da' \Big|_0^L = -4\pi$$

$$\frac{\partial g}{\partial x} \Big|_L - \frac{\partial g}{\partial x} \Big|_0 = -4\pi$$

This implies

$$\phi(\vec{x}) = \int_V \rho(x)G(x, x')d^3 x' + \phi(L) \left[1 - \frac{1}{4\pi} \frac{\partial G}{\partial x} \Big|_0 \right]$$

Evaluating this expression at $\vec{x} = 0$ with the boundary condition $G(0, x') = 0$ gives $\frac{\partial G}{\partial x} \Big|_0 = 4\pi$ or $\frac{\partial G}{\partial x} \Big|_L = 0$ just as for the potential ϕ .

We solve for G using an alternative Green's function,

$$E(x) = \int_0^L dx' d(x - x')\rho(x'),$$

where $d(x - x')$ is the solution to

$$\frac{d}{dx}(d) = 4\pi\delta(x - x')$$

and g and d are related by

$$d = \frac{dg}{dx}$$

Applying the condition, $E(L) = 0$,

$$\begin{aligned} d(L - x') - d(x - x') &= \int_x^L 4\pi\delta(x'' - x')dx'' \\ -d(x - x') &= \begin{cases} 0 & x > x' \\ 4\pi & x < x' \end{cases} \end{aligned}$$

After integrating and applying the condition, $\phi(0) = 0$,

$$\begin{aligned} g(x - x') - g(0 - x') &= -\int_0^x dx'' d(x'' - x') \\ &= \begin{cases} 4\pi x' & x > x' \\ 4\pi x & x < x' \end{cases} \end{aligned}$$

Discrete Solution Now we may solve for E. Making use of a continuous finite transform in x and a discrete transform in k, we have

$$\begin{aligned} E(x) &= \int_0^L dx' \left(\frac{1}{L} \sum_k d_k e_{ik(x-x')} \right) \left(\frac{1}{L} \sum_{k'} \rho_{k'} e^{ik'x'} \right) \\ &= \frac{1}{L^2} \sum_k d_k e^{ikx} \sum_{k'} \rho_{k'} \int_0^L e^{i(k'-k)x'} dx' \\ &= \frac{1}{L} \sum_k d_k \rho_k e^{ikx} \\ \text{or } E_k &= d_k \rho_k \end{aligned}$$

In other words, to solve for the electric field of some arbitrary charge distribution, we need only solve once for d_k and algebraically find the solution for the particular charge spectrum.

Proceeding to the solution for d_k , we begin by solving for the discrete ϕ .

$$\begin{aligned} \phi(x) &= \int_0^L dx' g(x - x') \rho(x') \\ &= \int_0^L dx' g(x - x') \left(\frac{1}{L} \sum_k \rho_k e^{ikx'} \right) \\ &= \frac{4\pi}{L} \left[\sum_{k \neq 0} \rho_k \left(\int_0^x dx' x' + \int_x^L dx' x \right) e^{ikx'} + \rho_0 \left(\int_0^x dx' x' + \int_x^L dx' x \right) \right] \end{aligned}$$

$$\begin{aligned}
&= \frac{4\pi}{L} \left\{ \sum_{k \neq 0} \rho_k \left(-i \frac{d}{dk} \int_0^x dx' + x \int_x^L dx' \right) e^{ikx'} + \rho_0 \left[\frac{1}{2} x'^2 \Big|_0^x + x(x') \Big|_x^L \right] \right\} \\
&= \frac{4\pi}{L} \left\{ \sum_{k \neq 0} \rho_k \left[-i \frac{d}{dk} \left(\frac{1}{ik} e^{ikx'} \right) \Big|_0^x + x \left(\frac{1}{ik} e^{ikx'} \right) \Big|_x^L \right] + \rho_0 \left[\frac{x^2}{2} + x(L-x) \right] \right\} \\
&= \frac{4\pi}{L} \left\{ \sum_{k \neq 0} \rho_k \left[-\frac{d}{dk} \left(\frac{1}{k} e^{ikx} - \frac{1}{k} \right) + \frac{x}{ik} (e^{ikL} - e^{ikx}) \right] + \rho_0 x \left(L - \frac{x}{2} \right) \right\} \\
&= \frac{4\pi}{L} \left\{ \sum_{k \neq 0} \rho_k \left[\left(\frac{1}{k^2} - \frac{ix}{k} \right) e^{ikx} - \frac{1}{k^2} - \frac{ix}{k} (1 - e^{ikx}) \right] + \rho_0 x \left(L - \frac{x}{2} \right) \right\} \\
&= \frac{4\pi}{L} \left[\sum_{k \neq 0} \frac{\rho_k}{k^2} (e^{ikx} - 1 - ikx) + \rho_0 x \left(L - \frac{x}{2} \right) \right]
\end{aligned}$$

$$E = -\nabla\phi = \frac{4\pi}{L} \left[\sum_{k \neq 0} -\frac{i\rho_k}{k} (e^{ikx} - 1) + \rho_0 (x - L) \right] \quad (B.2)$$

These, of course, may be recognized as a particular solution to the inhomogeneous equation (the periodic (in x) parts) and a general solution to the homogeneous equations (the parts non-periodic in x .)

An "Exact" Poisson Solver

In many instances use of the Fourier Transform solution is preferable to that of difference equations which results from approximating the operator $\frac{d}{dx}$ (or $\frac{d^2}{dx^2}$) when solving for ϕ . As its name implies, the FFT is relatively fast, particularly in multiple dimensions and unlike other fast solvers such as Buneman's, allows easy analysis of the field spectra, and incorporation of particle shaping. If we plan to use FFTs to solve these equations, however, we must be prepared to live with aliasing which result from inability to distinguish short wavelength modes from others on a finite grid. Indeed, we can readily show examples using Fourier Transforms where, despite the advertised (local) error estimates, global errors can be disastrous.

In the previous section we implicitly solved for $d_k = -\frac{4\pi i}{k}$ in equations B.1 and B.2. In general, however, the choice of the Poisson solver is somewhat arbitrary. Eastwood [19] makes a case for choosing the (periodic) solution to Poisson's equation as

$$\hat{E}_k = \hat{d}_k \hat{\rho}_k \quad (B.2')$$

where \hat{d}_k minimizes the mean-squared deviation of F , the resulting force, from R , a “reference” force. In our case the reference force is that defined by the particle shape and E field (B.2).

The optimal $\hat{d}_k = |\hat{U}_k|^2 = \hat{R}_k / |\sum_n \hat{U}_{kn}|^2$. Here \hat{R}_k is the Fourier transform of R (with the assumption that R is band limited), \hat{U}_k is the transform of the shape function U , and \hat{U}_{kn} is the alias of \hat{U}_k due to finite transforms. Basically \hat{d}_k is that from the Green’s function solution to the Poisson’s equation adjusted to account for particle shape/force weighting schemes and aliasing due to finite grids.

The assumption of a band-limited force is tenuous from the outset, and the proper choice of \hat{E}_k for non-periodic boundary conditions is difficult if not completely ambiguous. Thus, in many cases the direct k -space solution to Poisson’s equation (B.2) is likely to be as good as (or better) than other more sophisticated schemes [19, p.15].

Trying to retain the advantages of the FFT without loss of accuracy due to aliasing, we take a slightly different approach. Rather than approximate the operator and take the charge distribution as known exactly at points, we shall use the exact operator and approximate the charge distribution over the continuous interval about the known points, $x_g = g\Delta + \delta, g = 0, 1, 2 \dots$. We take as given, ρ_g , and expand the continuous function ρ about these values. Of course, if we know $\rho(x)$ everywhere, we could (conceivably) solve for E exactly.

In one dimension

$$\frac{\partial E}{\partial x} = 4\pi\rho(x) = 4\pi\left\{\left[\sum_g \rho(x_g) + \frac{\partial\rho}{\partial x}\Big|_{x=x_g}(x-x_g) + \frac{\partial^2\rho}{\partial x^2}\Big|_{x=x_g}\frac{(x-x_g)^2}{2} + \dots\right]\Pi_g\right\}$$

where x_g is a grid point, Δ the grid spacing, and

$$\Pi_g = \begin{cases} 1 & |x - x_g| < \frac{\Delta}{2} \\ 0 & |x - x_g| > \frac{\Delta}{2} \end{cases}$$

is the “hat” function. Further we may require that, if we find the value of ρ_g by “adding up” particle charges within each g th cell, $\sum_i \int_{g\Delta+\delta_i-\frac{\Delta}{2}}^{g\Delta+\delta_i+\frac{\Delta}{2}} \rho dx = \rho_g$. This effectively eliminates all even values of the expansion (except for the zeroth term.)

Now, to solve Poisson’s equation, we use Fourier transforms. However, we would like to avoid the problems of aliasing or, alternatively, problems of truncation associated with difference schemes.

Specifically, the FFT and continuous transforms for ρ can be shown to be related. Applying the operator $\int_0^L dx e^{-ikx} \dots$, we obtain the transform of the quantities.

$$\begin{aligned}\rho_k &= \int_0^L dx e^{-ikx} \Pi_g \left[\sum_g \rho_g + \frac{\partial \rho}{\partial x} \Big|_g (x - x_g) + \dots \right] \\ &= \sum_g \int_{x_g - \frac{\Delta}{2}}^{x_g + \frac{\Delta}{2}} dx \left[\rho_g + \frac{\partial \rho}{\partial x} \Big|_g (x - x_g) + \dots \right] e^{-ikx}\end{aligned}$$

We may evaluate the integral piece by piece for each cell, $x_g - \frac{\Delta}{2} < x < x_g + \frac{\Delta}{2}$, and, taking $\rho_g, \frac{\partial \rho}{\partial x} \Big|_g \dots$ as known grid quantities, we find

$$\begin{aligned}\int_{x_g - \frac{\Delta}{2}}^{x_g + \frac{\Delta}{2}} dx e^{-ikx} &= \frac{1}{-ik} [e^{-ik(x_g + \frac{\Delta}{2})} - e^{-ik(x_g - \frac{\Delta}{2})}] \\ &= \frac{i}{k} e^{-ikx_g} (e^{-i\frac{k\Delta}{2}} - e^{i\frac{k\Delta}{2}}) \\ &= \Delta e^{-ikx_g} \sin\left(\frac{k\Delta}{2}\right) / \left(\frac{k\Delta}{2}\right),\end{aligned}$$

a well-known result [5, p. 169].

$$\begin{aligned}\int_{x_g - \frac{\Delta}{2}}^{x_g + \frac{\Delta}{2}} dx e^{-ikx} (x - x_g) &= \int_{-\frac{\Delta}{2}}^{\frac{\Delta}{2}} dx' e^{-ik(x' + x_g)} x' \\ &= e^{-ikx_g} \int_{-\frac{\Delta}{2}}^{\frac{\Delta}{2}} x' dx' e^{-ikx'} \\ &= e^{-ikx_g} i \frac{d}{dk} \int_{-\frac{\Delta}{2}}^{\frac{\Delta}{2}} dx' e^{-ikx'} \\ &= e^{-ikx_g} i \frac{d}{dk} \left[\sin\left(\frac{k\Delta}{2}\right) / \left(\frac{k\Delta}{2}\right) \right] \Delta \\ &= e^{-ikx_g} i \left[\frac{\Delta}{2} \left[\cos\left(\frac{k\Delta}{2}\right) - \frac{\sin\left(\frac{k\Delta}{2}\right)}{\frac{k\Delta}{2}} \right] / \left(\frac{k\Delta}{2}\right) \right] \\ &= e^{-ikx_g} \frac{i}{k} \left[\cos\left(\frac{k\Delta}{2}\right) - \frac{\sin\left(\frac{k\Delta}{2}\right)}{\frac{k\Delta}{2}} \right] \Delta\end{aligned}$$

Assuming $\delta = 0$,

$$\rho_k = \sum_g \left[\frac{1}{-ik} e^{-ikx} \rho_g \Big|_{x_g - \frac{\Delta}{2}}^{x_g + \frac{\Delta}{2}} + \frac{\partial \rho}{\partial x} \Big|_g e^{-ikx_g} \int_{-\frac{\Delta}{2}}^{\frac{\Delta}{2}} d\Delta x \Delta x e^{-ikx} \right]$$

$$\begin{aligned}
&= \sum_g \left[\frac{i}{k} \rho_g (e^{-ik/2} - e^{ik/2}) e^{-ikx_g} + \frac{\partial \rho}{\partial x} \Big|_g e^{-ikx_g} i \frac{d}{dk} \int_{-\frac{\Delta}{2}}^{\frac{\Delta}{2}} d\Delta x e^{-ikx_g} \right] \\
&= \sum_g \left[\frac{\sin(\frac{k\Delta}{2})}{(\frac{k\Delta}{2})} \rho_g + \frac{\partial \rho}{\partial x} \Big|_g i \frac{d}{dk} \frac{\sin(k\Delta/2)}{(k\Delta/2)} + \dots \right] e^{-ikx_g} \Delta \\
&= \sum_g [\rho_g f_0(k) + \frac{\partial \rho}{\partial x} \Big|_g f_1(k) + \dots] e^{-ikx_g} \Delta
\end{aligned}$$

where $f_n(k) = (i \frac{d}{dk})^n [\frac{\sin(k\Delta/2)}{(k\Delta/2)}]$.

Note that, although we do not have a measure of $d\rho/dx|_g$ and higher derivatives, we may either

- 1) approximate their values with a difference equation, for example, or
- 2) use their exact values in terms of the unknown ρ_k .

We take this second approach for now but return to the first.

Noting that $\rho = \frac{1}{L} \sum_{k=-\infty}^{\infty} e^{ikx} \rho_k$, we have

$$\left(\frac{d}{dx}\right)^n \rho \Big|_g = \frac{1}{L} \sum_{k=-\infty}^{\infty} (ik)^n e^{ikx_g} \rho_k \dots$$

Performing the operation $\Delta \sum_g e^{i(k-k')x_g} = L \delta_{kk'}$, $\delta_{kk'}$ the Kronecker delta,

$$\delta_{kk'} = \begin{cases} 1 & k = k' \\ 0 & k \neq k', \end{cases}$$

we have

$$\rho_k = \sum_g \rho_g f_0(k) e^{-ikx_g} + \sum_{n_{\text{odd}}} \left[\frac{(ik)^n}{n!} (i \frac{d}{dk})^n f_0(k) \right] \rho_k$$

We recognize the sum over n as (formally) $[\sin(-k \frac{d}{dk}) f_0(k)]$ where $\sin(-k \frac{d}{dk})$ operates on $f_0(k)$. We finally have

$$\rho_k = \rho_m \left[\frac{f_0(k)}{1 - \sin(-k \frac{d}{dk}) f_0(k)} \right]$$

That is, the infinite transform ρ_k is related to the finite transform ρ_m by the relation

$$\rho_k = \rho_m F(k)$$

This is a pleasant state indeed. Let us assume that we desire to obtain the function E_g (say) $= \sum_{k=-\infty}^{\infty} e^{ikx_g} E_k$. We know that E_k and E_m are related through the aliases to E_m , that is

$$E_g = \sum_{k=-\infty}^{\infty} e^{ikx_g} E_k = \sum_{m=-N/2+1}^{N/2} \sum_{p=-\infty}^{\infty} e^{ik_p x_g} E_{k_p}$$

where $k_p = m + Np$. If we can solve analytically for E_k (e.g. $E_k = -\frac{i\rho k}{k}$), then we may solve "exactly"

$$\begin{aligned} E_g &= \sum_m e^{imx_g} \sum_{p=-\infty}^{\infty} E_{k_p} \\ &= \sum_m e^{imx_g} -i\rho_m \sum_{p=-\infty}^{\infty} F(k_p)/k_p \\ &= \sum_m e^{imx_g} \left(-i\frac{\rho_m}{m}\right) \sum_p \left(\frac{m}{k_p}\right) \left[\frac{f_0(k_p)}{1 - \sin\left(-k_p \frac{d}{dk_p}\right) f_0(k_p)}\right] \\ &= \sum_m e^{imx_g} \left(-i\frac{\rho_m}{m}\right) \sum_p \left(\frac{\frac{\pi m}{N}}{\frac{\pi m}{N} + \pi p}\right) \frac{(-1)^p f_0(m)}{1 - (-1)^p \sin\left(-\frac{k_p}{m} \frac{d}{dm}\right) f_0(m)} \end{aligned}$$

We recognize the terms in the solution:

- 1) $\sum_m e^{imx_g} \left(-i\frac{\rho_m}{m}\right)$ is the standard FFT solution for E at the grid points without any corrections for aliasing.
- 2) $\sum_p \dots$ is the correction factor for aliasing.
- 3) $\sin\left(-k_p \frac{d}{dk_p}\right) f_0(k_p)$ carries the degree to which the continuous ρ is approximated by the Taylor series expansion.

By truncating this series, we are (equivalently) creating a difference equation to solve for E_g . This procedure is equivalent to creating a band-limited function as posited by Eastwood.

We illustrate this point by dealing with only the zeroth order term in the expansion for ρ (i.e. $\rho = \sum_g \Pi_g \rho_g$).

$$\begin{aligned} E_g &= \sum_m e^{imx_g} \left(-i\frac{\rho_m}{m}\right) \sum_p \frac{x}{x + \pi p} (-1)^p f_0(m) \\ &= \sum_m e^{imx_g} \left(-i\frac{\rho_m}{m}\right) \cot\left(\frac{m\Delta}{2}\right) \end{aligned}$$

where we have used the expansion [10, p. 217]

$$\cot x = \sum_{n=-\infty}^{\infty} \frac{1}{x + \pi n}$$

We are not surprised that, in agreement with Eastwood, this solution corresponds to

$$\rho_g = \frac{\phi_{g+1} - 2\phi_g + \phi_{g-1}}{\Delta^2}$$

$$E_g = \frac{\phi_{g+1} - \phi_{g-1}}{2\Delta} !$$

We may obtain as accurate an expression as patience allows by evaluating the sine series to any desired order and physically summing the resulting expression over as many ps as we choose! If we intend to use this scheme in a program where we repeatedly evaluate E_g given ρ_g , we need only evaluate the modifying terms at the start of the program once. Since this term converges for p as $\frac{1}{p^2}$, we expect rapid improvement in our evaluation for E over its aliases. We may in turn increase our accuracy in terms of Δ^n to any compatible order by keeping higher and higher terms in the sine expansion. For example, keeping the first sine term should give an order of accuracy better results than the common finite difference scheme.

Furthermore we still retain the ability to use particle shaping in these schemes. The subject of particle shaping remains a separate issue - what particle shape gives the best physics shall be briefly considered in the next section.

B.3 Particle Shapes

B.3.1 Cloud-in-Cell Weighting

At each time step the particle contributes to the density and derives a force from the fields based on its position. Commonly the rule for assigning the density and calculating the forces for a discrete array of grid points based on a continuous particle position is known as interpolation. In particle simulation, however, it is useful to consider the alternate view of finite size particles.

In our 1D case, to calculate the force, we assign particle charge to each of the grid points:

$$q_g = \begin{cases} q(1 - \frac{|x_i - x_g|}{\Delta}) & |x_i - x_g| < \Delta \\ 0 & |x_i - x_g| > \Delta \end{cases} \quad (\text{B.3})$$

The same scheme is obtained by considering the particle to be a constant density slab of thickness Δ and infinite cross section. This is known as cloud-in-cell (CIC) weighting [5].

Charge density for field calculations may also be assigned to each grid point based on the volume of this particle in each cell. More generally, after counting particles within each grid cell, we obtain a charge density,

$$\rho(x) = \sum_g \int_0^L dx' \rho(x') \int_{-\frac{\Delta}{2}}^{\frac{\Delta}{2}} d\Delta x S(x' - x_g - \Delta x) / \int_{-\frac{\Delta}{2}}^{\frac{\Delta}{2}} d\Delta x \equiv \sum_g q_g \delta(x - x_g) \quad (\text{B.4})$$

where S is the particle shape which determines assignment of particle charge to the grid for calculation of field quantities.

The idea of finite size particles is easily incorporated into plasma theory and is particularly useful in studying the effects of higher order interpolation schemes or the use of “smoothing factors” to promote more realistic simulation behaviour. For example, the use of “smoothing factors” may be interpreted in terms of “effective particle shapes”. Thus, a principal benefit of the finite size particle concept is as a bookkeeping tool. It ensures that we may analytically compute the effects of our charge sharing and force interpolation schemes.

B.3.2 Optimal Particle Shape

Potential for Finite Size Particles

The Coulomb potential for a pair of point particles is

$$\phi(r) = \frac{e^2}{r}, \quad r = |\vec{x}_2 - \vec{x}_1|$$

This can be written in the equivalent form

$$\phi = \int dx' \int dx'' \frac{e^2 \delta(x' - x_1) \delta(x'' - x_2)}{|x'' - x'|}$$

for point particles or, more generally,

$$\phi = \int dx' \int dx'' \frac{e^2 S(x' - x_1) S(x'' - x_2)}{|x'' - x'|}$$

for finite size particles which includes point particles as a subclass.

To exhibit the explicit dependence of ρ on the separation of finite size particle centers we note

$$S(x' - x_1) = \left(\frac{1}{2\pi}\right)^3 \int dk S_k e^{ik(x' - x_1)}$$

and therefore

$$\phi = \frac{e^2}{(2\pi)^6} \int dx' \int dx'' \int dk \int dk' \frac{S_k S_{k'} e^{ik(x' - x_1)} e^{ik'(x'' - x_2)}}{|x'' - x'|}$$

Changing coordinates to $\bar{x} = \frac{x' + x''}{2}$, the position of the center of charge elements, and Δx , the separation between charge elements, we have

$$\begin{aligned} \phi &= \frac{e^2}{(2\pi)^6} \int d\bar{x} \int d\Delta x \int dk \int dk' \frac{S_k S_{k'} e^{ik(\bar{x} - \frac{\Delta x}{2} - x_1)} e^{ik'(\bar{x} + \frac{\Delta x}{2} - x_2)}}{|\Delta x|} \\ &= \frac{e^2}{(2\pi)^6} \int d\bar{x} \int d\Delta x \int dk \int dk' \frac{S_k S_{k'}}{|\Delta x|} e^{i(k+k')\bar{x} - i(k-k')\frac{\Delta x}{2} - i(kx_1 + k'x_2)} \end{aligned}$$

We next use the identity $\int dx e^{-i(k-k')x} = \int dx e^{-ikx} (e^{ik'x}) = 2\pi\delta(k - k')$. (This can be most easily seen in that $(\frac{1}{2\pi}) \int dk e^{ikx} \delta(k - k') = e^{ik'x}/2\pi$ so that the Fourier Transform of $e^{ik'x}$ is $2\pi\delta(k - k')$).

$$\begin{aligned} \phi &= \frac{e^2}{(2\pi)^6} \int d\Delta x \int dk \int dk' \frac{S_k S_{k'}}{|\Delta x|} e^{i(k-k')\frac{\Delta x}{2} - i(kx_1 + k'x_2)} \int d\bar{x} e^{i(k+k')\bar{x}} \\ &= \frac{e^2}{(2\pi)^6} \int d\Delta x \int dk \int dk' \frac{S_k S_{k'}}{|\Delta x|} e^{i(k-k')\frac{\Delta x}{2} - i(kx_1 + k'x_2)} (2\pi)^3 \delta(k + k') \\ &= \frac{e^2}{(2\pi)^3} \int d\Delta x \int dk \frac{S_k S_{-k}}{|\Delta x|} e^{-ik\Delta x + ikx} \end{aligned}$$

Now we may transform $\phi(r)$

$$\phi_{k'} = \int dr e^{-ik'r} \phi(r)$$

$$\begin{aligned}
&= \frac{e^2}{(2\pi)^3} \int dr \int \int d\Delta x dk \frac{S_k S_{-k}}{|\Delta x|} e^{ik\Delta x} e^{-i(k'+k)r} \\
&= e^2 \int \int d\Delta x dk \frac{S_k S_{-k}}{|\Delta x|} e^{ik\Delta x} \delta(k' + k) \\
\phi_k &= \int d\Delta x e^2 \frac{S_k S_{-k}}{|\Delta x|} e^{-ik\Delta x} \\
&= S_k S_{-k} \phi'_k
\end{aligned}$$

We see that the presence of the shape merely modifies the standard form of the potential by a factor $|S_k|^2$.

Two Body Corellation Function for Finite Size Particles

The use of finite size particles to reduce collisions in simulations is a common technique to compensate for reduced shielding of charges from the relative smallness of the plasma parameter - $n\lambda_D^3$. We wish to examine how the two body correlation function (and therefore collisions) behaves with finite size particles and postulate the existence of an "optimal" particle shape in regard to the correlation function.

In thermal equilibrium Frieman and Book [20] have shown that, assuming a correlation function of the form

$$g(|x_1 - x_2|, v_1, v_2) = f_M(v_1) f_M(v_2) \Psi(|x_1 - x_2|)$$

where $f_M = (m/2\pi kT)^{3/2} e^{-mv^2/2kT}$, the spatial dependent part of Ψ obeys the equation

$$\begin{aligned}
(v_1 - v_2) \cdot \frac{\partial \Psi}{\partial \vec{x}} + \frac{1}{kT} \frac{\partial \phi}{\partial \vec{x}} \cdot (v_1 - v_2) \Psi &= -\frac{1}{kT} \frac{\partial \phi}{\partial \vec{x}} \cdot (v_1 - v_2) \\
-\frac{n}{kT} \int dx_3 \left(\frac{\partial \phi(|x_1 - x_3|)}{\partial x_1} \cdot v_1 \Psi(2, 3) + \frac{\partial \phi(|x_2 - x_3|)}{\partial x_2} \cdot v_2 \Psi(1, 3) \right) \\
\text{or } (v_1 - v_2) \cdot \left[\frac{\partial \Psi}{\partial \vec{x}} + \frac{1}{kT} \frac{\partial \phi}{\partial \vec{x}} (\Psi + 1) \right] &= -\frac{n}{kT} \frac{\partial}{\partial \vec{x}} \int d\Delta x \phi(|\vec{x} - \Delta x|) \Psi(|\Delta x|) \\
\frac{\partial \Psi}{\partial r} + \frac{1}{kT} \frac{\partial \phi}{\partial r} (\Psi + 1) &= -\frac{n}{kT} \frac{\partial}{\partial r} \int d\Delta x \phi(|\vec{x} - \Delta x|) \Psi(|\Delta x|)
\end{aligned}$$

The effect of finite particle size on the potential ϕ is to reduce it at short distances so that it remains finite even at zero separation. We plot the electric field and potential versus separation distance in the figure below. We

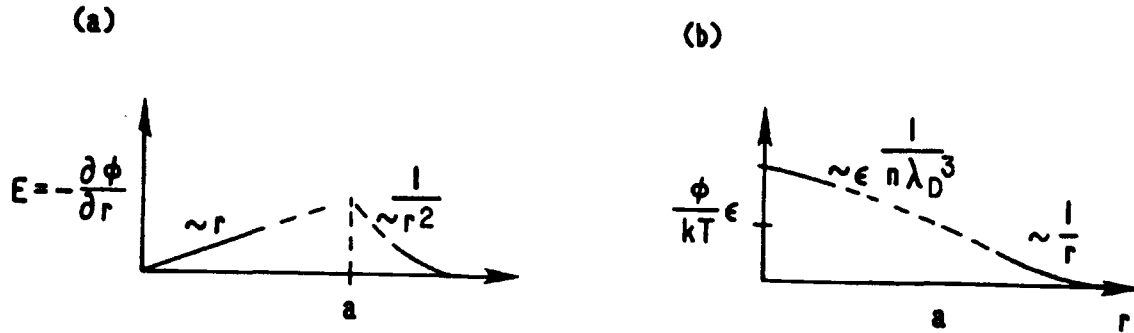


Figure B.2: This shows the potential vs radius for particles.

note that, as the particles overlap, the force decreases, finally approaching zero for small r . At large distances the electric field and potential both must approach the classical Coulomb potential.

If $\frac{e\phi}{kT}$ is on the order of ϵ at a (by assumption) then it is of the same order for $r < a$. This then changes our asymptotic analysis. The terms above are in the ratios given below, as deduced from Book and Frieman,

$$\begin{array}{ccc}
 \text{"small" } r_0 \leq n^{-\frac{1}{2}} & \frac{\partial \Psi}{\partial x} & \frac{\partial V}{\partial x} & nr_0^3 \frac{\partial}{\partial x} \int d\Delta x V(|x - \Delta x|) \Psi(|\Delta x|) \\
 & \epsilon & \epsilon & < \epsilon^2 \\
 r_0 \geq a \sim \lambda_D & \epsilon & \epsilon & \epsilon
 \end{array}$$

where $V \equiv \frac{e\phi}{kT}$, $x \equiv \frac{r}{r_0}$.

For "small" r we have the balance

$$\begin{aligned}
 \frac{\partial \Psi}{\partial x} + \frac{\partial V}{\partial x}(\Psi + 1) &= 0 \\
 e^V \frac{\partial(\Psi + 1)}{\partial x} + \frac{\partial e^V}{\partial x}(\Psi + 1) &= 0 \\
 \frac{\partial}{\partial x}[e^V(\Psi + 1)] &= 0 \\
 \Psi &= -1 + \text{const}e^{-V} \\
 \Psi &= -1 + \text{const}e^{-\frac{e\phi}{kT}}
 \end{aligned}$$

Note for V large, $\frac{\partial \Psi}{\partial x}$ balances $\frac{\partial V}{\partial x}$, while for V small, $\frac{\partial \Psi}{\partial x}$ effectively balances itself.

For "large" r (V small) the balance must be

$$\frac{\partial \Psi}{\partial x} + \frac{\partial V}{\partial x} + n\lambda_D^3 \frac{\partial}{\partial x} \int d\Delta x V(|\vec{x} - \Delta x|) \Psi(|\Delta x|) = 0$$

We have immediately that

$$\Psi + V + n\lambda_D^3 \int d\Delta x V(|\vec{x} - \Delta x|) \Psi(|\Delta x|) = \text{const}$$

Using the convolution theorem,

$$\int d\Delta x V(|\vec{x} - \Delta x|) \Psi(|\Delta x|) = \left(\frac{1}{2\pi}\right)^3 \int dk V_k \Psi_k e^{ikx},$$

we have the solution in Fourier components

$$\Psi_k + V_k + nV_k \Psi_k = [4\pi^2 \delta(k) \delta(\mu) / k^2] \text{const}$$

$$\Psi_k = -\frac{V_k}{1 + nV_k} + \frac{4\pi^2 \delta(k) \delta(\mu)}{k^2 (1 + nV_k)} \text{const}$$

$$\begin{aligned} \Psi &= -\left(\frac{1}{2\pi}\right)^3 \int d\vec{k} \left[\frac{V_k}{1 + nV_k} - \frac{4\pi^2 \delta(k) \delta(\mu)}{k^2 (1 + nV_k)} \text{const} \right] e^{ikx} \\ &= \frac{\text{const}}{1 + nV_0} - \frac{1}{4\pi^2} \int dk k^2 \frac{V_k}{1 + nV_k} [(e^{ikr} - e^{-ikr}) / ikr] \end{aligned}$$

For ϕ we have the standard Coulomb potential integrated over the shape functions

$$\begin{aligned} V &= \int d\Delta x_1 \int d\Delta x_2 \frac{e^2 S(\Delta x_1) S(\Delta x_2)}{|x_1 + \Delta x_1 - x_2 - \Delta x_2|} / kT \\ &= \left(\frac{1}{2\pi}\right)^3 \int d\vec{k} |S_k|^2 \phi_k / kT e^{ikx} \\ \phi_k &= \int d\vec{x} \frac{e^2}{r} e^{-ikx} \\ &= 2\pi e^2 \int_0^\infty dr r \int_{-1}^1 d\mu e^{-ikr\mu} \\ &= \frac{2\pi e^2}{-ik} \int_0^\infty dr (e^{-ikr} - e^{ikr}) \\ &= \frac{2\pi e^2}{k} i \lim_{\alpha \rightarrow 0} \left[\frac{e^{(-ik-\alpha)r}}{-ik-\alpha} - \frac{e^{(ik-\alpha)r}}{ik-\alpha} \right] \Big|_0^\infty \\ &= \frac{4\pi}{k^2}, \end{aligned}$$

so that $\Psi = -\frac{1}{4\pi^2} \int_0^\infty dk \left[\frac{(4\pi e^2/kT)S_k^2}{1+S_k^2} / (k\lambda_D)^2 \right] \left(\frac{e^{ikr} - e^{-ikr}}{ikr} \right)$.

For $S_k^2 = 1$ (point particles) we have poles at $k = \pm i/\lambda_D$. We extend the limits of integration from $-\infty$ to ∞ since the integrand is even in k and

$$\Psi = -\left(\frac{1}{2\pi}\right)^3 \frac{e^2}{kT} \int_{-\infty}^{\infty} dk \left[\frac{k^2}{k^2 + (1/\lambda_D)^2} \right] \left(\frac{e^{ikr} - e^{-ikr}}{ikr} \right)$$

We note that the portion of the integral involving e^{ikr} must be evaluated over contour 1 while that for e^{-ikr} must be evaluated over contour 2 in Figure B.3.

$$\begin{aligned} \int_{-\infty}^{\infty} dk \frac{k^2}{k^2 + (1/\lambda_D)^2} \frac{e^{ikr}}{ikr} &= \int_{-\frac{\pi}{2}}^{\frac{\pi}{2}} d\epsilon e^{i\theta} \frac{(\frac{i}{\lambda_D})^2}{2(\frac{i}{\lambda_D})\epsilon e^{i\theta}} \frac{e^{i(\frac{i}{\lambda_D})r}}{i(\frac{i}{\lambda_D})r} \\ &= \frac{1}{2} \int_0^{2\pi} d\theta \frac{e^{-r/\lambda_D}}{r} \\ &= \pi \frac{e^{-r/\lambda_D}}{r} \end{aligned}$$

With a like contribution from the other contour so that

$$\Psi = -\frac{e^2}{kTr} e^{-r/\lambda_D}$$

as in Frieman and Book[20].

An "Optimal" Particle Shape

We see that the trade-off between the (real) point particle case and the finite particle case must be the density (in the form of $\lambda_D = \sqrt{T/n}$) and the particle shape. Since g (the two body correlation function) represents the error due to collisions, we should seek to minimize this error.

An appropriate shape should result from the minimization principle:

$$\frac{\partial}{\partial s} \int d^3x (\Psi(s) - \Psi(\delta))^2 = 0$$

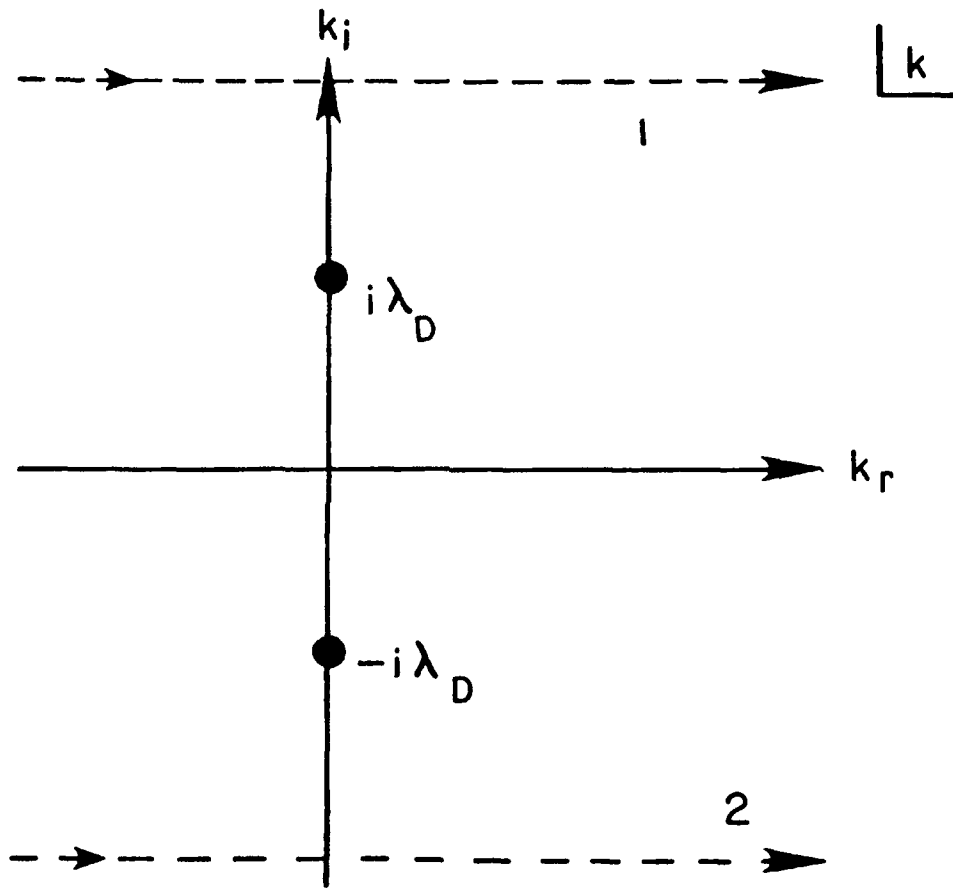


Figure B.3: The contour of integration to evaluate particle shape.

B.4 Extension to Two Dimensions

We extend the simulation to two dimensions. The model is similar to the 1D case but now the potential varies both in r and z . The model and boundary conditions are pictured in Figure 6.1. We shall find the boundary condition at $r=R$ is flexible. The condition at $r=0$ reflects the fact that the particle distribution is continuous (no line charge).

B.4.1 Poisson's Equation in Spherical and Cylindrical Coordinates

Azimuthal symmetry about the z -axis suggests use of cylindrical or spherical coordinates. Poisson's equation and the electrostatic potential in these two systems is:

$$\frac{1}{\rho} \frac{\partial}{\partial \rho} (\rho E_\rho) + \frac{\partial E_z}{\partial z} = 4\pi\rho$$

$$\vec{E} = -\vec{\nabla}\phi = \frac{\partial\phi}{\partial\rho}\hat{\rho} + \frac{\partial\phi}{\partial z}\hat{z}$$

or

$$\frac{1}{r^2} \frac{\partial}{\partial r} (r^2 E_r) + \frac{1}{r \sin\theta} \frac{\partial}{\partial \theta} (\sin\theta E_\theta) = 4\pi\rho$$

$$\vec{E} = \frac{\partial\phi}{\partial r}\hat{r} + \frac{1}{r} \frac{\partial\phi}{\partial\theta}\hat{\theta}$$

Numerical solution of Poisson's equation is facilitated when the ∇^2 operator can be expressed with one "Poisson-like" variable. Cylindrical coordinates therefore are chosen.

B.4.2 Continuous Solution

In cylindrical coordinates, we have an equation for the potential $\phi(\rho, z)$:

$$\frac{1}{\rho} \frac{\partial}{\partial \rho} \left(\rho \frac{\partial \phi}{\partial \rho} \right) + \frac{\partial^2 \phi}{\partial z^2} = -4\pi\rho$$

The charge density ρ can be expanded in an infinite Fourier series, $\frac{1}{L} \sum_{k=-\infty}^{\infty} \rho(\rho) \exp^{ikz}$, with $\rho_k(\rho) \equiv \int_0^L dz \exp^{-ikz} \rho(\rho, z)$. This suggests a form for the ϕ solution,

$$\phi = \frac{1}{L} \sum_{k=-\infty}^{\infty} \phi_k(\rho) \exp^{ikz} + \phi_h,$$

where $\phi_k(\rho)$ are particular solutions to the inhomogenous equations

$$\frac{1}{\rho} \frac{\partial}{\partial \rho} \left(\rho \frac{\partial \phi_k(\rho)}{\partial \rho} \right) - k^2 \phi_k(\rho) = -4\pi \rho_k(\rho)$$

and ϕ_h is a homogeneous solution to the cylindrical Poisson equation which allows ϕ to satisfy the boundary conditions in z , $\phi(0) = 0$, $\phi'(L) = 0$.

The Green's function solution for ϕ_k may be expressed in terms of modified Bessel functions $I_0(\rho)$, $K_0(\rho)$. The requirement for finite ϕ at $r=0$ precludes use of K_ν which behaves as $\ln(\frac{x}{2})$ for $x \ll 1$.

We may add to this any solution to the homogeneous equation which satisfies the given boundary condition. However, we choose this solution to be zero in absence of a source, ρ . The homogeneous solution consists of products of exponentials (real or imaginary) in z and appropriate Bessel functions, $\phi_h = \sum_{k'} J_0(k'\rho)[A_{k'}e^{k'z} + B_{k'}e^{-k'z}]$. The boundary conditions on the homogeneous solution derive from those on ϕ itself, i.e. $\phi_h = \phi - \phi_p$. The boundary conditions in r are $\phi'_h(0, z) = 0$ and $\phi_h(L, z) = 0$. The first condition allows solutions of the form J_0 while the boundary conditions at $r=R$ restrict kR to zeroes of J_0 . The boundary conditions in z are $\phi_h(0) = -\sum_k \phi_k(\rho)$ and $\phi'_h(L) = -i \sum_k k \phi_k(\rho)$ and, using the orthogonality relation [24, Eqn. (3.95), p. 106],

$$\int_0^R \rho J_0(k'\rho) J_0(k\rho) d\rho = \frac{R^2}{2} [J_1(kR)]^2 \delta_{k'k},$$

determine the constants in the expression for ϕ_h ,

$$A_{k'} + B_{k'} = 2 \int_0^R \rho \phi_h(0) J_0(k\rho) d\rho / R^2 J_1^2(kR)$$

$$\text{and } k'(A_{k'}e^{k'L} - B_{k'}e^{-k'L}) = 2 \int_0^R \rho \phi'_h(L) J_0(k\rho) d\rho / R^2 J_1^2(kR)$$

B.4.3 Matrix Solution

Boundary conditions

We may specify either Dirichlet or Neumann boundary conditions or equally well a combination of the two—"mixed boundary conditions".

Dirichlet Boundary conditions Here the value of the potential is given at a boundary. Assume that the n^{th} grid line contains the given values $\phi_{i,n} = f_i$. The differential operator at the $n - 1^{\text{st}}$ grid line is:

$$\frac{\phi_{i,n} - 2\phi_{i,n-1} + \phi_{i,n-2}}{\Delta^2} = \rho_{i,n-1}$$

$$\text{or } \frac{-2\phi_{i,n-1} + \phi_{i,n-2}}{\Delta^2} = \rho_{i,n-1} - \frac{f_i}{\Delta^2}$$

The boundary value is absorbed into the charge.

Neumann Boundary Conditions Here the value of the electric field is given at a boundary. Assume that the n^{th} grid line contains the given values $\phi'_{i,n} = g_i \equiv \frac{\phi_{i,n+1} - \phi_{i,n-1}}{2\Delta}$

Then the differential operator on the n^{th} grid line becomes

$$\frac{\phi_{i,n+1} - 2\phi_{i,n} + \phi_{i,n-1}}{\Delta^2} = \rho_{i,n}$$

$$\frac{-2\phi_{i,n} + 2\phi_{i,n-1}}{\Delta^2} = \rho_{i,n} - \frac{2g_i}{\Delta}$$

Again the boundary value is absorbed into the charge so that we are free to consider homogeneous boundary values, $\phi_h = 0$ or $\phi'_h = 0$, only.

Mixed Boundary Conditions Some combination of ϕ and ϕ' are given on separate (therefore not Cauchy) boundaries. Assume we have Dirichlet boundary conditions $\phi = 0$ at $z=0$ and Neumann boundary condition $\phi' = 0$ at $x=L$. The boundary conditions may remain unspecified in the r direction.

Difference Equations

To obtain the discrete analog to the ∇^2 operator we use the 3-point two dimensional difference, that is, since

$$D_{i+\frac{1}{2}}\phi = \frac{\phi_{i+1} - \phi_i}{\Delta},$$

$$D_i^2\phi = \frac{\phi_{i+1} - 2\phi_i + \phi_{i-1}}{\Delta^2}$$

The difference equation is readily obtained as

$$\frac{1}{r_m} \frac{[r_{m+\frac{1}{2}}(\phi_{m+1,n} - \phi_{m,n}) - r_{m-\frac{1}{2}}(\phi_{m,n} - \phi_{m-1,n})]}{\Delta r^2} + \left[\frac{(\phi_{m,n+1} - \phi_{m,n}) - (\phi_{m,n} - \phi_{m,n-1})}{\Delta z^2} \right] = -4\pi\rho_{m,n} \quad (\text{B.5})$$

for the interior points.

At the boundaries (particularly at $r=0$) it is useful to apply the integral form of Gauss' Law, Eqn. (3.1(c)).

$$\int_V \nabla \cdot E d\vec{x} = \int_V 4\pi\rho d\vec{x}$$

$$\int_S \vec{E} \cdot d\vec{S} = 4\pi q$$

where the surface and volume integrals are over the cells of interest.

At $m=0$

$$E_{r\frac{1}{2},n} [2\pi(\frac{\Delta r}{2})\Delta z] + (E_{z0,n+\frac{1}{2}} - E_{z0,n-\frac{1}{2}}) [\pi(\frac{\Delta r}{2})^2] = 4\pi q_{0,n}$$

$$4 \frac{(\phi_{0,n} - \phi_{1,n})}{\Delta r^2} + \frac{[(\phi_{0,n} - \phi_{0,n+1}) - (\phi_{0,n-1} - \phi_{0,n})]}{\Delta z^2} = \frac{4\pi q_{0,n}}{\Delta V}$$

$$\frac{6\phi_{0,n} - 4\phi_{1,n} - \phi_{0,n+1} - \phi_{0,n-1}}{\Delta^2} = 4\pi\rho_{0,n} \quad (\text{B.6})$$

for $\Delta r = \Delta z = \Delta$ and $\Delta V = \pi(\frac{\Delta r}{2})^2 \Delta z$.

At $m > 0$

$$\pi[(m + \frac{1}{2})^2 - (m - \frac{1}{2})^2] \Delta r^2 (E_{zm,n+\frac{1}{2}} - E_{zm,n-\frac{1}{2}}) +$$

$$2\pi(m + \frac{1}{2}) \Delta r \Delta z E_{rm+\frac{1}{2},n} - 2\pi(m - \frac{1}{2}) \Delta r \Delta z E_{rm-\frac{1}{2},n} = 4\pi q_{m,n}$$

$$2\pi m \Delta r^2 (\frac{\phi_{m,n} - \phi_{m,n+1}}{\Delta z} + \frac{\phi_{m,n} - \phi_{m,n-1}}{\Delta z}) +$$

$$2\pi(m + \frac{1}{2}) \Delta r \Delta z \frac{\phi_{m,n} - \phi_{m+1,n}}{\Delta r} + 2\pi(m - \frac{1}{2}) \Delta r \Delta z \frac{\phi_{m,n} - \phi_{m-1,n}}{\Delta r} = 4\pi q_{m,n}$$

$$2\pi m \Delta (2\phi_{m,n} - \phi_{m,n+1} - \phi_{m,n-1}) +$$

$$2\pi m \Delta [2\phi_{m,n} - (1 + \frac{1}{2m})\phi_{m+1,n} - (1 - \frac{1}{2m})\phi_{m-1,n}] = 4\pi q_{m,n}$$

$$\frac{-(1 - \frac{1}{2m})\phi_{m-1,n} + 4\phi_{m,n} - (1 + \frac{1}{2m})\phi_{m+1,n} - \phi_{m,n+1} - \phi_{m,n-1}}{\Delta^2} = 4\pi\rho_{m,n}$$

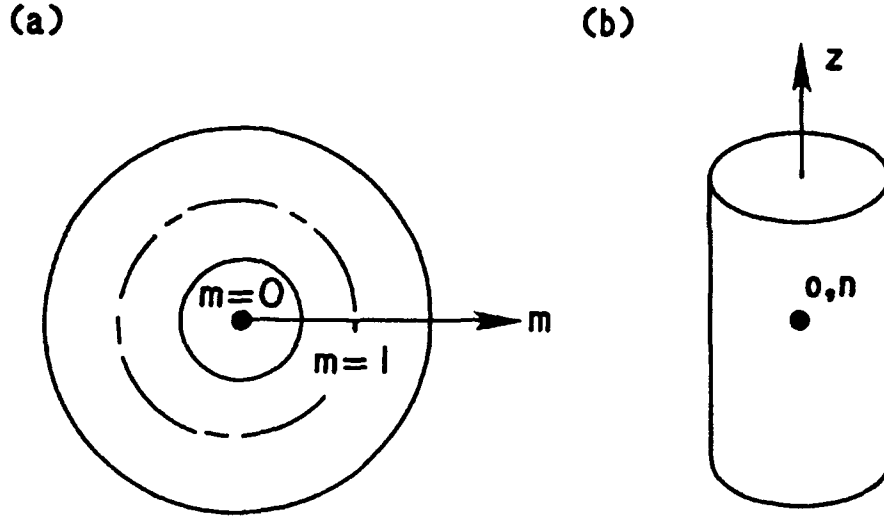


Figure B.4: This is Gauss' Law for $m = 0$.

for $\Delta r = \Delta z$ and $\Delta V = 2\pi m \Delta r^2 \Delta z$.

For $E_r = 0$ at $r = R \equiv M\Delta r$, we approximate $\phi_{M+1,n} = \phi_{M,n}$

$$\left(3 - \frac{1}{2m}\right)\phi_{M,n} - \left(1 - \frac{1}{2m}\right)\phi_{M-1,n} - \phi_{M,n+1} - \phi_{M,n-1} = 4\pi\rho_{m,n} \quad (\text{B.7})$$

For $\phi = 0$ at $r = R \equiv (M+1)\Delta r$

$$4\phi_{M,n} - \left(1 - \frac{1}{2M}\right)\phi_{M-1,n} - \phi_{M,n+1} - \phi_{M,n-1} = \rho_{M,n} \quad (\text{B.8})$$

B.4.4 Solution for Electric-field

Mixed Boundary Conditions in z

We use $m = 1$ at $r = 0$. Using $E = -\nabla\phi$ at interior points ($ngr - 1 > nr > 2, ng - 1 > nz > 1, ngr = M + 1$):

$$E_{rm,n} = -\frac{\phi_{m+1,n} - \phi_{m-1,n}}{2}$$

$$E_{zm,n} = -\frac{\phi_{m,n+1} - \phi_{m,n-1}}{2}$$

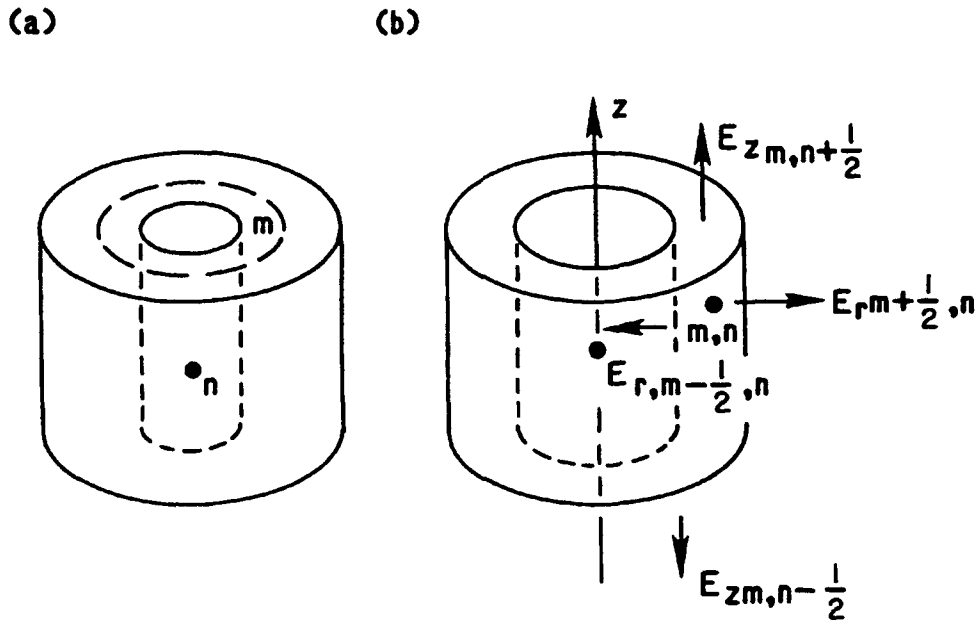


Figure B.5: This is Gauss' Law for $m > 0$.

For $nr = 1, ng - 1 > nz > 1$

$$E_{r1,n} = 0 \quad E_{z1,n} = -\frac{\phi_{1,n+1} - \phi_{1,n-1}}{2}$$

For $nr = ngr, ng - 1 > nz > 1$ and $E_r(R) = 0$

$$E_{rngr,n} = 0 \quad E_{zngr,n} = -\frac{\phi_{ngr,n+1} - \phi_{ngr,n-1}}{2}$$

For $ngr - 1 > nr > 2, nz = ng$

$$E_{rm,ng} = -\frac{\phi_{m+1,ng} - \phi_{m-1,ng}}{2} \quad E_{zm,ng} = 0$$

At $n=0, \phi = 0$

$$\frac{\partial E_z}{\partial z} + \frac{1}{r} \frac{\partial}{\partial r} (r E_r) = 4\pi\rho$$

$$\frac{E_{zm,n+1} - E_{zm,n-1}}{2\Delta z} + \left(\frac{1}{m-1}\right) \frac{(m - \frac{1}{2})E_{rm+\frac{1}{2},n} - (m - \frac{3}{2})E_{rm-\frac{1}{2},n}}{\Delta r} = 4\pi\rho_{m,n}$$

For $ngr - 1 > nr > 2, nz = 0$

$$\begin{aligned}
 E_{zm,0} &= Ez_{m,2} - 8\pi\rho_{m,1} + 2 \times \left[-\frac{(m - \frac{1}{2})}{m - 1}(\phi_{m+1,1} - \phi_{m,1}) \right. \\
 &\quad \left. + \frac{m - \frac{3}{2}}{m - 1}(\phi_{m,1} - \phi_{m-1,1}) \right] \\
 &= Ez_{m,2} - 8\pi\rho_{m,1} - 2\left[1 + \frac{1}{2(m - 1)}\right]\phi_{m+1,1} \\
 &\quad - 2\left[1 - \frac{1}{2(m - 1)}\right]\phi_{m-1,1} + 4\phi_{m,1}
 \end{aligned}$$

$E_{r,m,0} = 0$ at $r=R$ for no surface charge.

At $r=R$ $\phi = 0$ for $\phi(R) = 0$

$$\begin{aligned}
 E_{zM,n} &= 0 \\
 \frac{E_{zm,n+\frac{1}{2}} - E_{zm,n-\frac{1}{2}}}{\Delta z} &+ \\
 \frac{1}{m\Delta} \frac{(m+1)\Delta E_{rm+1,n} - E_{rm-1,n}(m-1)\Delta}{2\Delta} &= 4\pi\rho_{m,n} \\
 E_{rM+1,n} &= \frac{(M-2)}{M} E_{rM-1,n} + \\
 &\quad \left(\frac{M-1}{M}\right)[8\pi\rho_{M,n} - 2(\phi_{M,n} - \phi_{M,n-1}) + 2(\phi_{M,n+1} - \phi_{M,n})] \\
 &= \left(1 - \frac{2}{M}\right) E_{rM-1,n} + \\
 &\quad \left(1 - \frac{1}{M}\right)[8\pi\rho_{M,n} + 2(\phi_{M,n+1} + \phi_{M,n-1}) - 4\phi_{M,n}]
 \end{aligned}$$

At the corners:

For $m,n=1,0$

$$E_{r1,0} = 0 \quad E_{z1,0} = E_{z1,2} - 8\pi\rho_{1,1} + 4(\phi_{1,1} - \phi_{2,1})$$

At $(m,n)=(1,ng)$,

$$E_{r1,ng} = 0 \quad E_{z1,ng} = 0$$

At $r=R, z=0$ $E_r = 0, E_z = 0$ (no surface charge).

At $r=R, z=L, (m,n)=(ngr,ng), E_z = 0$

$$E_{rM+1,N} = \left(1 - \frac{2}{M}\right) E_{rM-1,N} + \left(1 - \frac{1}{M}\right)[8\pi\rho_{M,N} + 4(\phi_{M,N-1}) - \phi_{M,N}]$$

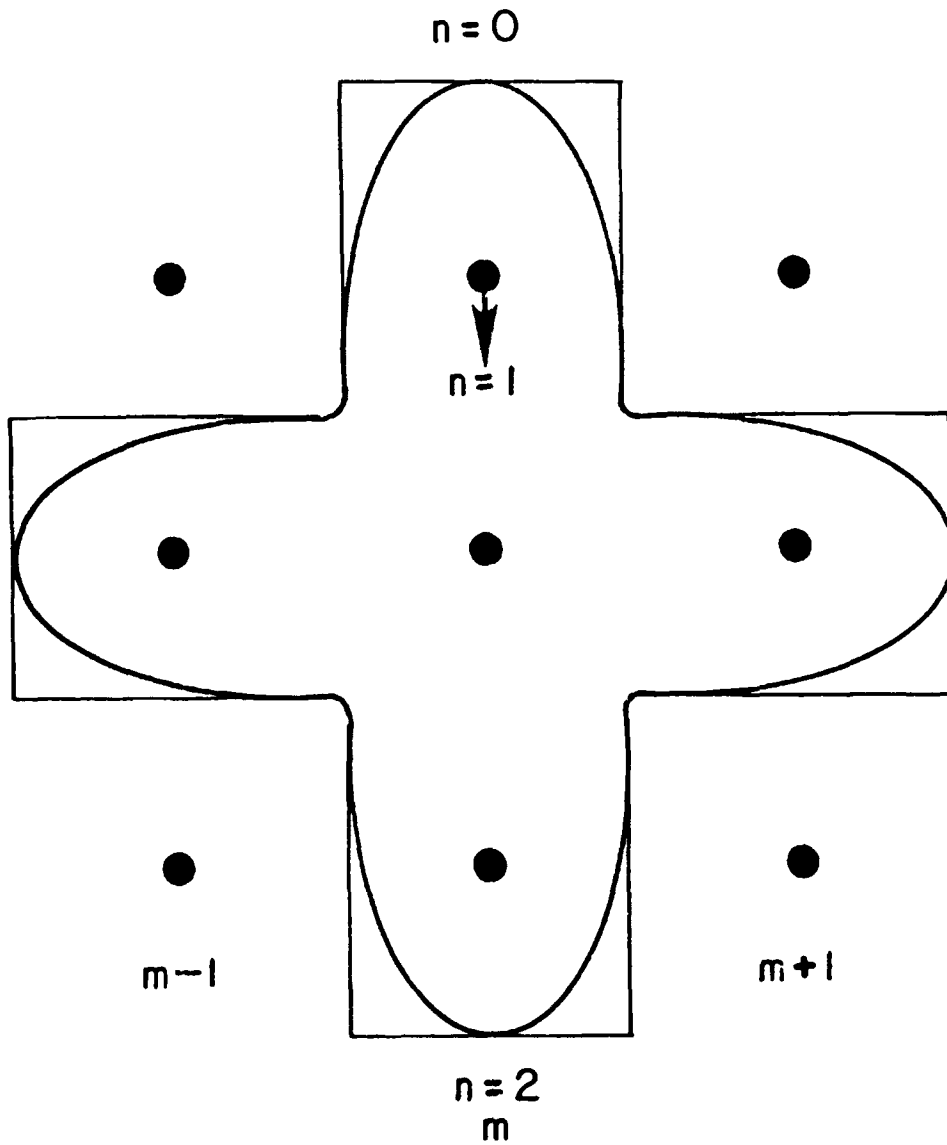


Figure B.6: This shows the calculation of E on the boundaries.

B.4.5 Charge Sharing/Force Interpolation

The weighting scheme chosen in 1D may be interpreted as a dipole expansion of the charge density about the midpoint between cells[29]. In two dimensions a similar approach, but including a quadrupole term yields a scheme known as area weighting [5, p. 244]. This approach is roughly equivalent to the scheme used here consolidating the charge as a ring of finite size. In the limit of large r , the two approaches are exactly equivalent.

This scheme may be readily derived by application of Gauss' Law:

$$\begin{aligned} \int \vec{E} \cdot d\vec{A} &= 4\pi q \\ E_{r+}(z)(2\pi r_+ \Delta z) - E_{r-}(z)(2\pi r_- \Delta z) + \\ E_{z+}[\pi(r_+^2 - r_-^2)] - E_{z-}[\pi(r_+^2 - r_-^2)] &= 4\pi\rho[\pi(r_+^2 - r_-^2)]\Delta z \\ &= \delta E_r(z_+) + (1 - \delta)E_r(z_-) \\ E_r(2\pi r \Delta z) - E_{r-}(2\pi r_- \Delta z) + (E_{z+} - E_{z-})[\pi(r^2 - r_-^2)] &= 4\pi\rho_r[\pi(r^2 - r_-^2)]\Delta z \end{aligned}$$

where we designate +,- as the upper and lower limits of the particle extent.

$$\begin{aligned} rE_r &= E_{r-}r_- + 2\rho[\pi(r^2 - r_-^2)] - \Delta E_z \frac{(r^2 - r_-^2)}{2\Delta z} + 2\pi(\rho_r - \rho)[(r^2 - r_-^2)] \\ &= E_{r-}r_- + \left(\frac{r^2 - r_-^2}{2}\right)[4\pi\rho - \frac{\Delta E_z}{\Delta z}] + \dots \\ &= E_{r-}r_- + \left(\frac{r^2 - r_-^2}{2}\right)\left[\frac{E_{r+}(2\pi r_+ \Delta z) - E_{r-}(2\pi r_- \Delta z)}{\pi(r_+^2 - r_-^2)\Delta z}\right] + \dots \\ &= E_{r-}r_- + \left(\frac{r^2 - r_-^2}{r_+^2 - r_-^2}\right)[r_+ E_{r+} - r_- E_{r-}] + \dots \\ &= r_+ E_{r+} \left(\frac{r^2 - r_-^2}{r_+^2 - r_-^2}\right) + r_- E_{r-} \left(\frac{r_+^2 - r^2}{r_+^2 - r_-^2}\right) + \dots \\ &= r_+ [\delta E_r(r_+, z_+) + (1 - \delta)E_r(r_+, z_-)] \left(\frac{r^2 - r_-^2}{r_+^2 - r_-^2}\right) \\ &\quad + r_- [\delta E_r(r_-, z_+) + (1 - \delta)E_r(r_-, z_-)] \left(\frac{r_+^2 - r^2}{r_+^2 - r_-^2}\right) + o(\Delta r) \\ (E_r(z) \approx E_r(z_-) + \delta[E_r(z_+) - E_r(z_-)]/\Delta z) \end{aligned}$$

Similarly

$$E_{r+}(2\pi r_+ \Delta z) - E_{r-}(2\pi r_- \Delta z) + (E_z - E_{z-})[\pi(r_+^2 - r_-^2)] = 4\pi\rho_z[\pi(r_+^2 - r_-^2)]\Delta z$$

$$\begin{aligned}
E_z &= E_{z-} + \Delta z [4\pi\rho_z - 2(r_+ E_{r_+} - r_- E_{r_-}) / (r_+^2 - r_-^2)] \\
&= E_{z-} + \delta z (E_{z_+} - E_{z-}) \\
&= \delta E_{z_+} + (1 - \delta) E_{z-} \\
&= \delta [E_z(r_+, z_+) (\frac{r_+^2 - r_-^2}{r_+^2 - r_-^2}) + E_z(r_-, z_+) (\frac{r_+^2 - r_-^2}{r_+^2 - r_-^2})] \\
&+ (1 - \delta) [(\frac{r_+^2 - r_-^2}{r_+^2 - r_-^2}) E_z(r_+, z_-) + E_z(r_-, z_-) (\frac{r_+^2 - r_-^2}{r_+^2 - r_-^2})]
\end{aligned}$$

In two-dimensions (r-z) we may continue to use the same charge sharing and force interpolation scheme as in the 1D case for the z direction. In r, however, we choose to treat the particle as a ring of uniform charge density,

$$\begin{aligned}
\rho &= \frac{q}{\pi(r_{i+\frac{1}{2}}^2 - r_{i-\frac{1}{2}}^2)\Delta z} \\
&= \frac{q}{2\pi r_i \Delta z \Delta r} \quad i > \frac{1}{2} \\
&= \frac{q}{\pi r_{i+\frac{1}{2}}^2 \Delta z} \quad i < \frac{1}{2}
\end{aligned}$$

The charge density of the particle remains uniform but varies with r as shown in Figure B.7.

The force is similarly calculated from

$$F_r = 2\pi \int r dr \rho E_r \equiv q_1 E_{r_1} + q_2 E_{r_2}, \text{ where } E_{r_{1,n}} \equiv \frac{q_{1,n}}{q_1} E_{r_{1,n}} + \frac{q_{1,n+1}}{q_1} E_{r_{1,n+1}}$$

Force weighting is identical to charge sharing except as noted for calculation of B. Since both the mass and the charge are distributed together and because of symmetry the acceleration for each bit of charge is the same for the particle treated as a whole as for individual bits.

Care must be taken in calculation of the force due to the magnetic field[8]. This force should act at the charge center of the particle which is located at

$$\begin{aligned}
\int_{r_{i-\frac{1}{2}}}^{r_i} r dr \rho &= \frac{1}{2} \int_{r_{i-\frac{1}{2}}}^{r_{i+\frac{1}{2}}} r dr \rho \\
r_z^2 - (r_i - \frac{1}{2})^2 &= r_i \\
r_z &= \sqrt{r_i^2 + \frac{1}{4}} \quad r_i > \frac{1}{2}
\end{aligned}$$

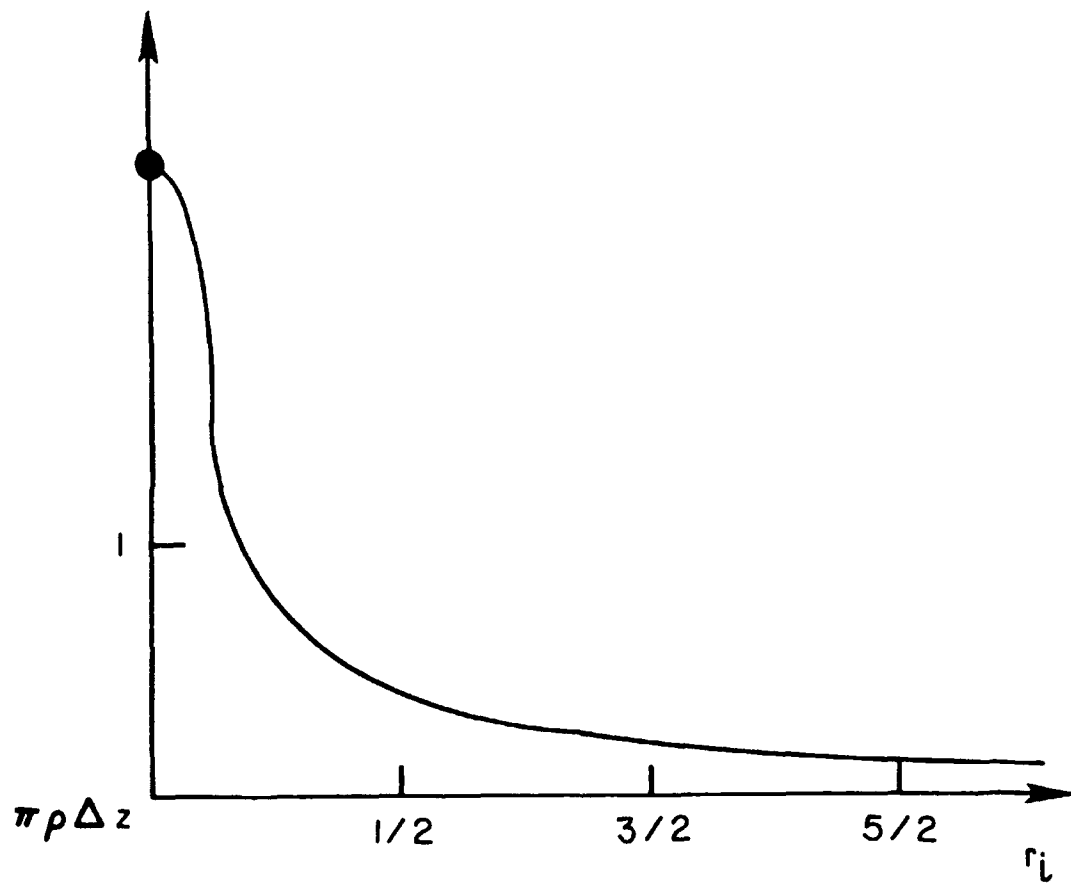


Figure B.7: This shows the variation of particle charge density with r .

$$= (r_i + \frac{1}{2})/\sqrt{2} \quad r_i < \frac{1}{2}$$

More elaborate schemes for charge weighting and force calculation may be used but one may often obtain a more "accurate" (less noisy) simulation by instead substituting a greater number of particles.

Appendix C

Buneman Algorithm Solution to the Mixed Boundary Condition Problem

The Buneman algorithm is a quick way to solve Poisson's equation without the use of Fourier transforms. In cylindrical coordinates with r and z as variables we have

$$\frac{1}{r} \frac{\partial}{\partial r} r \frac{\partial \phi}{\partial r} + \frac{\partial^2 \phi}{\partial z^2} = -4\pi\rho$$

and its finite difference form,

$$\frac{1}{r_m} [r_{m+\frac{1}{2}}(\phi_{m+1,n} - \phi_{m,n}) - r_{m-\frac{1}{2}}(\phi_{m,n} - \phi_{m-1,n})] + (\phi_{m,n+1} - 2\phi_{m,n} + \phi_{m,n-1}) = -4\pi\rho_{m,n}\Delta^2,$$

where we have assumed a uniform grid spacing $\Delta r = \Delta z = \Delta$.

It is mathematically convenient to write the system of equations as

$$T\vec{\phi}_{n+1} + A\vec{\phi}_n + T\vec{\phi}_{n-1} = -4\pi T\vec{\rho}_n\Delta^2$$

where $\vec{\phi}_n = \begin{bmatrix} \phi_{0,n} \\ \dots \\ \phi_{M,n} \end{bmatrix}$, $\vec{\rho}_n = \begin{bmatrix} \rho_{0,n} \\ \dots \\ \rho_{M,n} \end{bmatrix}$, T is the diagonal matrix

$$T = \begin{bmatrix} \frac{1}{8} & & & & \\ & \dots & & & \\ & & m & & \\ & & & \dots & \\ & & & & M \end{bmatrix}$$

and A is the symmetric triadiagonal matrix

$$A = \begin{bmatrix} -\frac{3}{4} & \frac{1}{2} & & & \\ m - \frac{1}{2} & -4 & m + \frac{1}{2} & & \\ & & & \dots & \\ & & & & M - \frac{1}{2} & -4 \end{bmatrix}$$

With the further transformation $T^{\frac{1}{2}}\vec{\phi}_n \rightarrow \vec{\phi}_n$ [11, p. 642], $T^{\frac{1}{2}}\vec{\rho}_n \Delta^2 \rightarrow \vec{\rho}_n$,

$$T^{-\frac{1}{2}}AT^{-\frac{1}{2}} \rightarrow A = \begin{bmatrix} -6 & \sqrt{2} & & & \\ \sqrt{2} & -4 & \frac{3}{2\sqrt{2}} & & \\ & & & \dots & \\ & & \frac{m-\frac{1}{2}}{\sqrt{m(m-1)}} & -4 & \frac{m+\frac{1}{2}}{\sqrt{m(m+1)}} \end{bmatrix},$$

the system may simply be written

$$\vec{\phi}_{n+1} + A\vec{\phi}_n + \vec{\phi}_{n-1} = -4\pi\vec{\rho}_n$$

for $\phi = 0$ at $r=R$ (B.8). Assuming the boundary conditions of symmetry about $z=L$ and $\phi(z=0) = 0$, our system of equations look like

$$\begin{aligned} A\vec{\phi}_1 + \vec{\phi}_2 &= \vec{\rho}_1 \\ \vec{\phi}_{j-1} + A\vec{\phi}_j + \vec{\phi}_{j+1} &= \vec{\rho}_j \quad j=2, \dots, N-1 \\ 2\vec{\phi}_{N-1} + A\vec{\phi}_N &= \vec{\rho}_N \end{aligned}$$

and may conveniently be written in block matrix form

$$\begin{bmatrix} I & A & I \\ & I & A & I \end{bmatrix} \begin{bmatrix} \vec{\phi}_{j-1} \\ \vec{\phi}_j \\ \vec{\phi}_{j+1} \end{bmatrix} = \begin{bmatrix} \vec{\rho}_{j-1} \\ \vec{\rho}_j \\ \vec{\rho}_{j+1} \end{bmatrix}$$

where the corner values depend on the given boundary conditions. At the end faces, $z=0$ and L , $A\vec{\phi}_1 + \vec{\phi}_2 = -4\pi\vec{\rho}_1$ and $\vec{\phi}_{N+n} = \vec{\phi}_{N-n}$ respectively. Also $\vec{\phi}_0 = \vec{\phi}_{2N} = 0$.

One observes that, for a grid spacing of $L = N\Delta$, the solution is immediately obtained as

$$\vec{\phi}_N = -A^{-1}4\pi\vec{\rho}_N$$

By analogy we can solve the entire system for a smaller grid spacings by suitably lumping equations together and after obtaining the solution at a single grid line and use that solution as a new boundary condition to back-solve our equations and obtain solutions at each of the other grid lines. Such a method is conceivably less time consuming than a brute force method of solving the system such as Gaussian elimination. In fact the Buneman algorithm reduces the necessary calculations by a factor $\ln N/N$.

After multiplying even equations by $-A$ and adding adjacent odd equations, we obtain the reduced set

$$\begin{aligned} (2I - A^2)\vec{\phi}_2 + \vec{\phi}_4 &= \vec{\rho}_1 + \vec{\rho}_3 - A\vec{\rho}_2 \\ \vec{\phi}_{j-2} + (2I - A^2)\vec{\phi}_j + \vec{\phi}_{j+2} &= (\vec{\rho}_{j-1} + \vec{\rho}_{j+1}) - A\vec{\rho}_j \\ 2\vec{\phi}_{j-2} + (2I - A^2)\vec{\phi}_N &= 2\vec{\rho}_{N-1} - A\vec{\rho}_N \end{aligned}$$

where we have multiplied the last equation by $-A$ but the second to last by $-2I$. This is equivalent to increasing the system length by 2 and placing a mirror charge distribution on the opposite side.

This process may be repeated k times for $N = 2^k$. Each time we shall have a new matrix $A^{(r)} = 2I - (A^{(r-1)})^2$ in a system of equations in the same form but half the size of the original set. The $k - 1^{\text{st}}$ reduction yields

$$\begin{aligned} A^{(k-1)}\phi_{2^{(k-1)}} + \phi_{2^k} &= \rho_{2^{(k-1)}}^{(k-1)} \\ 2\phi_{2^{k-1}} + A^{(k-1)}\phi_{2^k} &= \rho_{2^k}^{(k-1)} \end{aligned}$$

And finally

$$A^{(k)}\vec{\phi}_{2^{(k)}} = \vec{\rho}_{2^{(k)}}^{(k)}$$

where $A^{(k)} = 2 - (A^{(k-1)})^2$ and $\rho_{2^{(k)}}^{(k)} = 2\rho_{2^{(k-1)}}^{(k-1)} - A^{(k-1)}\rho_{2^{(k)}}^{(k-1)}$.

A convenient (and quick) way to solve this equation results from the factorization of $A^{(r)}$. Note $A^{(r)}$ satisfies

$$A^{(r)} = 2I - (A^{(r-1)})^2$$

which is a polynomial expression in A and I. One may recognize the equation for the $A^{(i)}$ as a difference equation of the form

$$p_{i+1} = 2 - p_i^2$$

with solution

$$p_i = -2 \cos 2^i \theta$$

We can factor p_{k+1} by expressing it in terms of its roots[21]:

$$\begin{aligned} p_{k+1} = 2 - (-2 \cos 2^k \theta)^2 &= 0 \\ \cos^2 2^k \theta &= \frac{1}{2} \\ \cos 2^k \theta &= \pm 1/\sqrt{2} \\ 2^k \theta &= (2n - 1)\pi/4 \\ \theta &= \frac{\pi(2n - 1)}{2^{k+1}2} \end{aligned}$$

This means that $A^{(k)}$ may be written as

$$A^{(k)} = (-1)^{1+2^k} \prod_{r=1}^k (A + 2I \cos \theta_r)$$

and the solution can be obtained by k inversions of tridiagonal matrices.

If applied directly, this algorithm is unstable but, as Buneman discovered, stability may be acquired by more subtle treatment of the charge densities on the RHS. Letting $y_j^r = A^{(r)} p_j^{(r)} + q_j^{(r)}$

$$\begin{aligned} p_j^{(r+1)} &= p_j^{(r)} - (A^{(r)})^{-1} (p_{j+2^r}^{(r)} + p_{j-2^r}^{(r)} - q_j^{(r)}) \\ q_j^{(r+1)} &= q_{j+2^r}^{(r)} + q_{j-2^r}^{(r)} - 2p_j^{(r+1)} \\ A^{(r)}(x_j - p_j^{(r)}) &= q_j^{(r)} - (x_{j-2^r} + x_{j+2^r}) \\ x_j &= p_j^{(r)} + (x_j - p_j^{(r)}) \end{aligned}$$

These are [11, Eqns. 11.6 a,b, 11.7, and 11.8] and is the Poisson solver implemented in our simulations.

Bibliography

- [1] Milton Abramowitz and Irene A. Stegun, editors. *Handbook of Mathematical Functions*. Applied Mathematics Series 55. National Bureau of Standards, June 1964.
- [2] S.-I. Akasofu and J.R. Kan, editors. *Physics of Auroral Arc Formation*. American Geophysical Union, 1981.
- [3] YA. L. Fobert. *The Near-Earth and Interplanetary Plasma*. Cambridge University Press, 1983.
- [4] Carl M. Bender and Steven A. Orzag. *Advanced Mathematical Methods for Scientists and Engineers*. McGraw-Hill Book Company, 1978.
- [5] Charles K. Birdsall and A. Bruce Langdon. *Plasma Physics via Computer Simulation*. McGraw-Hill Book Company, 1985.
- [6] Lars P. Block. Potential double layers in the ionosphere. *Cosmic Electrodynamics*, 3:349–376, 1972.
- [7] David Bohm. Minimum ionic kinetic energy for a stable sheath. In A. Guthrie and R.K. Walkerling, editor, *The Characteristics of Electrical Discharges in Magnetic Fields*, pages 77–86. McGraw-Hill, New York, 1949.
- [8] J.P. Boris. Relativistic plasma simulation - optimization of a hybrid code. In Jay P. Boris and Ramy A. Shanny, editors, *Fourth Conference on Numerical Simulation of Plasmas*, pages 3–67, Washington, D.C., November 2,3 1970. Naval Research Laboratory.
- [9] Joseph E. Borovsky. The scaling of oblique plasma double layers. *The Physics of Fluids*, 26(11):3273–3278, November 1983.

- [10] T.J. I'A Bromwich. *An Introduction to the Theory of Infinite Series*. MacMillan, London, second edition, 1965.
- [11] B.L. Buzbee, G.H. Golub, and C.W. Nielson. On direct methods for solving poisson's equation. *SIAM Journal of Numerical Analysis*, 7(4), December 1970.
- [12] Sydney Chapman. History of aurora and airglow. In Billy M. McCormac, editor, *Aurora and Airglow*, pages 15–28, NY, 1967. NATO Advanced Study Institute, University of Keele, 1966, Rheinhold Publishing Corporation.
- [13] Francis F. Chen. *Introduction to Plasma Physics*. Plenum Press, 1974.
- [14] Y.T. Chiu and Michael Schultz. Self-consistent particle and parallel electrostatic field distributions in the magnetospheric-ionospheric auroral region. *J. Geo. Res.*, 83(A2):629–642, Feb. 1 1978.
- [15] R.H. Cohen. Axial potential profiles in thermal barrier cells. *Nuclear Fusion*, 21(2):209–214, 1981.
- [16] J.W. Cooley and J.W. Tukey. An algorithm for the machine calculation of complex fourier series. *Mathematics of Computation*, 19:297–301, 1965.
- [17] Victor K. Decyk and John M. Dawson. Computer model for bounded plasma. *Journal of Computational Physics*, 30:407–427, 1979.
- [18] William E. Drummond and Marshall N. Rosenbluth. Anomalous diffusion arising from microinstabilities in a plasma. *The Physics of Fluids*, 5(12):1507–1513, December 1962.
- [19] J.W. Eastwood. Optimal particle-mesh algorithms. *Journal of Computational Physics*, 18:1–20, 1975.
- [20] E.A. Frieman and D.L. Book. Convergent classical kinetic equation for a plasma. *The Physics of Fluids*, 6(12):1700–1706, December 1963.
- [21] R.W. Hamming. *Numerical Methods for Scientists and Engineers*. McGraw-Hill, Inc., second edition, 1973.

- [22] Akira Hasegawa and Tetsuya Sato. Existence of a negative potential solitary-wave structure and formation of a double layer. *Phys. Fluids*, 25((4)):632–635, April 1982.
- [23] R.W. Hockney. Computer experiment of anomalous diffusion. *Phys. Fluids*, pages 1826–1835, Sept 1966.
- [24] John David Jackson. *Classical Electrodynamics*. John Wiley & Sons, Inc., second edition, 1975.
- [25] J.R. Kan and L.C. Lee. On the auroral double-layer criterion. *Journal of Geophysical Research*, 85(A2):788–790, February 1, 1980.
- [26] Allan N. Kaufman. Reformulation of quasi-linear theory. *J. Plasma Physics*, 8, part 1:1–5, 1972.
- [27] J.M. Kindel and C.F. Kennel. Topside current instabilities. *Journal of Geophysical Research*, 25(13):3055–3078, May 1, 1971.
- [28] Nicholas A. Krall and Alvin W. Trivelpiece. *Principles of Plasma Physics*. McGraw-Hill Book Company, 1973.
- [29] W.L. Kruer, J.M. Dawson, and B. Rosen. The dipole expansion method for plasma simulation. *Journal of Computational Physics*, 13:114–129, 1973.
- [30] Irving Langmuir. The interaction of electron and positive ion space charges in cathode sheaths. *Physical Review*, 33:955–989, June 1929.
- [31] L.R. Lyons and D.J. Williams. *Quantitative Aspects of Magnetospheric Physics*. D. Reidel Publishing Company, 1984.
- [32] T.G. Northrup. The guiding center approximation to charged particle motion. *Annals of Physics*, 15:79–101, 1961.
- [33] Hideo Okuda. Lecture notes on selected topics in space physics. These notes are from AS556 Advanced Plasma Dynamics a course given in the Astrophysics Department each year at Princeton University on a variety of topics, 1986.

- [34] Hans Peerson. Electric field parallel to the magnetic field in a low-density plasma. *The Physics of Fluids*, 9(6):1090–1098, June 1966.
- [35] F.W. Perkins and Y.C. Sun. Double layers without current. *Physical Review Letters*, 46(2):115–118, 12 January 1981.
- [36] T. Sato and H. Okuda. Ion-acoustic double layers. *Phys. Rev. Lett.*, 44(11):740–743, 17 March 1980.
- [37] T. Sato and H. Okuda. Numerical simulations on ion acoustic double layers. *J. Geophys. Res.*, 86(A5):3357–3368, May 1, 1981.
- [38] Tetsuya Sato. Strong plasma acceleration by slow shocks resulting from magnetic reconnection. *Journal of Geophysical Research*, 84(A12):7177–7190, December 1979.
- [39] Tetsuya Sato and Akira Hasegawa. Externally driven magnetic reconnection versus tearing mode instability. *Geophysical Research Letters*, 9(1):52–55, January 1982.
- [40] George Schmidt. *Physics of High Temperature Plasmas*. Academic Press, Inc., New York, 1966.
- [41] Samuel M. Selby and Brian Girling, editors. *Standard Mathematical Tables*. The Chemical Rubber Co., fourteenth edition, 1965.
- [42] Yoichi Serizawa and Tetsuya Sato. Generation of large scale potential difference by currentless plasma jets along the mirror field. *Geophysical Research Letters*, 11(6):595–598, June 1984.
- [43] Robert A. Smith. A review of double layer simulations. *Physica Scripta T2/1*, 1982.
- [44] R.L. Stenzel, M. Ooyama, and Y. Nakamura. Potential double layers formed by ion beam reflection in magnetized plasmas. *Phys. Fluids*, 24(4):708–719, April 1981.
- [45] David P. Stern. One-dimensional models of quasi-neutral parallel electric fields. *Journal of Geophysical Research*, 86(A7):5839–5360, July 1, 1981.

- [46] Thomas Howard Stix. *The Theory of Plasma Waves*. McGraw-Hill Book Company, Inc., 1962.
- [47] T.E. Stringer. Electrostatic instabilities in current-carrying and counterstreaming plasmas. *Plasma Physics*, 6:267-279, 1964.
- [48] Daniel W. Swift and John J. Ambrosiano. Boundary conditions which lead to excitation of instabilities in plasma simulations. *Journal of Computational Physics*, 44:302-317, 1981.
- [49] Michael Temerin and F.S. Mozer. Double layers above the aurora. In R. Schrittwieser and G. Eder, editors, *Second Symposium on Plasma Double Layers and Related Topics*, pages 119-127, University of Innsbruck, July 5/6, 1984.
- [50] Lewi Tonks and Irving Langmuir. A general theory of the plasma of an arc. *Physical Review*, 34:876-922, Sept. 15, 1929.
- [51] John S. Wagner. *A Computer Simulation of Auroral Formation*. PhD thesis, Univ of Alaska, May 1981.
- [52] Elden C. Whipple, Jr. The signature of parallel electric fields in a collisionless plasma. *J. Geo. Res.*, 82(10):1525-1531, April 1, 1977.